PRODUCTION OF D^0(1863) MESONS IN 217 GEV/C PI-MINUS PROTON INTERACTIONS

BY

DANIEL EUGENE BENDER

B. S., University of Illinois, 1974
M. S., University of Illinois, 1975

THESIS

Submitted in partial fulfillment of the requirements
for the degree of Doctor of Philosophy in Physics
in the Graduate College of the
University of Illinois at Urbana-Champaign, 1980

Urbana, Illinois

PRODUCTION OF D^0(1863) MESONS IN 217 GEV/C
PI-MINUS PROTON INTERACTIONS

Daniel Eugene Bender, Ph. D.
Department of Physics
University of Illinois at Urbana-Champaign, 1980

This thesis reports on the analysis of data obtained during FNAL experiment E369. The Chicago Cyclotron Magnet Spectrometer Facility was used to perform a search for the hadronic production of charmed D mesons. A 217 Gev π^- beam was incident on a liquid hydrogen target. The trigger required a slow recoil proton in coincidence with a muon. A total of 26 ± 8 neutral D mesons were observed through their $K0\pi^+\pi^-$ decay mode. The distributions of Feynman X, missing mass, and momentum transfer to the recoil proton were consistent with diffractive production. Cross sections were calculated based on a diffractive model.

ACKNOWLEDGEMENTS

First and foremost deserving of thanks for her patience and understanding is my wife Mary. Very special thanks is also due to my advisor, Lee Holloway, for allowing me to do the analysis in my own way. I thank Professors Lou Koester, Bob Sard, and Giulio Ascoli for many stimulating conversations. Special thanks to the people who participated in various phases of the analysis: Mike Shupe, John Cooper, George Alverson, Waldo MacKay, Eric Smith, and Steve Hahn; and to the computer programmers who gave their help so freely: Jerry Wray, Dave Lesny, and Keith Nater. Finally, I would like to thank all those people whom I have not mentioned by name but who helped me in one way or another.

This thesis is dedicated to my wonderful parents.

The work presented in this thesis was supported in part by the Department of Energy under grant DE-AC02-76ER01195.

TABLE OF CONTENTS

CHAPTER 1

INTRODUCTION

The data described in this thesis was collected during an experiment performed at Fermi National Accelerator Laboratory. The work was done by a collaboration of physicists and students from Fermilab, Harvard University, the University of Illinois, the University of Oxford, and Tufts University.

The Chicago Cyclotron Magnet (CCM) spectrometer in the Muon Laboratory was the basis for the experimental setup. A beam of 217 Gev/c negative pions was brought to the Muon Lab, and focussed onto both beryllium and liquid hydrogen targets.

This thesis is concerned with but one of the three separate parts of the experiment. This part was designed to be sensitive to the production of pairs of charmed particles with masses in the range 1.5 to 3.5 Gev/c^2. This was accomplished by requiring the detection of a slow proton recoiling from the interaction such that the total invariant mass of the final state particles was between 3.0 and 7.0 Gev/c^2. This diffractive process is illustrated by the diagram in Figure 1-1. The missing mass, M , is defined by:

$$M_X^2 = P_X^2 = (P_\pi + P_p - P_p')^2$$

and the momentum transfer, t, to the recoil proton is:

$$t = (P_p - P_p')^2 .$$

The diffractive nature of reactions producing a slow recoil proton also increased the probability that the interaction products would have enough momentum to be accepted into the spectrometer. To enhance the probability of triggering the apparatus on production of charmed particles, a muon was also required, since it was believed that the lowest lying charmed particles should have a substantial semi-leptonic branching ratio.

Figure 1-1. Schematic diagram for the inclusive diffractive process $\pi^- + P \rightarrow P + X^-$.

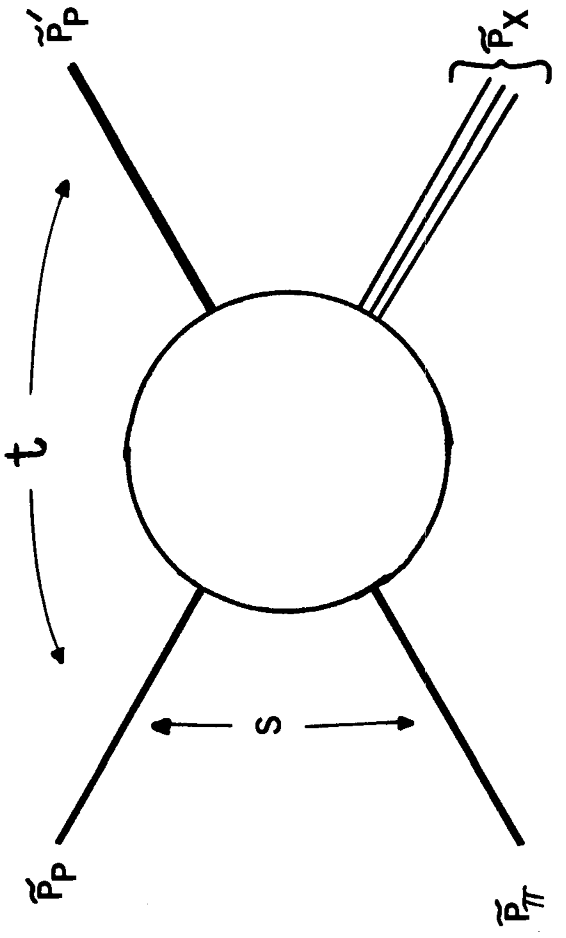
$\tilde{P}_P'$
$\tilde{P}_X$
t
s
$\tilde{P}_P$
$\tilde{P}_\pi$

The 1 MU.P ("one mu dot p", for the muon and proton in coincidence) trigger can be summarized by the two particle inclusive reaction:

$$\pi^- + p \to p + \mu + X$$

A large sample of such reactions (200,000 events with reconstructed recoil proton track) has been collected. The following chapters detail the analysis of the data and the results obtained.

CHAPTER 2

THEORY

Six years have passed since the report (Augustin, 1974; Aubert, 1974) of an unusual new particle astounded the world's physicists. This was the so-called Ψ/J particle. Its discovery led to a revolution in high energy physics, since it paved the way for a new quantum number - charm.

The idea of a charmed quark had been tossed about for quite some time, since being introduced in 1964 by Bjorken and Glashow (Bjorken and Glashow, 1964). At that time, charm was proposed to provide a sort of lepton-hadronic fermion symmetry; four leptons were known and it was aesthetically pleasing to have the same number of hadronic fermions (quarks). These four quarks and their quantum numbers are listed in Table 2-1.

The first real application of the charmed quark was found in 1970 by Glashow, Iliopoulous, and Maiani (Glashow, Iliopoulous, and Maiani, 1970). They found that adding a fourth quark (charm) to the Weinberg-Salam theory of weak interactions removed a troublesome strangeness changing neutral current from the WS Lagrangian. This made the theory consistent with known experimental limits on the magnitude of such an effect.

Adding a fourth quark essentially doubled the number of expected particles. Some of the lightest of the new charmed particles are listed with their quantum numbers in Table 2-2. Since none of these particles had been seen, charm, despite its success with the WS theory, was on shaky ground. The Ψ/J was soon interpreted as the bound state of a charmed quark anti-quark pair. Real confirmation of the charmed quark's existance came in 1976 with the observation of the D^0 meson (Perruzi, 1976), and shortly thereafter, the $D^{\pm}$. The observation that the $D^{\pm}$ decayed into a

TABLE 2-1

QUANTUM NUMBERS OF ORIGINAL QUARKS PLUS CHARM

QUARK	I	I_z	CHARGE	STRANGENESS	CHARM
u	1/2	1/2	2/3	0	0
d	1/2	-1/2	-1/3	0	0
s	0	0	-1/3	-1	0
c	0	0	2/3	0	1

TABLE 2-2

SOME OF THE LIGHTEST HADRONS WITH A CHARMED QUARK

HADRON	QUARK CONTENT	J	I	C	S	B
D^+	$c\bar{d}$	0	1/2	1	0	0
D^o	$c\bar{u}$	0	1/2	1	0	0
F^+	$c\bar{s}$	0	0	1	1	0
η_c	$c\bar{c}$	0	0	0	0	0
Ψ	$c\bar{c}$	1	0	0	0	0
Λ_c^+	udc	1/2	0	1	0	1

final state ($K^{\mp}\pi^{\pm}\pi^{+}$) not accessible to known hadrons was in perfect agreement with the predictions of the WS theory.

2.1 Decays of Charmed Mesons

Since charm is conserved in strong and electromagnetic interactions, the lightest charmed mesons (and baryons) must decay via the weak interaction. According to the WS model, the charged hadronic current is:

$$J^{h}_{\mu} = (\bar{c}\ \bar{u})\gamma_{\mu}(1-\gamma_5)\begin{bmatrix} -\sin\theta_c d + \cos\theta_c s \\ \cos\theta_c d + \sin\theta_c s \end{bmatrix}$$

The value of θ_c, the Cabibbo angle, is experimentally determined to be about 13°.

The mediator of the charged weak current is the intermediate vector boson - $W^{\pm}$. The decay of the c quark can be envisioned as occurring via the emission of a virtual W^{+}, which then decays into a $q\bar{q}$ or $\bar{\ell}\ell^{+}$ (lepton anti-lepton) pair. In this process the c quark is transformed into an s or d quark with an appropriate probability. The decay is described in the WS model by the coupling of the hadronic current to the weak current:

$$W^{+}_{\mu}J^{\mu} + J^{+}_{\mu}W^{\mu}$$

The relevant diagrams are shown in Figure 2-1 with their coupling strengths.

The most striking prediction of the WS model for charmed particle decay is that most of the time the decay products will contain a strange particle. This results from the vertex coupling strengths. The decay rate is proportional to the square of the coupling strength. It is evident that the decay of the c quark into a d quark is suppressed by a factor of $\tan^2\theta_c$ relative to its decay into an s quark.

Figure 2-1. Weak current vertex diagrams for quarks and leptons.

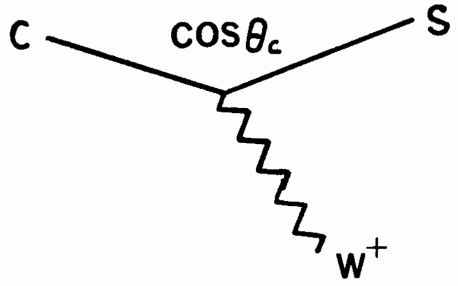
c
cosθc
s
w+

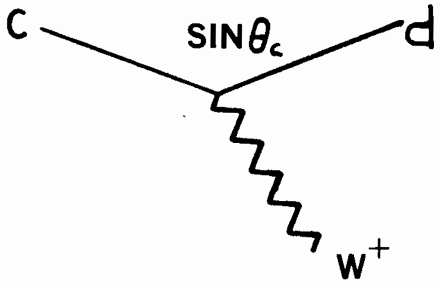
c
SINθc
d
w+

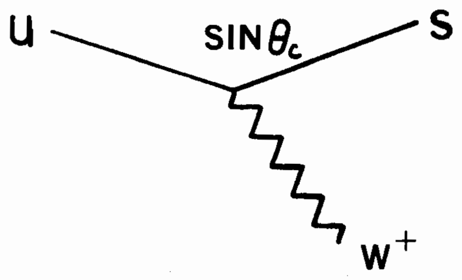
u
SINθc
s
w+

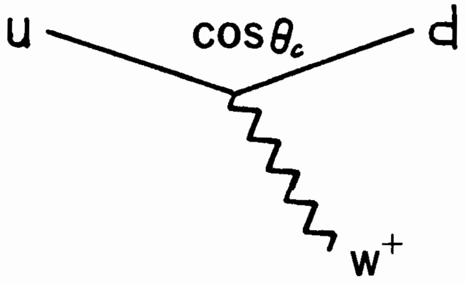
u
cosθc
d
w+

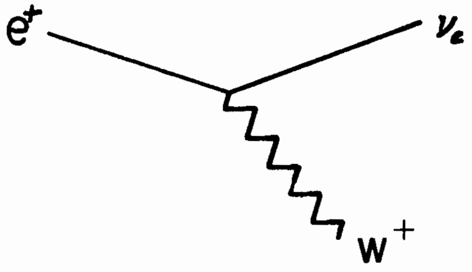
e+
νe
w+

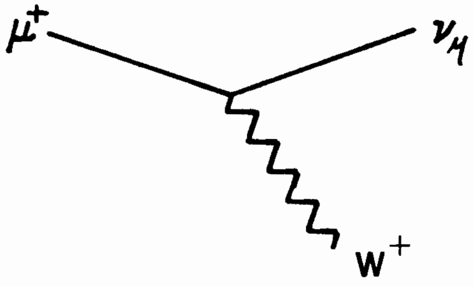
μ+
νμ
w+

2.2 Lifetimes of Charmed Mesons

Recent evidence (Bacino, 1980) indicates that the neutral and charged D mesons have different lifetimes. Both direct measurements of the lifetimes by travel times and measurements of the semi-leptonic branching ratios are consistent in reporting that $\tau_{D^+}/\tau_{D^o} \sim 5\text{-}10$.

Two possible explanations for this effect have been forwarded. One (Bander, 1980) points out that the D^o can decay via the W-exchange mechanism shown in Figure 2-2. The D^+ has no such (Cabibbo non-suppressed) diagram (see Figure 2-2(b)). The gluon emission overcomes the problem of the suppression of this type of diagram due to helicity considerations. This process can account for the observed differences in lifetimes.

The second explanation (Rosen, 1980) invokes a sextet dominance argument which predicts the tendency for the D^+ to have a longer lifetime. The two explanations have somewhat different expectations for the lifetime of the F meson. The sextet dominance theory gives the F^+ the same lifetime as the D^o, while the W-exchange (the F meson can decay according to the diagram in Figure 2-2(c)) predicts the lifetime of the F^+ should be between the D^o and D^+ lifetimes. The measurements of a few F^+ meson lifetimes seem to favor the W-exchange mechanism (Trilling, 1980).

2.3 Hadronic Production of Charm

The hadronic production of charmed particles may be the least understood facet of charm phenomenology. The reason for this is the seemingly large gap between the predicted charm production cross sections and the reported cross sections. Much more data will be needed to determine just how (and how much) charm is produced in hadronic interactions. I will describe the basic assumptions which underlie the various popular charm production mechanisms.

Figure 2-2. W-exchange (a) and quark annihilation (b), (c) diagrams for the decay of the D^o, D^+, and F^+ charmed mesons respectively.

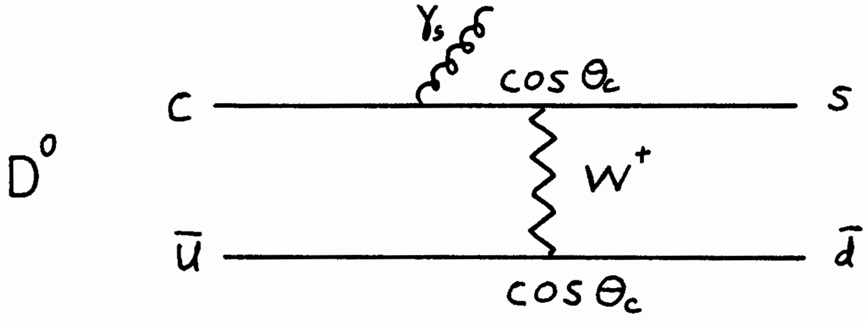
γ_s
$\cos\theta_c$
c
s
D^0
W^+
$\bar{u}$
$\bar{d}$
$\cos\theta_c$

(a)

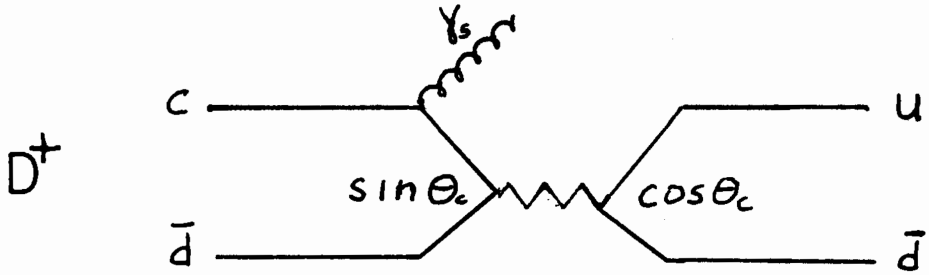
γ_s
c
u
D^+
$\sin\theta_c$
$\cos\theta_c$
$\bar{d}$
$\bar{d}$

(b)

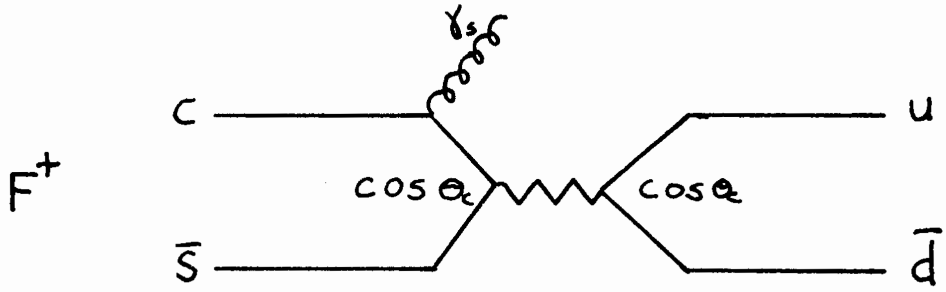
γ_s
c
u
F^+
$\cos\theta_c$
$\cos\theta_c$
$\bar{s}$
$\bar{d}$

(c)

There are two major classes of models for the calculation of charm cross sections:

1. Central production models
2. Diffractive production models

There may be a region between these two classes not covered by either.

2.3.1 Central Production Models

The central production models are those which predict the production of a $c\bar{c}$ quark pair with little momentum in the center of mass system. Two popular central production models are the Drell-Yan-like quark annihilation model (Roy, 1975) and the gluon fusion model (Jones and Wyld, 1978; Carlson and Suaya, 1978). Schematic diagrams of the processes basic to these models are shown in Figure 2-3.

These models are based on the parton description of hadrons (quantum chromodynamics). The partons are the quarks, anti-quarks, and gluons which compose the hadrons in question. Statistical in nature, these models assume each parton carries a fraction of the hadron's momentum:

$$x_i = p_i / P$$

The distribution of x (called the structure function) depends on the flavor if the parton is a quark. All gluons have the same structure functions. At high energies, the partons' momenta are assumed to be parallel to that of the hadron, thus ignoring their relative transverse momenta.

In these models, a high energy hadronic interaction is treated as a collision of single parton from each hadron. Perturbation theory can be used since the strong coupling constant, $g^2/4\pi$, is about 0.25. The Drell-Yan-like model assumes that a quark from one of the hadrons annihilates its anti-quark from the other hadron forming a virtual gluon.

Figure 2-3. Schematic diagrams for the Drell-Yan-like model (a) and the gluon fusion model (b). The external lines indicate an inclusive reaction.

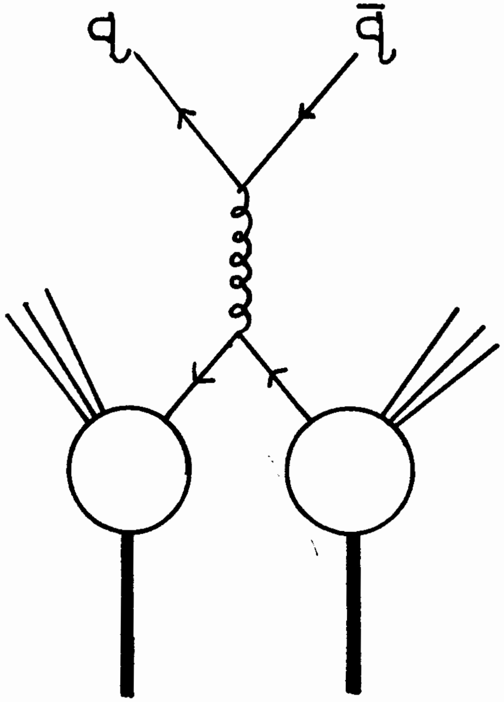

(a)

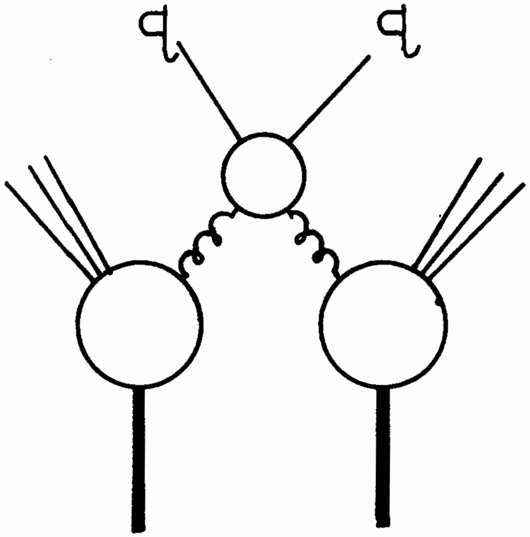

(b)

The gluon then decays into a $c\bar{c}$ pair (at least if that is what one is calculating). The gluon fusion model is almost self-explanatory. Two gluons, one from each hadron, "fuse" and produce a $q\bar{q}$ pair ($c\bar{c}$ in the case of interest). Interactions among the final state partons are necessary to yield color singlet states, but are assumed to have a small effect on the observed distributions.

Without going into the details of the calculations, I will simply state the charm production cross sections predicted by these models for the reaction $\pi^- + P \to c\bar{c} + X$ at s=400 Gev . This was approximately the center of mass energy for E369.

Jones and Wyld calculated the Drell-Yan-like model cross section to be about 400 nb using the quark structure functions of Feynman and Field. They assumed a gluon structure function of the form:

$$g(x) \propto (1-x)^n / x$$

for n=5 and 10. The resulting gluon fusion cross section varies from about 300 nb for n=10 to about 1.2μb for n=5.

2.3.2 Diffractive Production Models

The small cross sections calculated (Barger and Philips, 1975) for such diffractive models as D channel exchange (1 nb) and triple Regge processes with D exchange (60 nb) led to the popular belief that most charm particles should be centrally produced.

Abandoning such elaborate models, I have chosen to use a parametrization of high energy diffractive scattering data. The distribution of the recoil proton was fitted (Ascoli, 1975) to the form:

$$\frac{d^2\sigma}{dt\,dM_X^2} \propto e^{-b(M_X^2)|t|}$$

In the ranges $12 < M_X^2 < 50$ $(\text{Gev}/c^2)^2$ and $-0.4 < t < -0.04$ Gev :

$$b(M_X^2) = 4.7 + 7.0 \times \exp(-34.7 \times M_X^2/s)\ \text{Gev}^{-2}$$

The "fireball" which is left has a Feynman X of

$$X_F = 1 - M_X^2/s$$

It is this high energy excited blob which, it is hoped, will sometimes decay into a pair of charmed hadrons. This model was used to calculate the acceptance of the apparatus through the decay process just described. The acceptance calculation is detailed in Chapter 6.

A model of diffractive production proposed by Gustafson and Peterson (Gustafson and Peterson, 1977) yields cross sections which compare favorably to those reported in diffractive interactions (see section 6-4). This model can be used to predict charm production cross sections from, for example, strange particle production cross sections.

The cross section for producing a blob with mass M_X and $X > 0.8$ is proportional to:

$$\sigma(M_X) \propto \ln(0.2\ s/M_X^2)$$

This derivation is based on the experimental result that $d\sigma/dM_X^2 \propto 1/M_X^2$. They argue that a diagram such as that in Figure 2-4 would yield a cross section for the production of a $q\bar{q}$ pair inversely proportional to the produced quarks' mass squared:

$$\sigma(qq) \propto 1/M_q^2$$

This would lead to quark production cross sections in the ratios:

$$u:d:s:c = 1:1:1/4:1/100$$

for quark masses of 150 Mev/c^2 for the u and d quarks, 300 Mev/c^2 for the s and 1500 Mev/c^2 for the c. This type of reasoning leads to a inclusive cross section for the Λ_c^+ charmed baryon of 80 μb for 300 Gev/c protons and 150 μb for colliding beam energies ($\sqrt{s}$ = 60 Gev). The Λ_c^+ cross section was obtained from the known cross section for inclusive Λ^0 production in diffractive interactions.

Figure 2-4. Schematic diagram for the diffractive production model of Gustafson and Peterson.

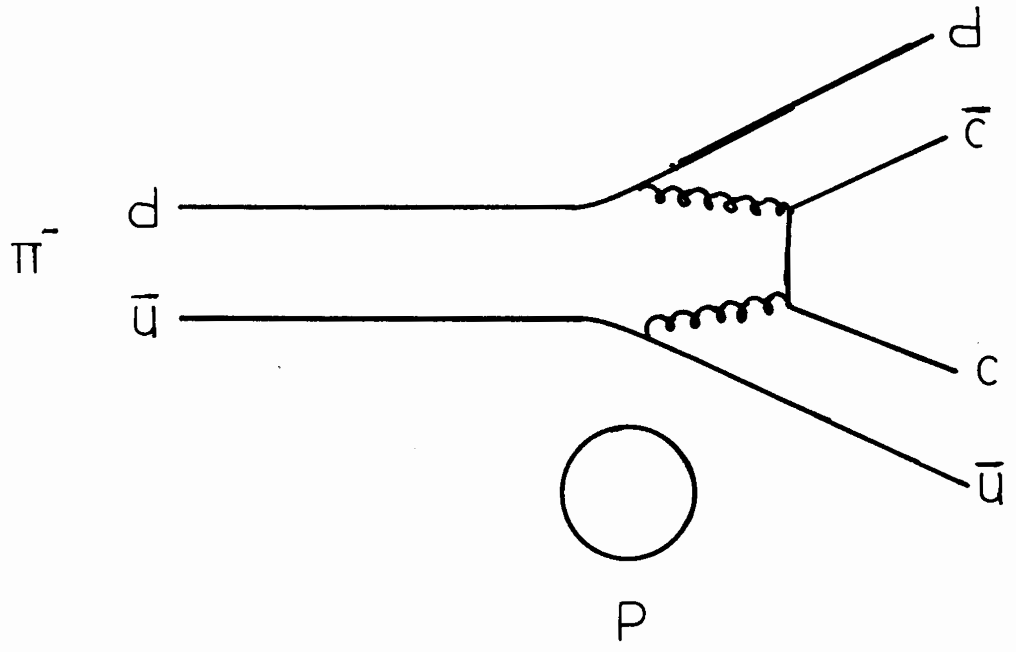
π^-
d
$\bar{u}$
d
$\bar{c}$
c
$\bar{u}$
P

For the limited range of M_X in E369, the dependence of the cross section on M_X can be ignored. Thus one may try to deduce the inclusive charm cross section from the inclusive strange particle production cross section in the same region of M_X. A simple estimate would give $\sigma(D+X)= \sigma(K+X)/25$.

CHAPTER 3

THE APPARATUS

The configuration of the Chicago Cyclotron Magnet (CCM) spectrometer as used in this experiment was basically unchanged from previous experiments. The few changes made were the removal of some spark chambers, the addition of a recoil proton detector and a lead glass Cerenkov photon detector, and the rearrangement of some of the scintillation counter hodoscopes.

The CCM spectrometer has been described in detail in several previous theses (Pordes, 1976; Hicks, 1978; Proudfoot, 1978). Therefore, the following discussion of the apparatus will cover only the main features and the changes, with references to previous theses where appropriate.

The laboratory coordinate system was defined with Z pointing along the nominal beam direction. The Y axis was vertical, and the X axis pointed left when observed from upstream(see Figure 3-1). Positively charged particles were deflected in the positive X direction by the CCM. The CCM was operated at 14.047 kilogauss yielding a 2.1 Gev/c transverse momentum kick.

A convenient breakdown of the apparatus may be made as follows:

1. Beam line equipment
2. Target, recoil proton, and trigger equipment
3. Particle tracking equipment
4. Particle identification and timing equipment

3.1 Beam Line Equipment

The equipment used in collimating, tracking, and defining the 217 Gev/c negative pion beam is shown schematically in Figure 3-2. The trajectory of the beam particle was determined by the 6 (4 X planes and 2 Y

Figure 3-1. Schematic view of experimental apparatus.

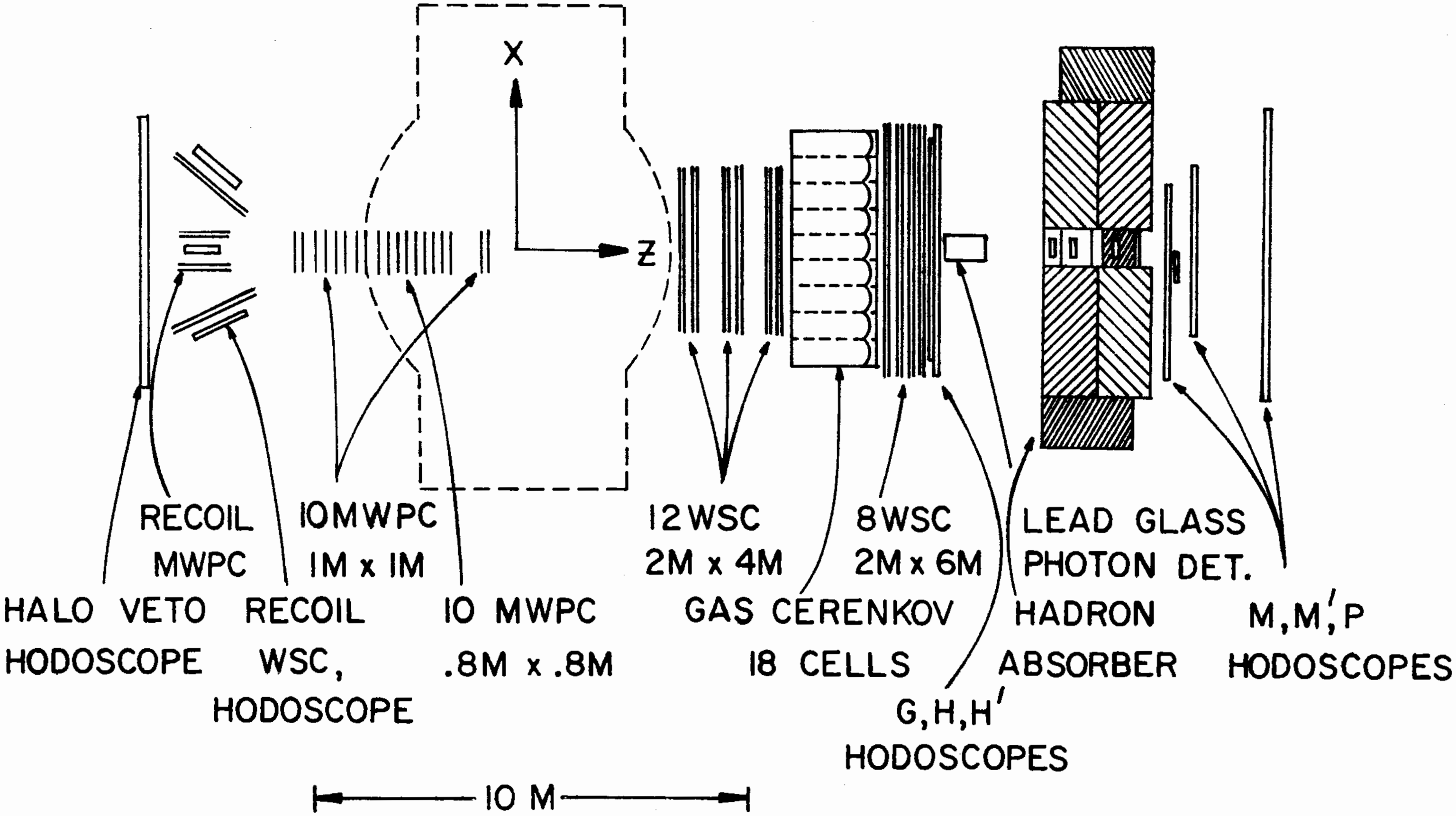
X
Z
RECOIL MWPC
10 MWPC 1M x 1M
12 WSC 2M x 4M
8 WSC 2M x 6M
LEAD GLASS PHOTON DET.
HALO VETO HODOSCOPE
RECOIL WSC, HODOSCOPE
10 MWPC .8M x .8M
GAS CERENKOV 18 CELLS
HADRON ABSORBER
M, M′, P HODOSCOPES
G, H, H′ HODOSCOPES
10 M

planes) beam multi-wire proportional chambers (MWPC). These had 6" X 6" active areas and 1/12" wire spacing. The dipole tagging magnets allowed determination of the beam particle´s momentum. The beam scintillation counter hodoscopes provided the timing information necessary to distinquish (in most cases) between the interacting particle and others which may have passed through the MWPC´s within their resolution time. Each hodoscope consisted of eight 3/4" X 6" X 1/4" counters (except BH1 which had 1" X 8" X 1/4" counters). Three threshold Cerenkov counters at low pressure helped to distinquish the heavier particles (kaons and protons) from the pions. The quadrupole magnet located just upstream of the final beam MWPCs and hodoscopes provided the focussing necessary to achieve a 1" diameter beam cross section at the target.

The veto hodoscopes were scintillators arranged around the beam line so as to identify any beam particle which deviated from the desired trajectory (i.e., inside the beam pipe). The "veto wall" was a concrete wall 3 m X 5 m X 1 m thick covered on the upstream side with scintillation counters. The main function of this hodoscope was to veto any muons coming from the berm (the earthern hadron absorber for the neutrino line). Since muons were required in the event trigger, it was important to veto events with muons from external sources.

3.2 Recoil Proton, Trigger, and Target Equipment

A schematic diagram of the target region is shown in Figure 3-3. The two targets, 4.81 g/cm^2 of beryllium and 3.26 g/cm^2 of liquid hydrogen, are indicated. Fiqure 3-1 shows the E369 apparatus, and locates the targets relative to the CCM. A description of the LH2 target can be found in the thesis of W. W. MacKay (MacKay, 1980).

Figure 3-2. Beam control and tracking equipment.

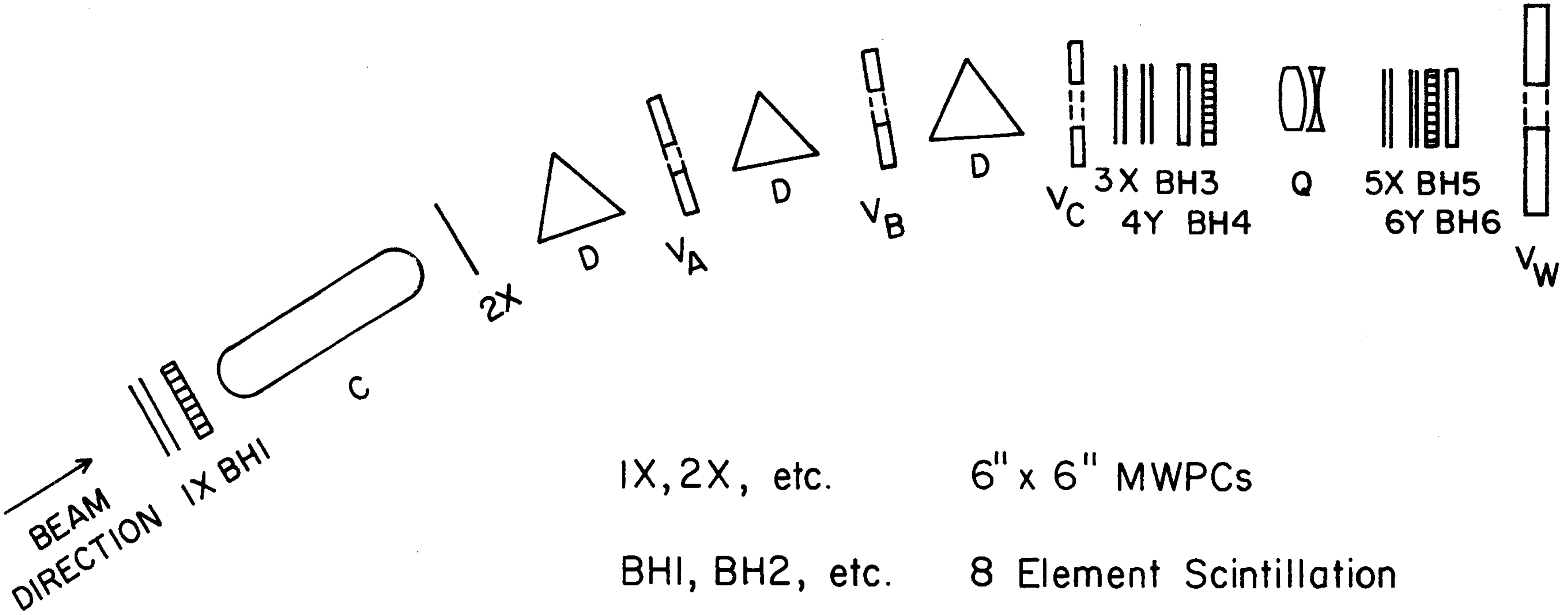

1X, 2X, etc.	6" x 6" MWPCs
BH1, BH2, etc.	8 Element Scintillation Counter Hodoscopes
V_A, V_B, V_C	Veto Counters
V_W	5M x 3M Halo Veto Wall
D	Magnetic Dipoles
Q	Quadrupole (Beam Focusing)
C	Threshold Cerenkov Counter

Figure 3-3. Schematic diagram of the target region.

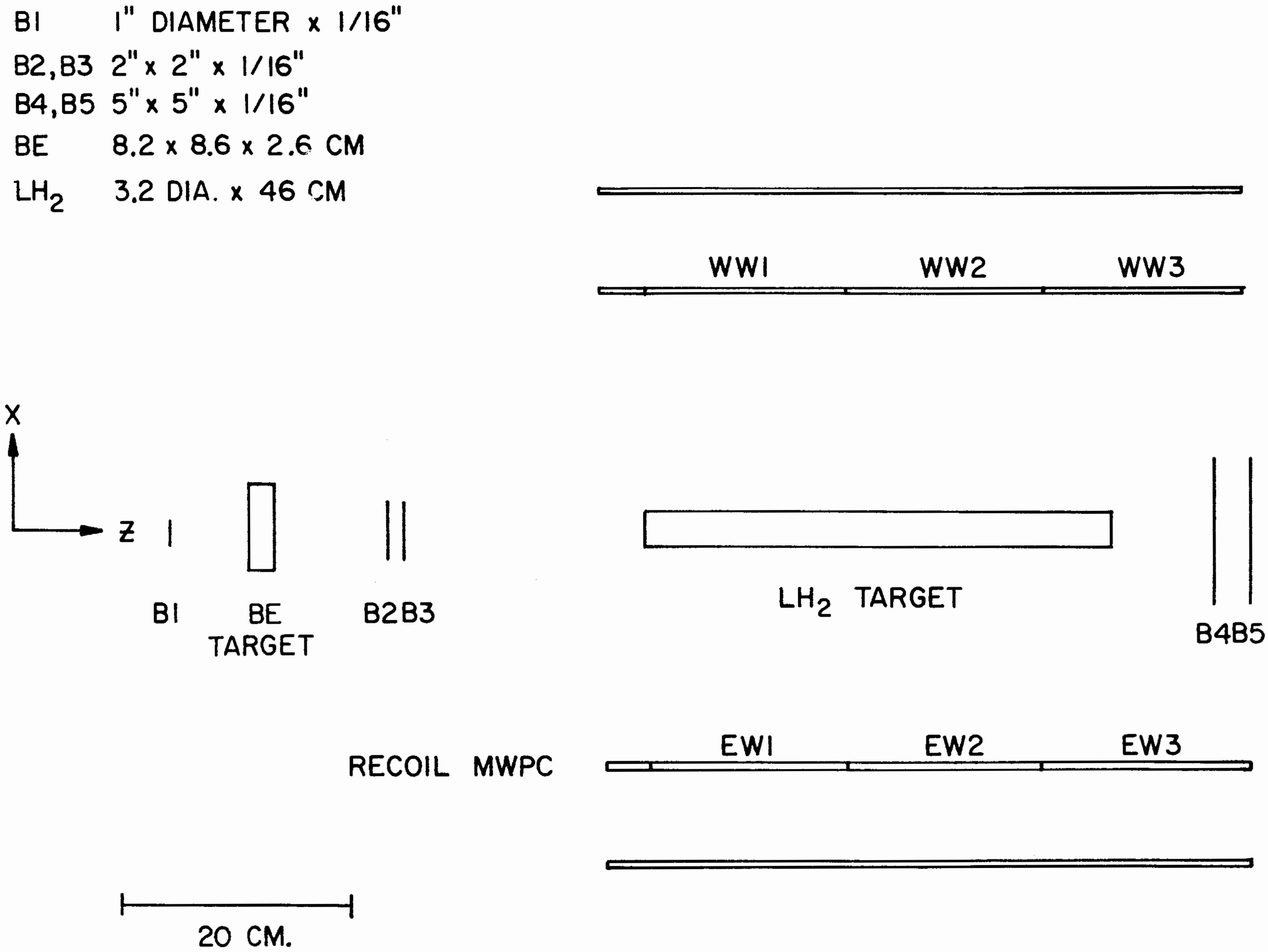

B1	1" DIAMETER x 1/16"
B2,B3	2" x 2" x 1/16"
B4,B5	5" x 5" x 1/16"
BE	8.2 x 8.6 x 2.6 CM
LH_2	3.2 DIA. x 46 CM

Scintillation counter B1 was the beam defining counter. It was a 1" diameter circular piece of 1/16" scintillator coupled to the photomultiplier tube (PMT) via an air light pipe. All valid interactions required a signal from B1.

Counters B2 and B3, placed between the Be and LH2 targets, were used in coincidence and served to identify interactions which occurred in the Be target. Similarly, B4 and B5, located just downstream of the LH2 target, were used to indicate that any interaction (either in the Be or the LH2) had occurred. Counters B1-B5 all used RCA 8575 PMTs.

The logic which made the decision as to whether the interaction had occurred in the Be or the LH2 is shown in Figure 3-4. As indicated, the output of each counter is fed into a linear fan out (LFO). One of the LFO outputs for each (B2-B5) counters is attenuated while the other is not. Both signals are then discriminated. The corresponding discriminator outputs (i.e., either un-attenuated or attenuated) are put into coincidence. The discriminators and attenuators were adjusted so that the unattenuated signals, (B4.B5)lo and (B2.B3)lo, occurred on the passage of one minimum ionizing particle, and the attenuated signals, (B2.B3)hi and (B4.B5)hi, occurred only for 3 or more minimum ionizing particles. (At least this was the intended setting; however, it was discovered too late that the high level signals occurred only about 50% of the time when there were 3 minimum ionizing particles.) Thus a signal from (B2.B3)hi indicated an interaction in the Be target, while a signal from (B4.B5)hi, and no signal from (B2.B3)hi, meant that a LH2 interaction had occurred.

There were three separate interaction triggers used in the experiment. The mnemonics given them were 2MU, 1 MU.P, and LMP. The 2MU trigger required an interaction in either the Be or LH2 target as well as signals

Figure 3-4. Interaction trigger logic.

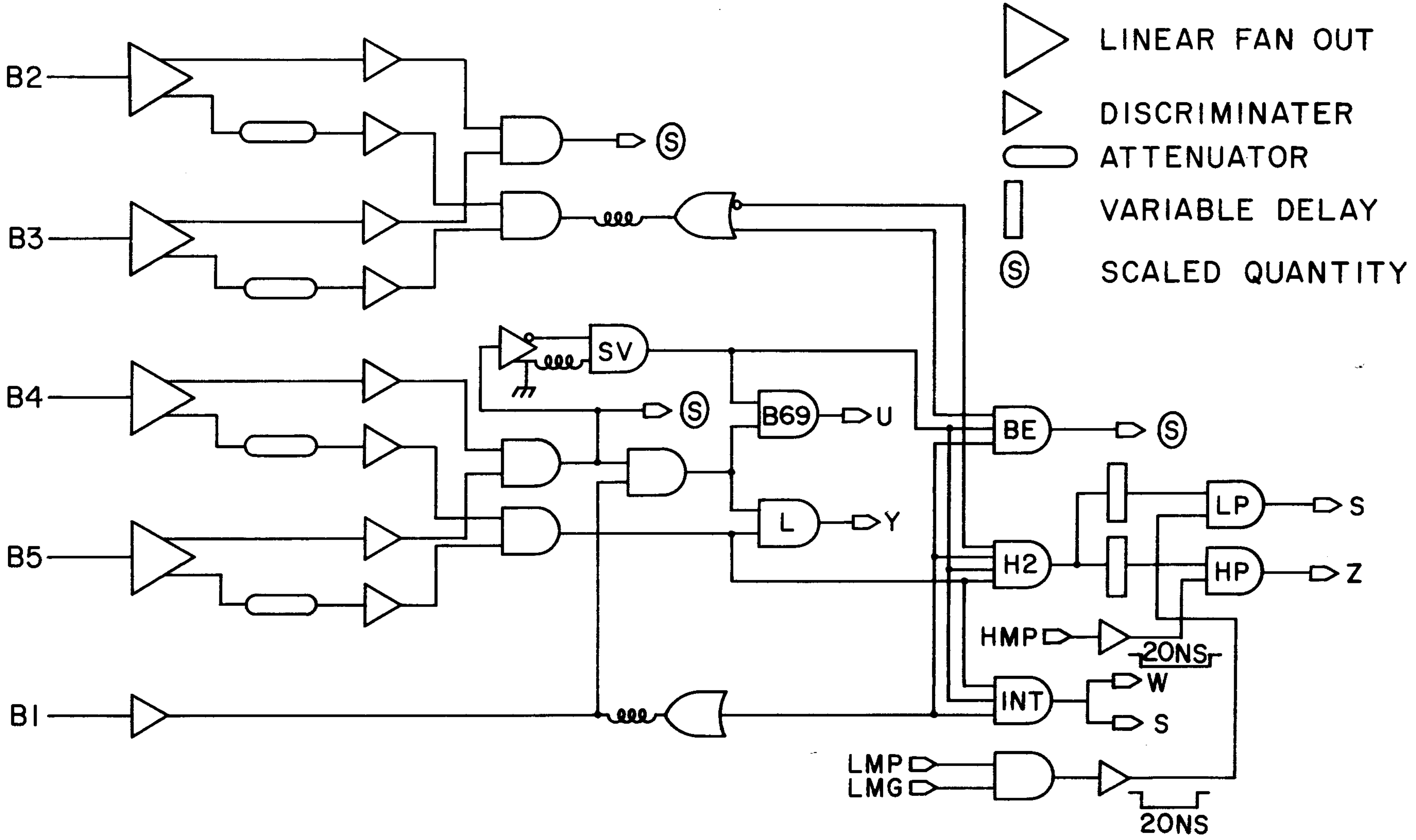

LINEAR FAN OUT
DISCRIMINATER
ATTENUATOR
VARIABLE DELAY
S SCALED QUANTITY
B2
B3
B4
B5
B1
S
SV
S
B69
U
L
Y
BE
S
H2
LP
S
HP
Z
HMP
20NS
INT
W
S
LMP
LMG
20NS

from opposite quadrants of the P hodoscope. The P and M´ (M-prime) hodoscopes, placed downstream of a hadron absorber, were used to identify muons in the interaction products. These hodoscopes are described more completely below. The 1 MU.P trigger required a LH2 interaction, a slow recoil particle, and a signal from the P or M´ hodoscope indicating a muon. The 1 MU.P trigger is described fully below. The LMP trigger was designed to provide a large sample of 3 and 5 prong diffractive interactions, but failed because the threshold on the (B4.B5)hi discriminator was set too high to trigger reliably on 3 minimum ionizing particles. This error also affected the 1 MU.P trigger, though probably not seriously.

Of the three triggers used in the experiment, two (1 MU.P and LMP) required a slow proton recoiling from the vertex. Sets of MWPCs, wire spark chambers (WSC henceforth), and scintillation counters on each side of the LH2 target served to detect these protons, and measure their time of flight. As shown in Figure 3-5, 2 MWPC planes were positioned on either side of the target, and about 20 cm away. These planes had vertical wires spaced at 1/16", and used a shift-register readout system developed by Dr. T. Kirk (Hicks, 1978). The 4 WSC planes on each side were placed at an angle of 25.5 degrees to the Z axis. The planes were type XY or X´Y (X´ tilt angle was 6 degrees from the vertical), and had a magnetostrictive readout system.

The special recoil time of flight (TOF) scintillation counters were located just behind the WSCs. These counters measured 6" X 72" X 1" thick and had a RCA 8575 PMT viewing the long dimension on each end.

There were 6 such counters on each arm, while a seventh counter had a transverse dimension of 12" rather than 6", but was otherwise similar. Another array of four 12" X 72" X 1" counters was located on the opposite

Figure 3-5. Schematic diagram of one arm of the recoil proton detector.

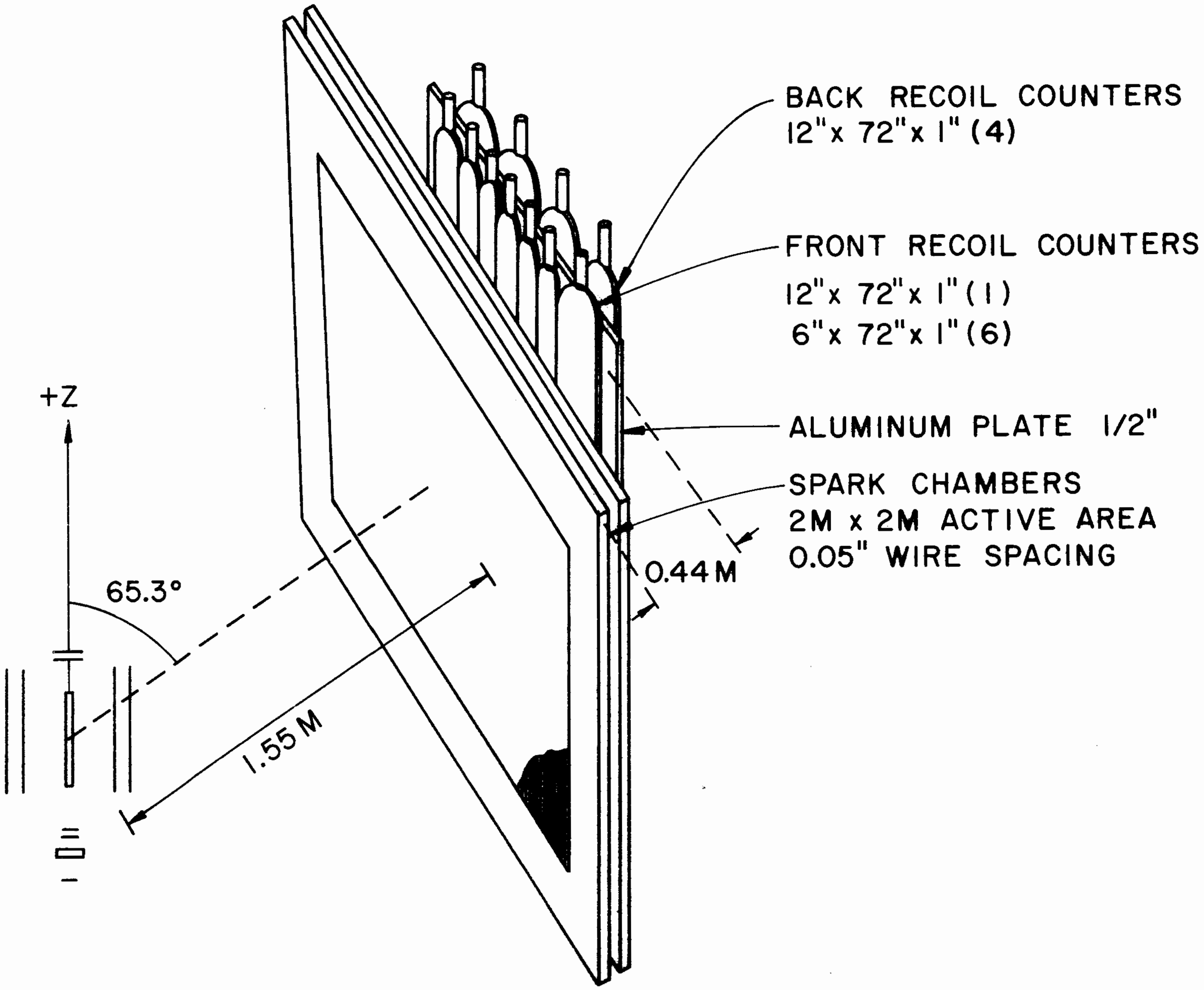
BACK RECOIL COUNTERS
12"x 72"x 1" (4)
FRONT RECOIL COUNTERS
12"x 72"x 1" (1)
6"x 72"x 1" (6)
ALUMINUM PLATE 1/2"
SPARK CHAMBERS
2M x 2M ACTIVE AREA
0.05" WIRE SPACING
0.44 M
+Z
65.3°
1.55 M

side of a 1/2" aluminum plate from the TOF counters. These 4 counters were used to measure dE/dX for the recoil particle after passing through the 1/2" plate. Most pions hitting the recoil detector would not have sufficient energy to penetrate the aluminum plate, while protons in the desired momentum range should reach the back counters and produce a large pulse height corresponding to a large dE/dX. (Although the back counters seemed to be working during the experiment, the data from them was found to be unreliable and was subsequently not used. This reduced the range of recoil particle momenta in which protons could be distinquished from pions.)

Figure 3-6 shows the electronics associated with each TOF counter. The output of each PMT, after passing through a LFO, was sent to an analog-to-digital converter (ADC) and to a time-to-digital converter (TDC) via a discriminator. A third output was sent, along with the output of the other PMT, to an adder-integrator. This circuit summed the two outputs and integrated the result with a suitable time constant. The output of the adder-integrator was an analog signal with a voltage proportional to the total charge from the two PMTs. This signal was then discriminated with a threshold chosen to reject minimum ionizing particles (i.e., pions).

The other device shown in Figure 3-6 is a mean timer, or chronotron. Its function, given the times at which the two PMT pulses arrived, was to generate a timing pulse independent of where the counter was hit. This timing pulse gated the output of the discriminator on the adder-integrator to establish the timing relationship of the proton trigger to the LH2 trigger.

Figure 3-6. Recoil counter time of flight and pulse height discrimination electronics.

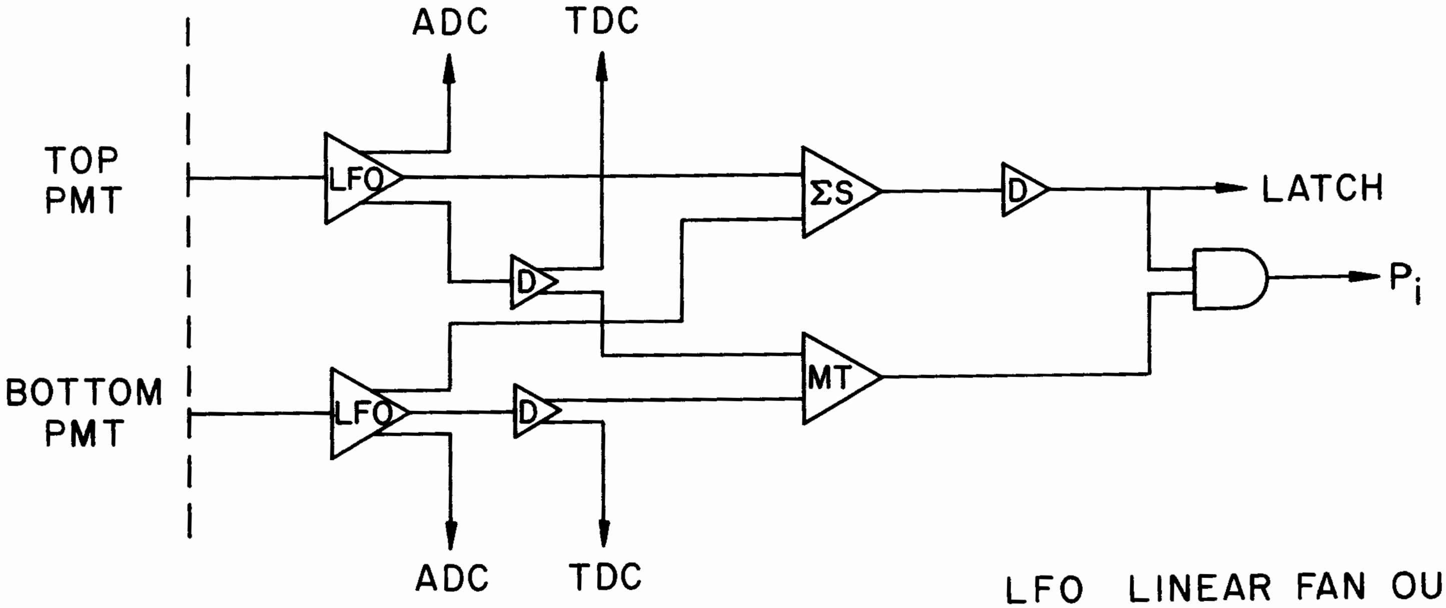

LFO	LINEAR FAN OUT
D	DISCRIMINATOR
ΣS	ADDER - INTEGRATOR
MT	MEAN TIMER

To further restrict the angles of the recoil protons with respect to the beam direction, the recoil MWPCs were incorporated into the trigger. The innermost MWPC on either side of the LH2 target was electronically divided into 3 parts (these were shown in Figure 3-3, designated WW1, EW1, etc.). A signal was available from each section, the magnitude of which was proportional to the number of wires in that section which had been hit. Figure 3-7 shows the logic associated with combining the various MWPC sections with the trigger signals from the TOF counters. The WP1, EP1, etc., refer to the output of the logic in Figure 3-6 for each of the TOF counters (the counters furthest upstream were WP1 and EP1). The MWPCs were used only in the 1 MU.P trigger.

One additional timing requirement was made to improve the pion rejection ratio. This involved placing a rough time of flight cut of from 12 to 32 nanoseconds on the recoil particle. Considering that a speed of light particle would traverse the 2 meter distance in approximately 6.67 nanoseconds, this amounts to a cut on v/c of the particle of from 0.21 to 0.56. Not incidentally, this cut, in combination with the angle restrictions, also achieves the desired range of missing mass ($3.0 < M_X < 7.0$ Gev/c^2) for the forward-going particles.

Since muons were required in two of the triggers (1MU.P and 2MU) a description of the muon detection is appropriate. Two scintillation counter hodoscopes, placed downstream of a 2.2 meter thick steel hadron absorber (see Figure 3-1), were responsible for detecting muons. These hodoscopes, the M′ and P, are shown in Figure 3-8. The Bow-tie shape of the P hodoscope was designed to discriminate against low mass di-muon pairs. For the 2MU trigger, the P alone was used. In particular, only the counters actually in the Bow-tie part were used, with all counters in a

Figure 3-7. Proton trigger formation logic.

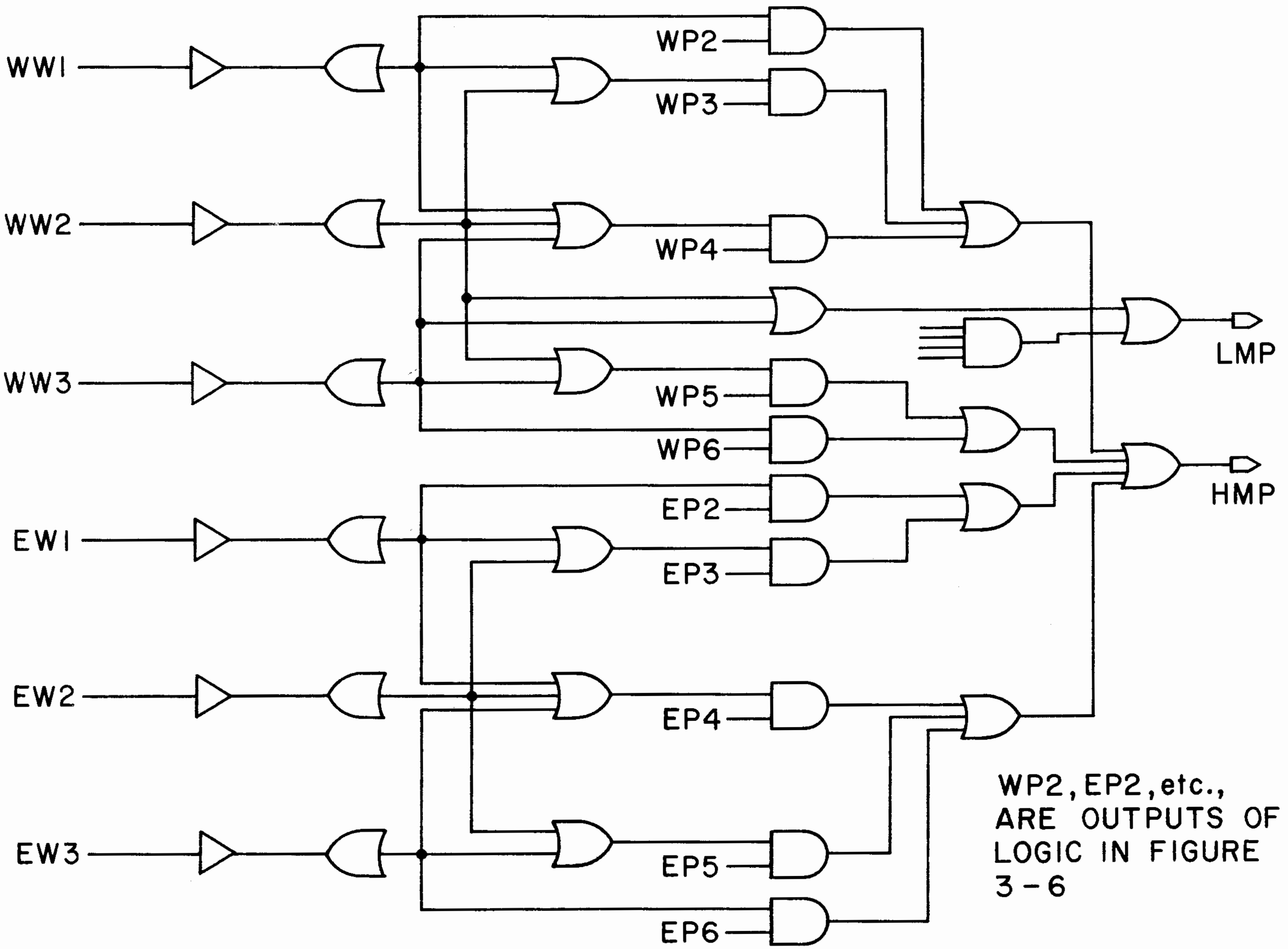

WP2, EP2, etc., ARE OUTPUTS OF LOGIC IN FIGURE 3-6

Figure 3-8. Muon detection hodoscopes M´ and P as viewed from downstream. Asterisks show counters included in the 1 MU.P trigger.

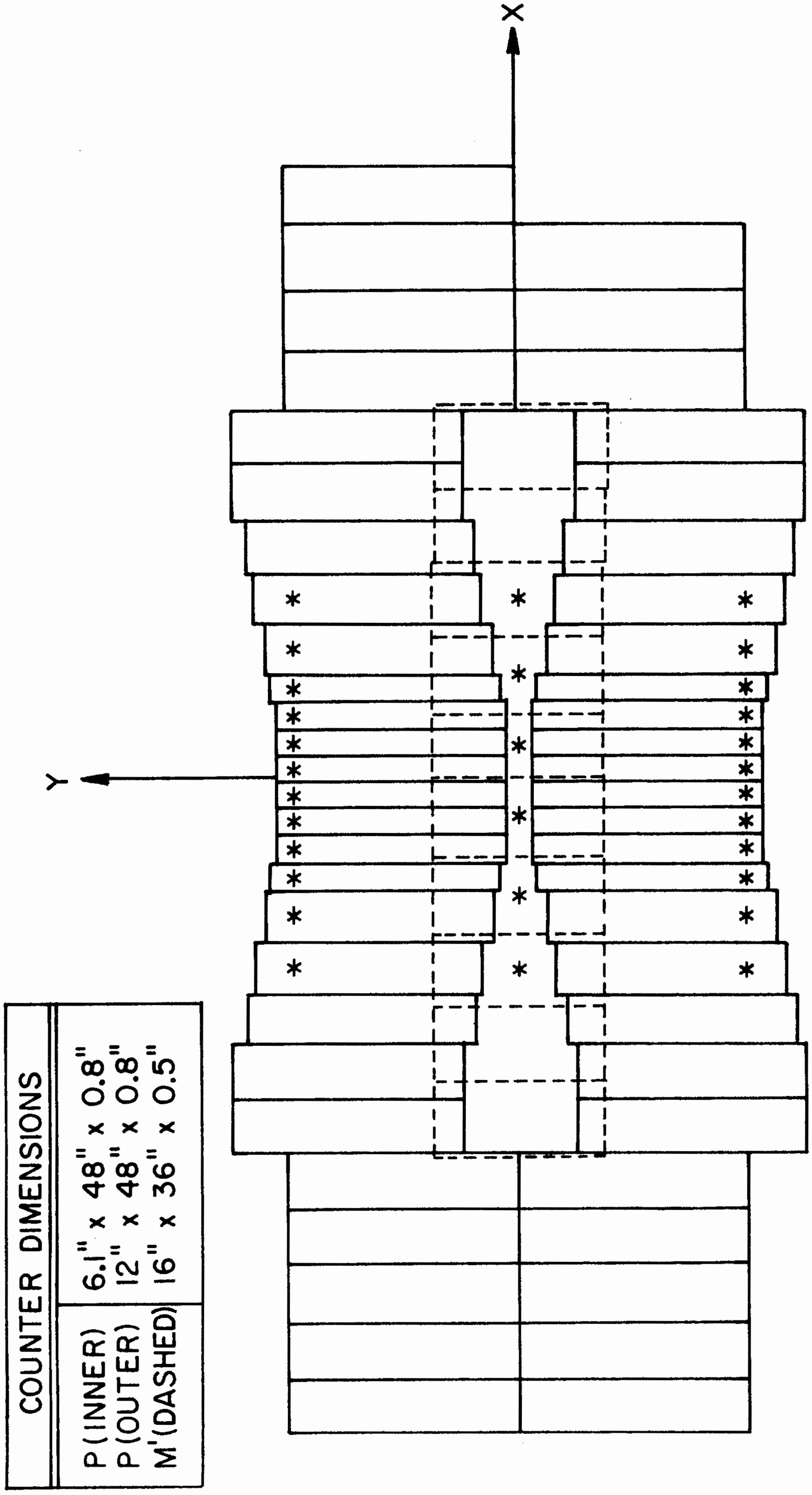

COUNTER DIMENSIONS	
P (INNER)	6.1" x 48" x 0.8"
P (OUTER)	12" x 48" x 0.8"
M'(DASHED)	16" x 36" x 0.5"

quadrant ORed together. The 2MU trigger then required two diagonally opposing quadrants each hit by a muon.

Parts of both the P and M′ hodoscopes were used in the 1 MU.P trigger, with the 1 MU part of the trigger coming from the OR of the discriminated signals from certain counters in both hodoscopes. The counters used in the 1 MU.P trigger are marked by asterisks in Figure 3-8. The counters in ther outer regions were not used because the trigger rate from the decay of lower momentum pions was much larger. Since the probability of a pion decaying before the hadron absorber is nearly inversely proportional to its momentum, and the pion momentum spectrum falls rapidly with increasing momentum, the trigger rate from pion decay decreases even more rapidly as the minimum momentum of the triggering particle is increased. The minimum momentum for the muon in the 1 MU.P trigger was about 30 Gev/c.

Figure 3-9 shows the logic associated with the formation of the event trigger. Simply adding or removing pins from the logic units at the final level allowed control over the merging of the various triggers. The signals enclosed in parentheses were formed by the logic shown in Figure 3-4.

3.3 Trackfinding Equipment

In order to determine the momentum of the charged particles produced in the interactions, some means of recording the particles′ tracks both before and after the momentum analyzing magnet must be provided. In this regard, the CCM spectrometer was used essentially unchanged from earlier experiments. The apparatus was shown in Figure 3-1. Note the 20 MWPC planes upstream of the CCM and the 20 WSC planes downstream. Also indicated are the timing hodoscopes, the 18 cell gas Cerenkov counter, the lead glass Cerenkov counter, and the hadron absorber. All chambers

Figure 3-9. Final event trigger logic.

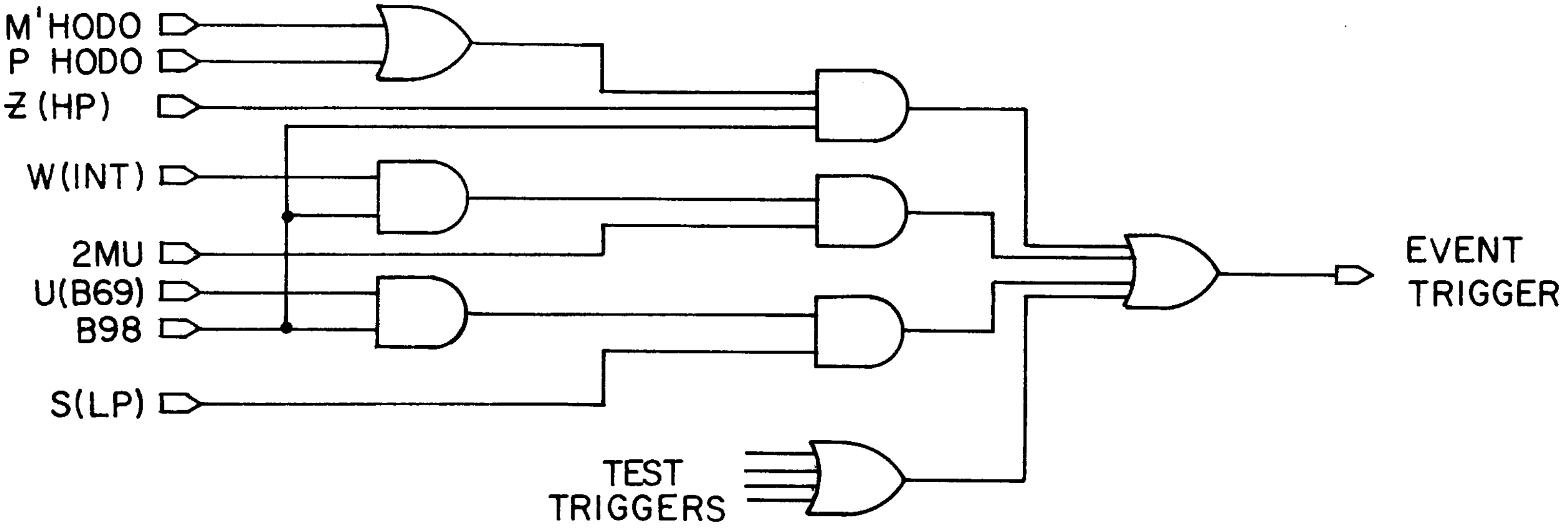

SIGNALS IN PARENTHESES
FROM FIG. 3-4.

upstream of the CCM were MWPCs, while all those downstream were WSCs.

The 20 MWPC planes originated from two places. The University of Chicago installed the 5 X-Y pairs of 1 m X 1 m area and 1.5 mm wire spacing. The University of Illinois supplied 5 modules of 2 planes each with an active area of 80 cm X 80 cm. These 80 cm chambers were designed as XY planes, but two modules were used as UV planes by physically tilting the chambers by ±26 degrees. Wire spacing in the 80 cm chambers was 1/8". The MWPC planes were not particularly efficient (average efficiency was about 85%) and suffered from light-ups (most wires in a chamber showing hits) and readout problems.

The spark chambers also came from two sources: The University of Chicago and Harvard. The construction of all the planes was similar with 1.25 mm wire spacing. The wires in the UV type planes were tilted by $\pm$arctan(1/8) to the vertical. There were no Y planes downstream, as the y information from the tilted planes was sufficient for track linking purposes.

The Chicago chambers were organized as 3 modules of 4 planes each and had an active area of 4 m X 2 m. The readout system consisted of capacitively couping each wire to an input of a long parallel to serial shift register (Proudfoot, 1978).

The Harvard WSCs came in two sizes: 6 m X 2 m and 4 m X 2 m. Both sizes used a magnetostrictive wand readout system (Proudfoot,1978). The 8 larger planes were located just downstream of the Oxford 18 cell gas Cerenkov counter. The 4 m X 2 m WSCs were positioned between the hadron absorber and the P hodoscope, and thus would have been used only for tracking muons if they had been efficient enough.

3.4 Particle Identification and Timing Equipment

This equipment consisted of several counter hodoscopes for track timing and an 18 cell gas Cerenkov counter to provide some information on the identity of the charged hadrons. Timing information was necessary to reject spurious tracks (false or those produced by particles from other interactions within the several microsecond memory time of the WSCs).

The counter hodoscopes, refered to as the G, H, H´, M, N, M´ and P, with the exception of the M´ and P as discussed previously, were used unchanged from the previous experiment. For drawings of these hodoscopes, consult the thesis of R. Hicks (Hicks,1978). The position of these hodoscopes was shown in Figure 3-1.

The Oxford 18 cell gas Cerenkov counter, whose location was also showm in Figure 3-1, helped to discriminate between pions and heavier hadrons (mostly kaons and protons) within a limited range of particle momenta. The gas was dry nitrogen at atmospheric temperature and pressure, and the radiator length was 1.2 m. The Cerenkov light was focused by the 60.8 cm X 110 cm parabolic mirrors onto the RCA 4522 5" PMTs. The effective momentum range was approximately 8-24 Gev/c for the separation of pions and kaons (only partial separation was possible due to the small number of photoelectrons for a v=c pion). For a complete description of the Oxford Cerenkov counter, consult the thesis of J. Proudfoot (Proudfoot, 1978).

The last major addition to the CCM spectrometer for this experiment was a lead glass Cerenkov counter array from Tufts University and The University of Massachusetts. It was configured so as to detect photons in the 2-30 Gev/c momentum range, although its location also made it a beam dump. The detector consisted of an 8 X 10 array of lead glass Cerenkov counters as shown in Figure 3-10. The squares represent the individual counters in the array as seen from upstream (beam's eye view). The shaded squares indicate counters which were either missing or otherwise badly behaved. The location of the array was shown in Figure 3-1. The details of the counter construction are illustrated in Figure 3-11.

The individual counters utilized a 6.35 cm X 6.35 cm X 58.4 cm block of Schott type SF-2 lead glass. This glass has an index of refraction of 1.67 and is 51% PbO by weight. An Amperex XP-2020 photomultiplier tube was coupled to the block with a 3.2 cm X 3.2 cm X 10.2 cm *light pipe* also of lead glass. Dupont HE-10 cement was used throughout. The whole counter was wrapped in aluminum foil and black electrical tape. A Bakelite plate was cemented to the end opposite the PMT, and held the light-emitting diode (a Monsanto MV5222) used for monitoring the gain of the PMT.

The PMT anode signals were attenuated to achieve the desired energy range and then digitized by Lecroy Model 1248 and 2249 ADCs. The ADCs were read through a CAMAC system connected to the PDP-11 computer dedicated to the lead glass detector. This computer also controlled the LED calibration sequence, and monitored the PMT high voltages through a multiplexed digital voltmeter. Details of the lead glass calibration system and data analysis are presented in the Appendix.

Figure 3-10. Schematic representation of the lead glass Cerenkov counter array. Shaded squares indicate missing or ill-behaved counters.

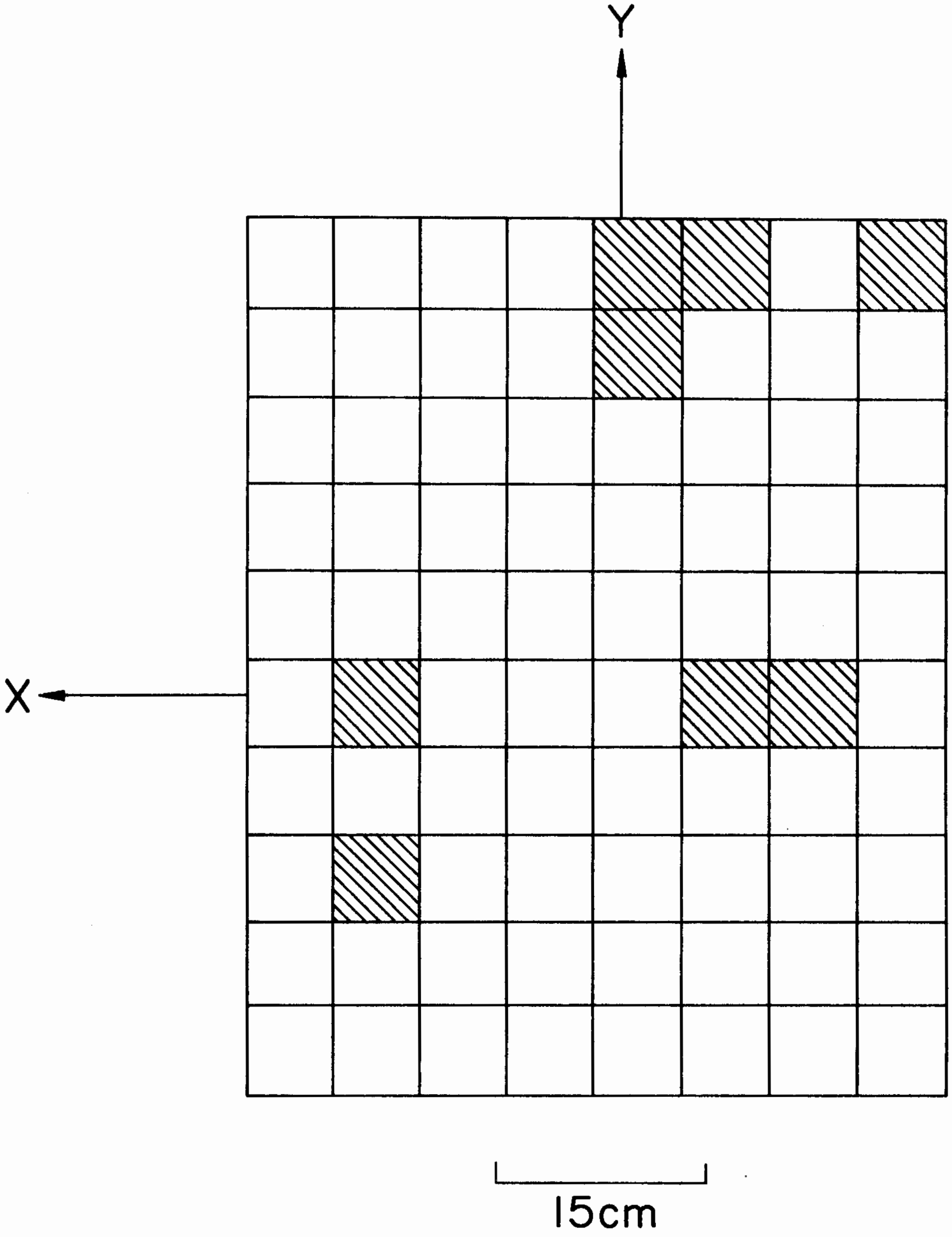
Y
X
15cm

Figure 3-11. Details of lead glass Cerenkov counter construction

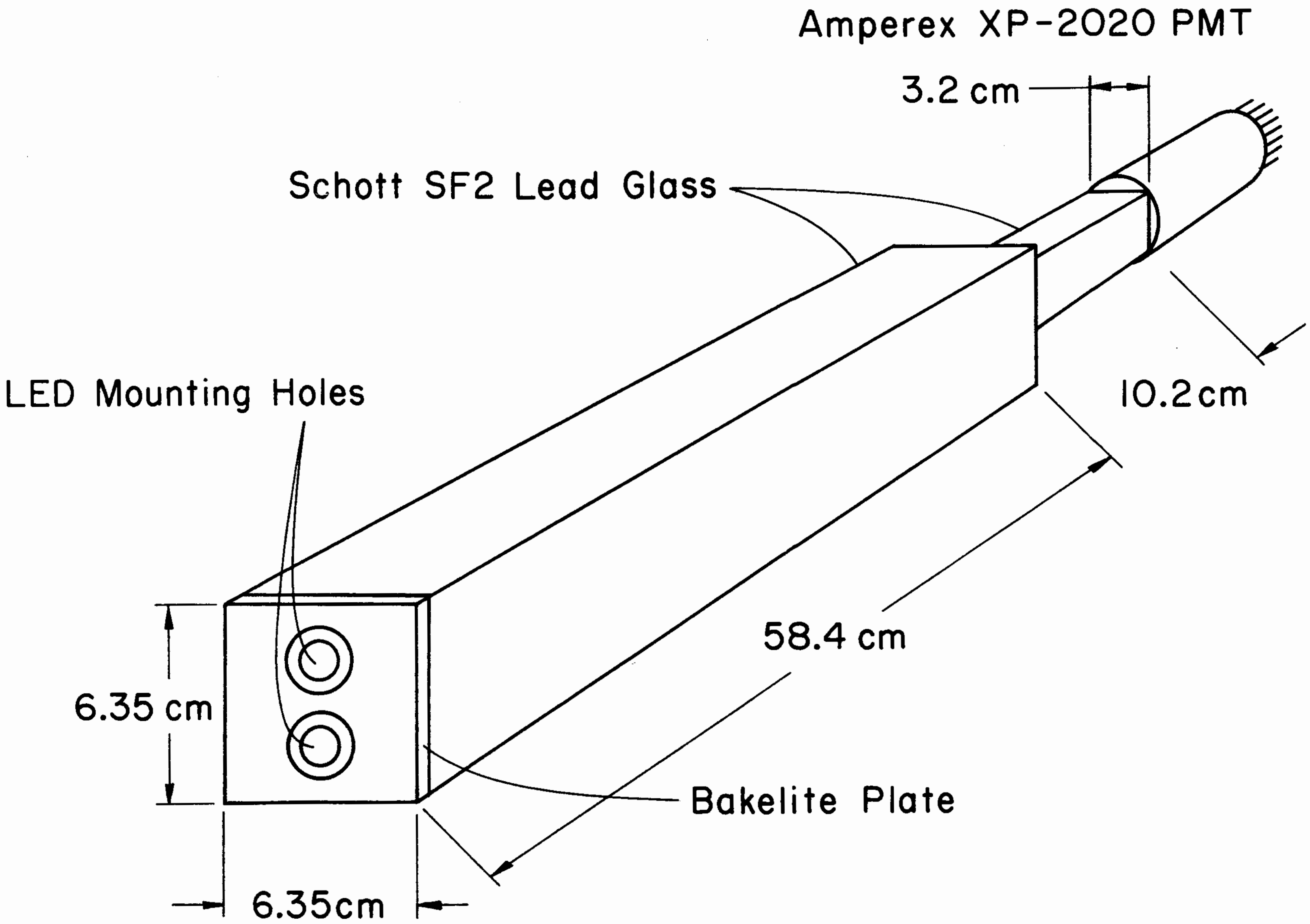
Amperex XP-2020 PMT
3.2 cm
Schott SF2 Lead Glass
LED Mounting Holes
10.2 cm
58.4 cm
6.35 cm
Bakelite Plate
6.35cm

CHAPTER 4

PRELIMINARY DATA ANALYSIS

The analysis of the data can best be described in three parts. The initial phase was the reconstruction of the tracks in the MWPCs and WSCs. The intermediate phase was concerned with particle identification and neutral particle reconstruction. In the final stage of the analysis, the invariant mass spectra of various combinations of the particles found in the first two stages were studied.

I will briefly describe the trackfinding process which had been modified somewhat from the earlier experiments (Hicks,1978). The reconstruction of the neutral strange particles $(K0,\Lambda^{0},\overline{\Lambda}^{0})$ will be covered in detail since I was responsible for the development of the algorithms used. The details of the lead glass data analysis are presented in the Appendix, since I also developed the algorithms for that analysis. I will describe the main features of the Cerenkov data analysis, for although I did not use the information to obtain charged kaons, I did make use of the results to help eliminate certain tracks (see chapter 5).

The details of the final analysis will be covered in Chapter 5, while the rest of this chapter will be devoted to the track reconstruction and the intermediate analysis.

4.1 Track Reconstruction

There were four distinct regions in which tracks were reconstructed:

1. Beam MWPCs
2. Recoil proton detector

3. Upstream (of the CCM) MWPCs
4. Downstream WSCs

First the raw data in the form of wire addresses had to be transformed into real coordinates. The only case worth noting involved the magnetostrictive readout system on the 6 m X 2 m WSCs. There were non-uniformities in the signal velocity along the magnetostrictive wands. Thus a correction (different for each plane) was applied which was a function of the uncorrected position and the particular run (The correction changed with time).

4.1.1 Beam MWPCs

The beam MWPCs and hodoscopes were used to reconstruct the track of the beam particle. If there was not enough information for a good fit, a track was fabricated from the primary vertex position and the nominal beam trajectory.

4.1.2 Recoil Proton Detector

The front recoil scintillation counters were first searched for the counter which had caused the trigger. The position of this counter was used as a guide to searching for relevant sparks in the recoil MWPCs and WSCs. Sparks in at least three out of the four X planes and one out of the two Y planes were needed for a recoil track to be found. The fit in the Y projection was constrained by including the point X=0,Y=0 (the beam line). This was done because the only Y measuring planes were situated about 1.5 m away from the beam line, and separated by only about 30 cm.

When the recoil track had been found, the recoil path length was determined, as well as the time of flight of the recoil particle. The calibration of the recoil time of flight has been discussed in detail in the thesis of W. W. MacKay (MacKay, 1980), who was responsible for the recoil proton analysis.

4.1.3 Upstream MWPC Trackfinding

The first four X-Y pairs of 1 m X 1 m MWPCs were searched for straight tracks separately in X and Y. A minimum of three hits out of the four possible were required in each projection. A fit of the primary vertex was done using these tracks, and the beam and recoil tracks, if they had been found. The recoil and beam tracks were initially given large weights, while the final fit assigned equal weights to all tracks still in consideration. The vertex, if found, was used as a guide to search the MWPCs for any tracks with only two hits in a projection and consistent with the vertex.

4.1.4 Downstream WSC Trackfinding

An extra step was necessary in the downstream trackfinding, since the WSCs had memory times on the order of microseconds. This preliminary step involved searching for tracks consistent with beam tracks and removing the associated sparks from further consideration. This helped to keep the trackfinding algorithms from overflowing due to excessive numbers of tracks, since the parallel nature of stale beam tracks combined with the uniform spacing of the WSC planes led to many more possible tracks than were really present. Apart from this cut on the data, the criterion for downstream tracks was at least three sparks in each of the X and Y projections. The tracks thus formed were discarded if they did not project into a 2.5 m wide window at the center of the CCM.

4.1.5 Track Linking

This phase of the trackfinding process involved the matching of X and Y projections in the upstream MWPCs to one another, and to the space tracks found in the WSCs downstream. There were two possible ways of accomplishing these tasks. The most straightforward method was to utilize the X-Y correlations provided (when they worked) by the tilted 80 cm MWPCs. The other method used the fact that the downstream tracks were full space tracks, that is, the X projections and Y projections were correlated by the WSC planes with tilted wires. In this method the first step was to associate a projection of a downstream track with an upstream track projection. Then the other projection of the downstream track was used to search for an upstream projection which matched. The linking process was typically more complex than indicated by the above description, since tracks were being bent in the X projection, while the linking resolution was poor in the Y projection because there were no strictly Y measuring planes downstream of the CCM.

If either upstream projection of a downstream track was missing, that projection was fabricated assuming the track originated from the primary vertex. Such tracks were flagged to indicate that they were not as good as the fully linked tracks.

The track momenta were initially determined with a hard edge radius approximation of the CCM (Pordes, 1976). Each track was then subjected to a least squares fit utilizing all of the hits associated with the track and a parametrization of the magnetic field.

Finally, left over upstream track projections were used to look in the 80 cm MWPCs for hits consistent with "low-momentum" tracks which may have been deflected away from the downstream WSCs by the CCM.

The trackfinding results along with the timing hodoscope data, scalers, Cerenkov data, and lead glass data were written onto a new set of so-called "scaled" magnetic tapes, which became the source of input to the second stage of the analysis.

The intermediate stage of the analysis consisted of three unrelated parts:

1. Cerenkov counter data analysis
2. Reconstruction of neutral kaon (KO) decays
3. Lead glass data analysis

The Cerenkov data analysis was performed by E. B. Smith and will be covered in detail in his thesis. I will give only a rudimentary description of the algorithms. The reconstruction of the neutral kaons (KO´s) which decayed in the first 2 m downstream of the LH2 target was performed by myself, as was the lead glass data analysis which will be covered in the Appendix.

4.2 Cerenkov Data Analysis

The Cerenkov data was used to provide a partial discrimination between pions and heavier particles such as kaons and protons. About 10% of all particles passing through the CCM were heavier than pions.

The algorithms used for the Cerenkov analysis attempted to compute the probabilities that a particle passing through it was either 1) a pion or 2) a kaon. For large numbers of tracks, this procedure can become quite complicated and ambiguous.

The following description of the algorithms will convey the general approach to the analysis. For details of the analysis, the reader should consult the thesis of E. B. Smith (Smith, 1980), who developed the algorithms.

The process begins by calculating the fraction of the maximum ($\beta = 1$) Cerenkov light that the particle would contribute to the cell(s), assuming that it was 1) an average pion and 2) an average kaon. By definition, an average particle of mass M and momentum P, passing through a medium with index of refraction N, should produce a fraction F of the v = c light, where F is given by:

$$F = 1 - [(P/M)^2 \times (N^2 - 1)]^{-1} \quad \text{for } P/E > 1/N = \beta_t$$

β_t is the threshold velocity which is equal to the velocity of light in the medium.

This fraction must then be corrected for the non-zero slope of the particle's path with respect to the normal to the mirror plane, and for sharing (if any) of the light with adjacent cells. The correction for the slope of the particle's path involves adjusting the amount of light produced according to the increase in amount of path length in the gas, and distorting the Cerenkov light circle into an ellipse. The correction for light sharing consists of dividing the Cerenkov circle along one or more chords corresponding to the boundaries of the cells involved, and multiplying F for a given cell by the ratio of the area of the circle falling on that cell to the total area of the circle. In the case of sharing of light, the particle contributes to the total light in each of the cells involved. The sharing correction differs for the pion and kaon hypotheses due to the different diameters of the Cerenkov light rings. The tracks flagged as muons were given special treatment. The expected pulse height for a muon of the given momentum was added to the total calculated for a given set of identifications. The muon track was then eliminated from consideration as the other tracks were identified.

The easiest particle identifications were made as the fraction F was calculated. The identification was based on the value of a ratio of probabilities. For a given hypothesis, pion or kaon, the probability that the observed pulse height from the cell was due to the light from the particle in question was calculated as:

$$P(Y:\langle n\rangle) = e^{-\langle n\rangle}/\sqrt{2\pi}\sum_{N=0}^{\infty} \frac{e^{-\left[\frac{(Y-N\times G)^2}{2(\sigma_P^2+N\sigma_G^2)}\right]}}{\sqrt{\sigma_P^2+N\sigma_G^2}} \frac{\langle n\rangle^N}{N!}$$

This formula is based on the Poissonian probability distribution for obtaining n photo-electrons when the average number of photo-electrons is <n>, and the assumption that the gain of the PMT can be parametrized as having a Gaussian distribution with mean G and variance σ_G^2. For n photo-electrons, this gives a Gaussian pulse height spectrum with mean n x G and variance n x $\sigma_G^2 + \sigma_P^2$, where σ_P^2 is the variance in the ADC pedestal. The total probability of obtaining the observed pulse height is simply the sum of the probabilities of getting n = 0,1,2,... photo-electrons which gave that pulse height.

For the simple case of one particle contributing light to a cell and producing a pulse height Y, the appropriate ratio of probabilities is:

$$R(K/\pi) = P(Y:\langle n_K\rangle)/P(Y:\langle n_\pi\rangle)$$

with $\langle n_K\rangle$ and $\langle n_\pi\rangle$ the average number of photo-electrons expected from this particle if it were a kaon and a pion, respectively. If R was greater than 1 the assignment of kaon was made, while if R was less than 1 the assignment of pion was made. If the particle's velocity was significantly above the kaon threshold or below the pion threshold, R was equal to 1, indicating a fundamentally ambiguous situation. The value of $R(K/\pi)$ is finally scaled by multiplying by the expected fraction of heavy particles, 0.0989.

When more than one particle contribute light to a cell, the procedure was to iteratively pick a particle and, adding its contribution for each of the two hypotheses in turn to the total of the contributions from the previously identified particles, compute the ratio R as before.

To summarize the Cerenkov analysis simply, the basic approach was to chose the set of particle identifications which would have given the amount of Cerenkov light closest to that which was observed. In the calculation of this expected pulse height, the Poissonian statistics of the PMT output, and the possible fluctuations of the PMT gain and the ADC pedestal were taken into account.

4.3 Reconstruction of Neutral Kaons

This section covers the reconstruction of neutral kaons (K0´s). The neutral short-lived kaon decays 68% of the time into $\pi^+\pi^-$. These decays can be reconstructed if they occur in the region between the LH2 target and the first MWPC plane. A few preliminary remarks will help in the understanding of this part of the analysis.

4.3.1 Track Linking

As noted in the section on trackfinding, tracks were divided into three categories, depending on where (i.e., upstream of the CCM, downstream of the CCM, or both) they were found.

The three types were:

1. Linked - found both upstream and downstream
2. Unlinked - found downstream only
3. Low momentum - found upstream only

Since the reconstruction of the K0's involved finding a separate vertex downstream of the primary vertex, only tracks which were found in the MWPCs could be used. Those tracks found only downstream were obviously not reconstructed in the MWPCs and thus were constrained to originate from the primary vertex so that their momenta could be determined.

The "low momentum" tracks were those tracks found by a particular program in the trackfinding analysis. Thus they were not necessarily restricted to very low momenta. In fact, about 70% of the "low momentum" tracks had momenta high enough that they should have passed through the timing hodoscopes and the WSCs. I discovered (quite by accident while looking at Monte Carlo events) that some of these tracks should have been linked to an unlinked downstream track. I then investigated the linking parameters and derived cuts which would pair up these pieces of a full track. When a link was found, the momentum was redetermined with a hard edge radius magnet approximation. A low momentum and unlinked track were linked in this fashion in about 10% of the events.

4.3.2 Track Retiming

Track timing was done during the trackfinding process. However, there were many cases in which several tracks passed through the same hodoscope element. This lead to problems when trying to remove the out of time tracks (mostly unlinked), since up to 30% of all tracks were ambiguous in at least one counter. Another problem was the fact that many of the low momentum tracks should have, given their momentum, passed through a counter. However, they were not checked for timing information by the original timing algorithm. Since the unlinked tracks were not used in the KO reconstruction, the main consideration during this stage of the analysis was the elimination of the out-of-time "stubs" (bubble chamber terminology for low-momentum tracks).

To rememdy these problems, I developed a more sophisticated timing algorithm which could decide whether a track was:

1. Uniquely in-time (one track through fired counter)
2. Ambiguously in-time (more than one track through fired counter)
3. Out of time (one or more tracks through unfired counter)

For each track, the total number of counters in each category was kept. Actually, two such sets of numbers were kept - one set for the general timing hodoscopes (G,H,H´) and one set for the muon timing hodoscopes (N,M,M´,P). Some of the ambiguous cases were solved by using the timing information from the other hodoscopes. For example, if tracks 1 and 2, say, pass through the same counter in one hodoscope, the result will be ambiguous. However, if either of the tracks is found to be out of time in another counter, and is not uniquely in-time anywhere, that track will be called out of time and the other will be uniquely in-time in the previously ambiguous counter. If both tracks happen to be ambiguous or out of time in the other hodoscopes, the result will be left ambiguous.

In order to check the low momentum tracks for timing, a downstream track had to be fabricated. The momentum and upstream track parameters determined by the trackfinder were used in a hard edge radius magnet approximation discussed by Pordes (Pordes, 1976) with a small modification.

The modification was determined by attempting to reproduce the downstream track of linked tracks. A satisfactory adjustment consisted of increasing the angle of deflection in absolute value by the quantity $0.36/P^2$ (radians), where P is the momentum in Gev/c. The formula given by the hard radius approximation for the deflection angle, φ , in terms of the track's radius of curvature, ρ , and impact parameter, B, is:

$$\varphi = \arctan[\sqrt{(R^2 - B^2)}/(|\rho| + \text{CHARGE} \times B)]$$

where R is the effective radius of the CCM (2.5 m), and CHARGE is the particle's charge.

After the tracks were retimed, they were sent through the Cerenkov analysis once again. The Cerenkov analysis had been done previously, but in a slightly different manner (see section 4.2) The two differences were that:

1. "Muons" were treated as pions
2. Timing and $R(K/\pi)$ were used to weed out tracks before a second pass

Since most of the muons in the 1 MU.P trigger had momenta greater than 30 Gev/c, they produced (at least within the Cerenkov's ability to measure) the same amount of Cerenkov light that a pion of the same momentum produced. In addition, many of the "muons" probably were not even muons by the time they reached the Cerenkov counter, since most of the triggers were due to hadrons penetrating the hadron absorber or to muons from pion decay.

Since the results of the Cerenkov analysis depend upon the particular set of tracks which it is given, those tracks must be chosen carefully. All of the tracks were used on the initial pass through the analysis. To determine appropriate cuts for the second pass, I studied the correlation between the "in-timeness" and the R(K/π) for tracks in various momentum ranges. By looking at the fraction of tracks in a particular momentum interval which had R(K/π) less than a given value, I was able to determine a sliding cut on the value of R(K/π) which depended on both the type of track and its timing. A few of the plots which were used are shown in Figure 4-1. The abscissa is the value of the cut on R(K/π) while the ordinate is the fraction of tracks whose R(K/π) is less than the cut. The momentum range used was 12-20 Gev/c. This momentum range was above the pion threshold (8 Gev/c) and below the kaon threshold (24 Gev/c).

Tracks which were ambiguous in the Cerenkov (i.e., those with R(K/π)=0.0989, the expected fraction of heavy particles) were not used. The normal division between pions and heavy particles was R(K/π) = 0.25. Note the differing shapes depending on track type and timing. For example, the circled points in Figure 4-1 give the curve for linked tracks which were uniquely in-time in 2 counters and not ambiguous or out of time anywhere. By contrast, the crosses indicate the curve for unlinked tracks which were out of time in 2 counters and not ambiguous or in time anywhere. The triangles show the curve for unlinked tracks which were ambiguous in 1 counter and out of time in 1 counter. These are among the tracks which would have been called in time by the original timing algorithm. Finally, the squares indicate the curve for the unlinked tracks which were in time according to the original timing algorithm but which were called out of time by my timing algorithm. These plots show unmistakably the correlation between timing and R(K/π). The reason is simply that out of time tracks have no Cerenkov light associated with them and are thus identified as heavy particles (kaons).

Figure 4-1. Correlation between timing and Cerenkov results for indicated combinations of track type and track timing. The squares correspond to tracks which were called in-time by the original timing algorithms, but called out of time by my timing algorithms.

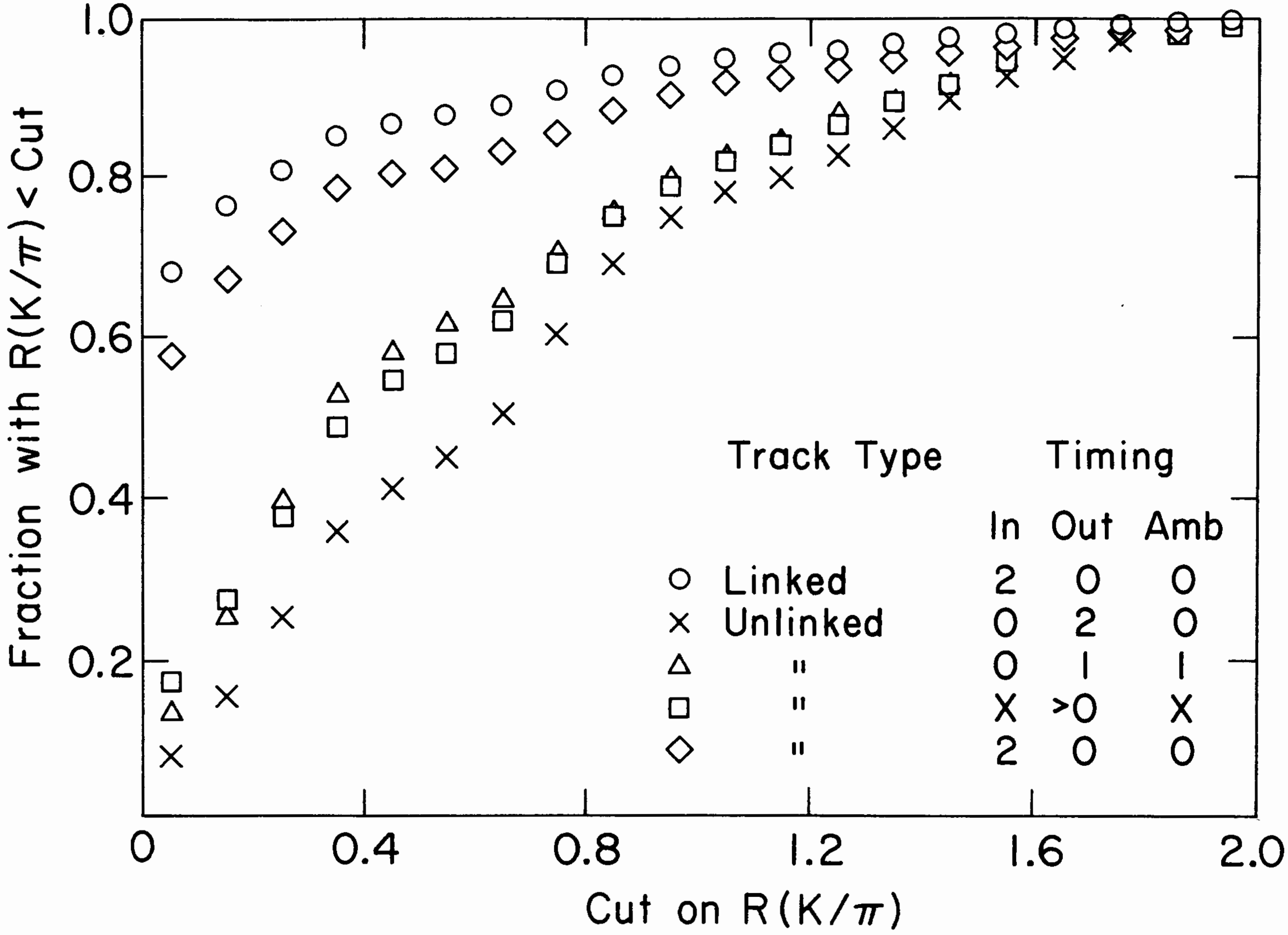
1.0
0.8
0.6
0.4
0.2
Fraction with R(K/π) < Cut
0
0.4
0.8
1.2
1.6
2.0
Cut on R(K/π)
Track Type
Timing
In Out Amb
○ Linked 2 0 0
× Unlinked 0 2 0
△ " 0 1 1
□ " X >0 X
◇ " 2 0 0

The cuts I chose to use for rejecting out of time tracks before the second pass through the Cerenkov analysis essentially made use of the fact that the Cerenkov counter was, except for heavy particles, a timing device. That is, tracks that were marginally in time, such as being both in time and out of time, were required to have a relatively small $R(K/\pi)$ corresponding to Cerenkov light for the track. Of course, this type of cut removed the tracks from heavy particles which happened to have marginal timing but the probability of this occurring was small compared to the probability that the track was really out of time.

The final set of tracks used for the Cerenkov analysis was also required to have a total longitudinal component of momentum which exceeded the beam particles momentum by not more than 4 Gev/c. If this was not already the case after the cuts described above had been applied, progressively more stringent timing cuts were applied until momentum conservation was obtained.

4.3.3 Error Scaling

The last preliminary remark concerns the scaling of the errors which were used to compute various chi-squares. The covariance matrix resulting from the final fit of a track to the sparks used to form it was the source from which the errors were calculated. It was found that the errors were not realistic unless scaled by a factor 3. One physical distribution used to determine this factor was the deviation of the fitted vertex from the Z value given by the extrapolation of the recoil proton track to $X = 0$ (i.e., the beam line). If the deviation is divided by the probable error in Z of the fitted vertex, the resulting distribution should be approximately Gaussian with unit standard deviation. Of course, there is a contamination from events in which the recoil track did not originate from the main interaction vertex. Figure 4-2 shows a typical distribution obtained with the rms errors scaled by a factor of 3, and using only events with 3 or more tracks used in the vertex fit at the 5% confidence level.

4.3.4 KO Reconstruction for Recoil Proton Events

The reconstruction of KO´s in events with recoil protons was simplified in a sense due to the fact that the proton track is believed to extrapolate back to the primary vertex with little error. In those events with a recoil proton track, an initial vertex fit could thus be avoided by simply taking the Z of the primary vertex to be that determined by the recoil track. The algorithm developed for finding KO´s worked schematically as follows:

1. Find all neutral pairs of tracks having a vertex with chi-square of 10 or less (1 degree of freedom) and distance of closest approach less than 1 cm.
2. Reject neutral pairs with vertex within 20 cm of recoil proton
3. Fit (geometrically) all neutral pairs passing previous steps

Each of the steps above deserves an explanation. In the first step, the distance of closest approach (DCA) and chi-square (χ_v^2) are calculated for each unique neutral pair of tracks. Only those pairs having a vertex with a DCA of 1 cm or less and a χ_v^2 of 10 or less are given further consideration The χ^2 of the pair vertex is calculated as:

$$\chi_v^2 = \sum_{i=1}^{2} [(X_v - X_i)^2/\delta X_i^2 + (Y_v - Y_i)^2/\delta Y_i^2]$$

where X_i and Y_i are the coordinates of track i at the Z position of the pair vertex, and X_v, Y_v are the coordinates of the pair vertex. The errors, δX_i, δY_i, on the coordinates of the tracks are calculated from the covariance matrix resulting from the fit of each track to its sparks. Thus

Figure 4-2. Distribution of fitted vertex about the Z-value obtained by extrapolation of the recoil track to the beam line. The deviations of the vertex are divided by the probable error in the Z position of the vertex. The probable errors have been increased by a factor of 3 to obtain this distribution. Z_ρ = proton Z; Z_M = main vertex Z.

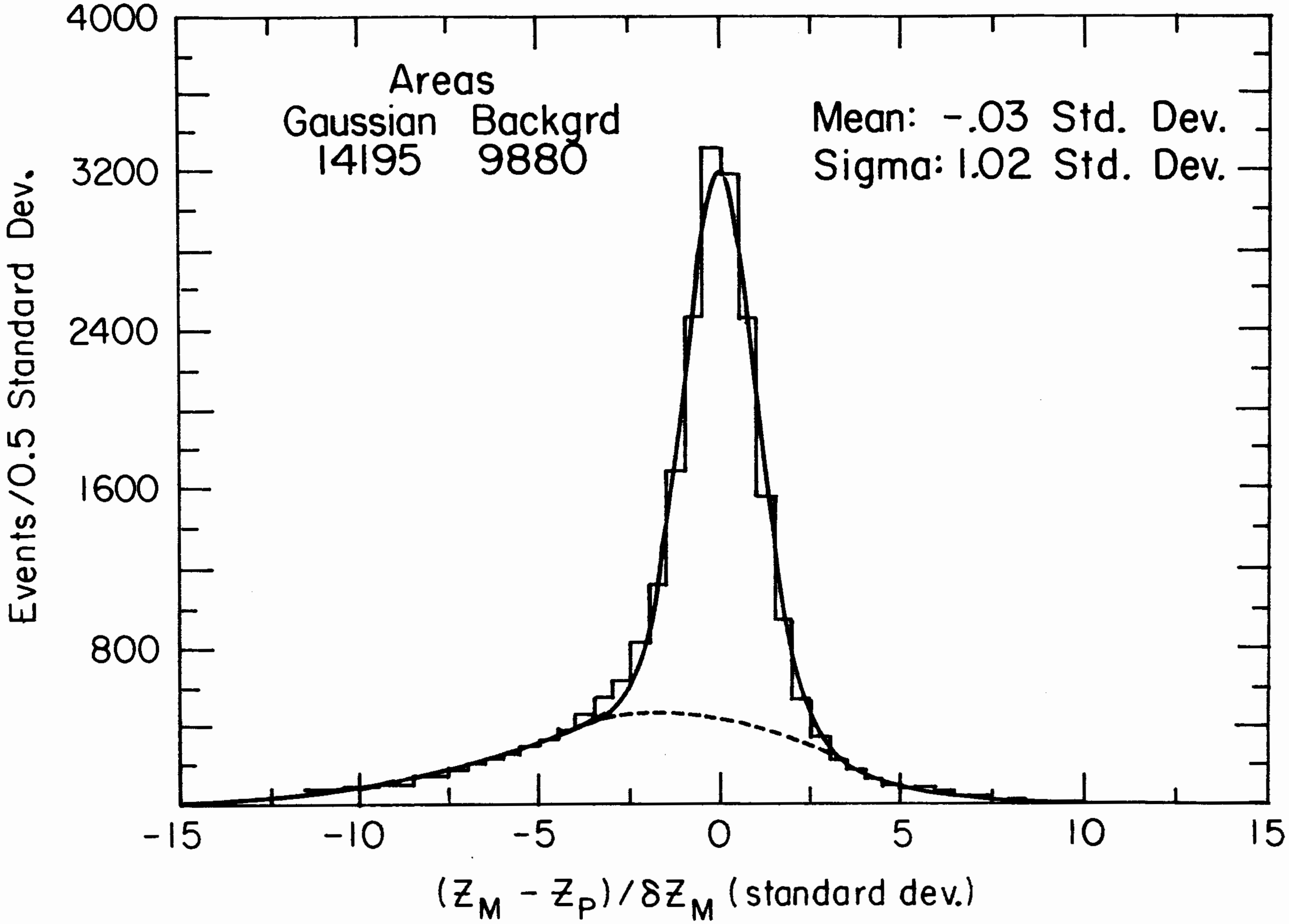
Areas
Gaussian Backgrd
14195 9880
Mean: -.03 Std. Dev.
Sigma: 1.02 Std. Dev.
Events/0.5 Standard Dev.
4000
3200
2400
1600
800
-15
-10
-5
0
5
10
15
$(Z_M - Z_P)/\delta Z_M$ (standard dev.)

the error depended upon how many sparks were associated with track.

At most one "low-momentum" track (stub) was allowed in a neutral pair, and more stringent cuts had to be applied. First of all, whereas no timing cuts were applied to the linked tracks, the stubs were required to be uniquely in-time if they had any timing information. In addition, the cut on the DCA of the tracks was decreased to 4 mm.

In the second step a simple cut was placed on the distance of the neutral vertex downstream of the recoil proton. The value of the cut was chosen to be 20 cm after studying the net K0 signal and signal-to-noise ratio as a function of the cut. The value of this cut was also different in the case that one of the tracks was a stub. It was 4.5 standard deviations (4.5 times the probable error in the Z position of the neutral vertex).

There was in addition a cut placed on the Z position of the neutral vertex after the MWPCs were reached. An absolute cut of -440 cm in Z was imposed after noting that no net K0 signal was seen beyond this point. (The z-position of the first MWPC downstream of the LH2 target was -500 cm.) This is not suprising given the fact that there would be at most two out of the four 1 m X 1 m MWPCs hit, which means that the tracks, if found at all, would be constrained to pass through the primary vertex (see section 4.1.3). A second more stringent cut was obtained by requiring that the neutral vertex be found less than one standard deviation downstream of the first MWPC plane which contained a hit for either track. If a hit was present, it meant that the real vertex was upstream of the plane. The tolerance simply allowed for the error in determining the position of the vertex.

Finally, each KO candidate surviving the preceeding cuts is used in a fit of the primary vertex. The neutral's track parameters and the relevant errors are calculated from the resultant momentum of the neutral and the position of the decay point. The neutral track is then used as any other track in the vertex fitting algorithm.

For each neutral pair considered, the following quantities result:

1. Coordinates (with errors), DCA, and χ^2_v of neutral vertex.
2. Contribution of neutral track to χ^2 of primary vertex.
3. Coordinates (with errors) and χ^2 of primary vertex.
4. Invariant mass (with error) of neutral.

The invariant mass spectrum for all $\pi^+\pi^-$ pairs passing the cuts on vertex separation, χ^2_v and DCA of the neutral vertex is shown in Figure 4-3. Figure 4-4 shows the distance of closest approach in mm for the KO signal plus background and the background (dashed). Table 4-1 gives the number of KO's reconstructed for the χ^2_v of the neutral vertex less than the value given. Also shown are the fraction of the total signal these numbers represent and the expected fraction for a perfect χ^2 distribution with one degree of freedom. How additional cuts on these quantities, and on other quantities derived from them, were used to reduce the background is shown next.

The two most obvious ways of reducing the background are 1) reducing the cut on the DCA of the tracks, and 2) increasing the cut on the separation between the primary and secondary vertices. These methods will always reduce the background, but inevitably reduce the signal as well. Therefore, I tried to formulate new quantities which would be more efficient at suppressing the background than the signal.

Figure 4-3. The $\pi^+\pi^-$ invariant mass spectrum for all pairs satisfying the cuts detailed in the text.

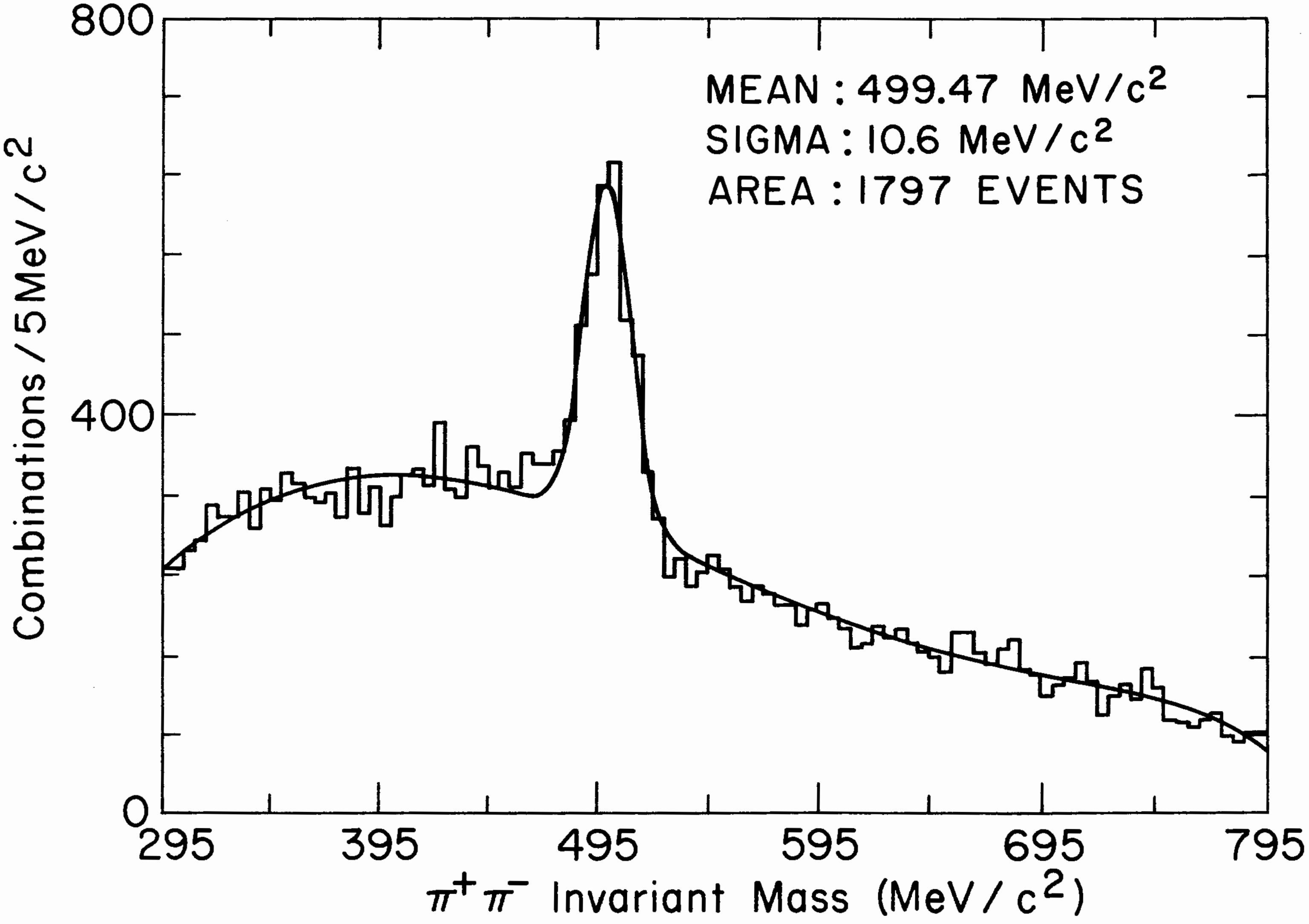
MEAN : 499.47 MeV/c^2
SIGMA : 10.6 MeV/c^2
AREA : 1797 EVENTS
Combinations / 5MeV/c^2
800
400
0
295
395
495
595
695
795
$\pi^+\pi^-$ Invariant Mass (MeV/c^2)

Figure 4-4. Distribution of the distance of closest approach (DCA) for the KO candidates in the indicated mass ranges. The solid histogram contains the KOs plus the background in the KO mass region. The background was calculated by weighting events from the indicated regions by 0.5.

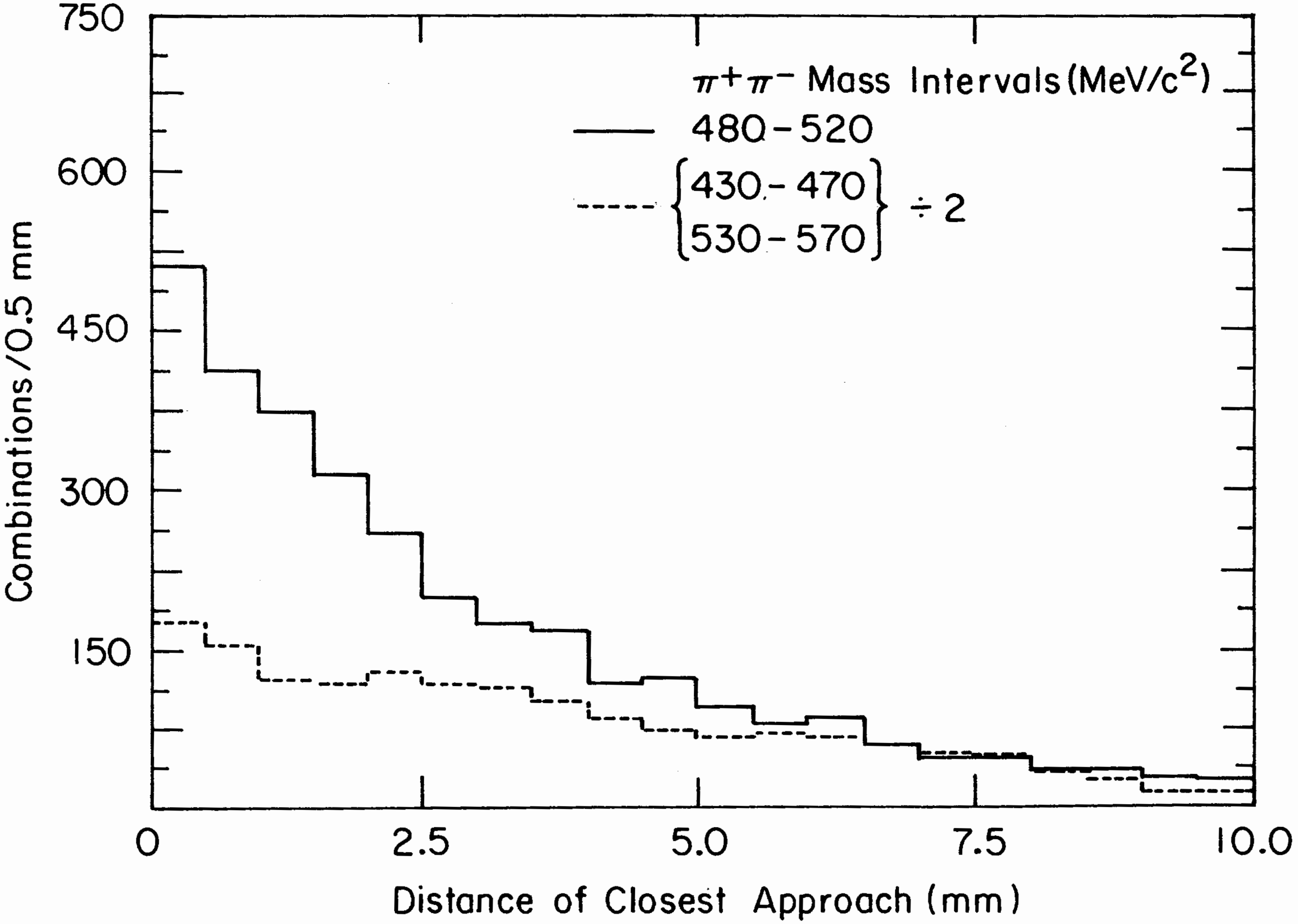
$\pi^+\pi^-$ Mass Intervals (MeV/c^2)
480-520
{430-470, 530-570} ÷ 2
750
600
450
300
150
Combinations/0.5 mm
0
2.5
5.0
7.5
10.0
Distance of Closest Approach (mm)

TABLE 4-1

NUMBER OF RECONSTRUCTED KOs AS FUNCTION OF χ^2_v

χ^2_v	NUMBER OF KO's	FRACTION OF TOTAL	EXPECTED FRACTION
0.2	726 +- 42	0.40 +- 0.03	0.345
0.5	1043 +- 50	0.58 +- 0.04	0.520
1.0	1272 +- 57	0.71 +- 0.05	0.683
2.5	1511 +- 66	0.84 +- 0.05	0.886
4.0	1655 +- 73	0.92 +- 0.06	0.954
6.0	1726 +- 77	0.96 +- 0.06	0.985
9.0	1785 +- 81	0.99 +- 0.06	0.997

One such quantity was the quality factor - Q for short. It was simply defined as the sum of the chi-square of the neutral vertex and the contribution of the neutral track to the chi-square of the primary vertex:

$$Q = \chi_v^2 + \chi_n^2$$

The smaller the value of Q the more likely that a KO candidate was genuine. The distribution of Q for the $\pi^+\pi^-$ mass region of 480 to 520 Mev/c^2 is shown in Figure 4-5. Also shown (dashed) is the distribution of Q for the background region. The effect of a cut on Q is shown in Figures 4-6 and 4-7. The mass combinations with Q less than 4.0 are shown in Figure 4-6, while those with Q greater than 4.0 are shown in Figure 4-7.

Since the tracks made by the pions from a KO often miss the primary vertex, they may also pass near tracks coming from the primary vertex at some point downstream (or upstream) of the primary vertex. When a track from a KO has a DCA with another track (not from the KO) which is less than 1 cm, and the Z position of that DCA is greater than 20 cm downstream of the proton, this alternate pairing also becomes a candidate for a KO if it is neutral. This occurs much more often than one might think, and there are sometimes several KO candidates sharing one or both of the tracks from a genuine KO. The problem is thus to choose the correct pair and exclude the rest, since there can be at most one real KO among those candidates sharing a track.

The problem was solved in most cases by choosing that pair which had the greatest significance in terms its distance downstream of the refitted primary vertex. The quantity which measured the significance was defined as:

$$\sigma_z = (Z_v - Z_p)/\sqrt{\delta z_v^2 + \delta z_p^2}$$

Figure 4-5. The distribution of the quality factor (Q) for the indicated $\pi^+\pi^-$ invariant mass intervals. Solid histogram includes KOs and background.

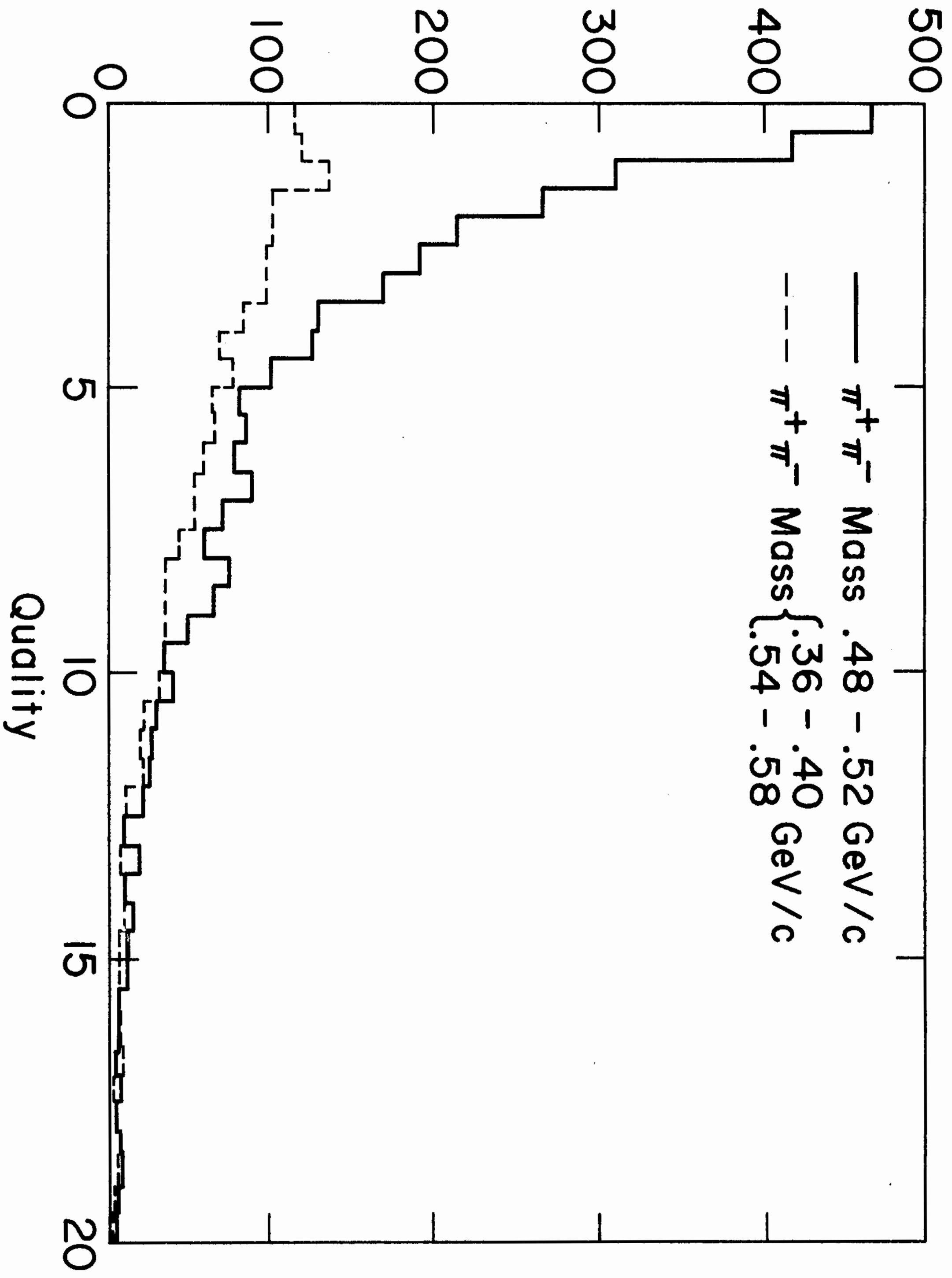

$\pi^+\pi^-$ Mass .48 - .52 GeV/c
$\pi^+\pi^-$ Mass {.36 - .40, .54 - .58} GeV/c
0
100
200
300
400
500
0
5
10
15
20
Quality

Figure 4-6. $\pi^+\pi^-$ invariant mass for Q less than 4.0.

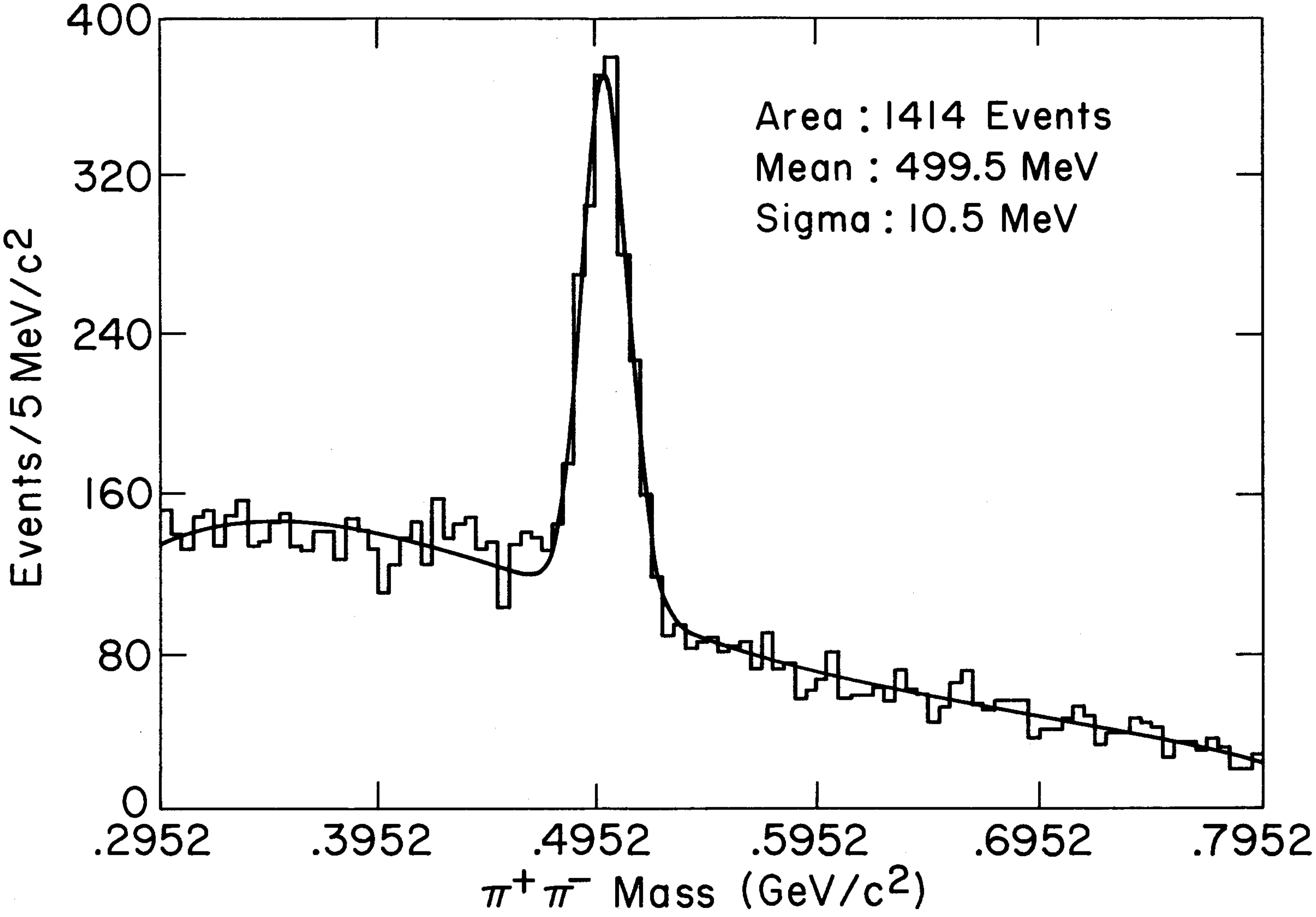
Area : 1414 Events
Mean : 499.5 MeV
Sigma : 10.5 MeV
Events/5 MeV/c^2
400
320
240
160
80
0
.2952
.3952
.4952
.5952
.6952
.7952
$\pi^+\pi^-$ Mass (GeV/c^2)

Figure 4-7. $\pi^+\pi^-$ invariant mass for Q greater than 4.0.

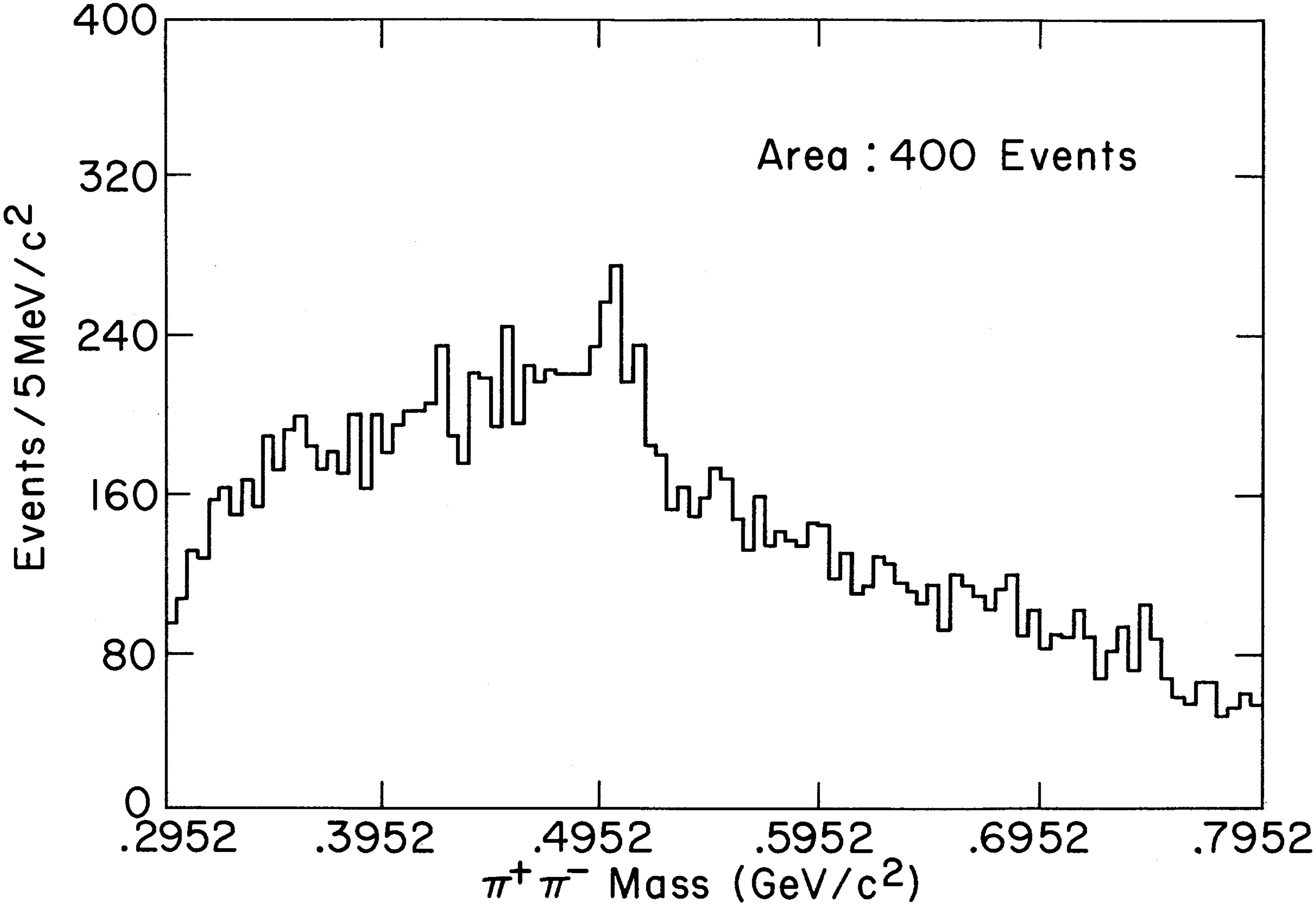
Area : 400 Events
Events / 5 MeV/c^2
400
320
240
160
80
0
.2952
.3952
.4952
.5952
.6952
.7952
$\pi^+\pi^-$ Mass (GeV/c^2)

This quantity measures the distance downstream in units of the total error in the measurement of the distance. The distribution of σ_z is shown in Figure 4-8 for the KO signal and background regions. I then found that an even better indicator for choosing the best candidate was obtained by dividing σ_z by Q^2. The results of using σ_z/Q^2 to choose the best KO candidate are shown in Figure 4-9. The solid histogram shows the candidates which were chosen as the best (this also includes those in which there was no ambiguity) as opposed to the dashed histogram which were those rejected.

Most of the background in the mass spectra shown thus far occurs in the first 60 cm downstream (see Figure 4-10) of the end of the LH2 target. For this reason, I devised a cut which would suppress the background drastically in this region (at the expense of some signal), while at the same time removing little of the signal in the region where the background was already small. The Z position of the KO decay was usually measured relative to the beginning (i.e., upstream end) of the LH2 target. This variable was called ZZ. The quantity developed to accomplish the background reduction discussed above was a function of Q and ZZ defined by:

$$QR = Q/(ZZ \times 0.025 + 0.5) \quad \text{for } ZZ < 100 \text{ cm.}$$
$$= Q/(ZZ \times 0.075 - 4.5) \quad \text{for } 100 < ZZ < 300 \text{ cm.}$$

Figures 4-11 and 4-12 show the performance of QR. Figure 4-11 shows the fraction of the total KO signal which has a value of QR less than the value of the cut on the abscissa. Note the dependence on the KO momentum which results from fact that lower momentum KO´s decay closer to the primary vertex on the average. Figure 4-12 shows the signal to background ratio as a function of the cut on QR for the same ranges of KO momenta. The mass spectra for pairs with QR < 1 and QR > 1 are shown in Figure 4-13 (a)

Figure 4-8. Distribution of σ_z for the KO signal (solid histogram) and background (dashed) mass regions.

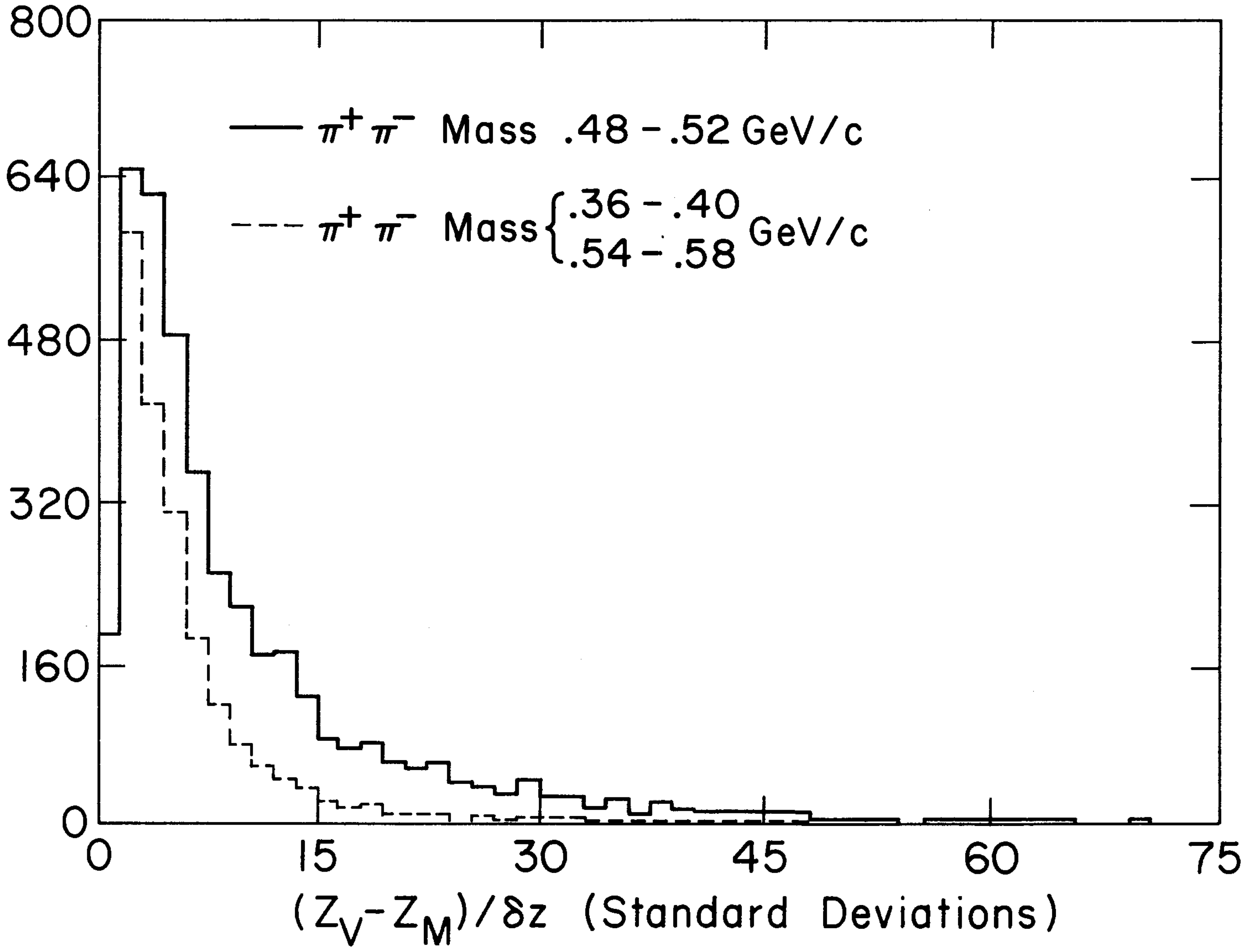
800
640
480
320
160
0
0
15
30
45
60
75
$\pi^+\pi^-$ Mass .48 – .52 GeV/c
$\pi^+\pi^-$ Mass {.36 – .40, .54 – .58} GeV/c
$(Z_V - Z_M)/\delta z$ (Standard Deviations)

Figure 4-9. Performance of the quantity σ_z/Q^2 at choosing the best KO candidate if several share the same track(s). Solid histogram shows KO candidates chosen as best plus those with no tracks shared. Dashed histogram shows candidates which had shared tracks and were not chosen as best.

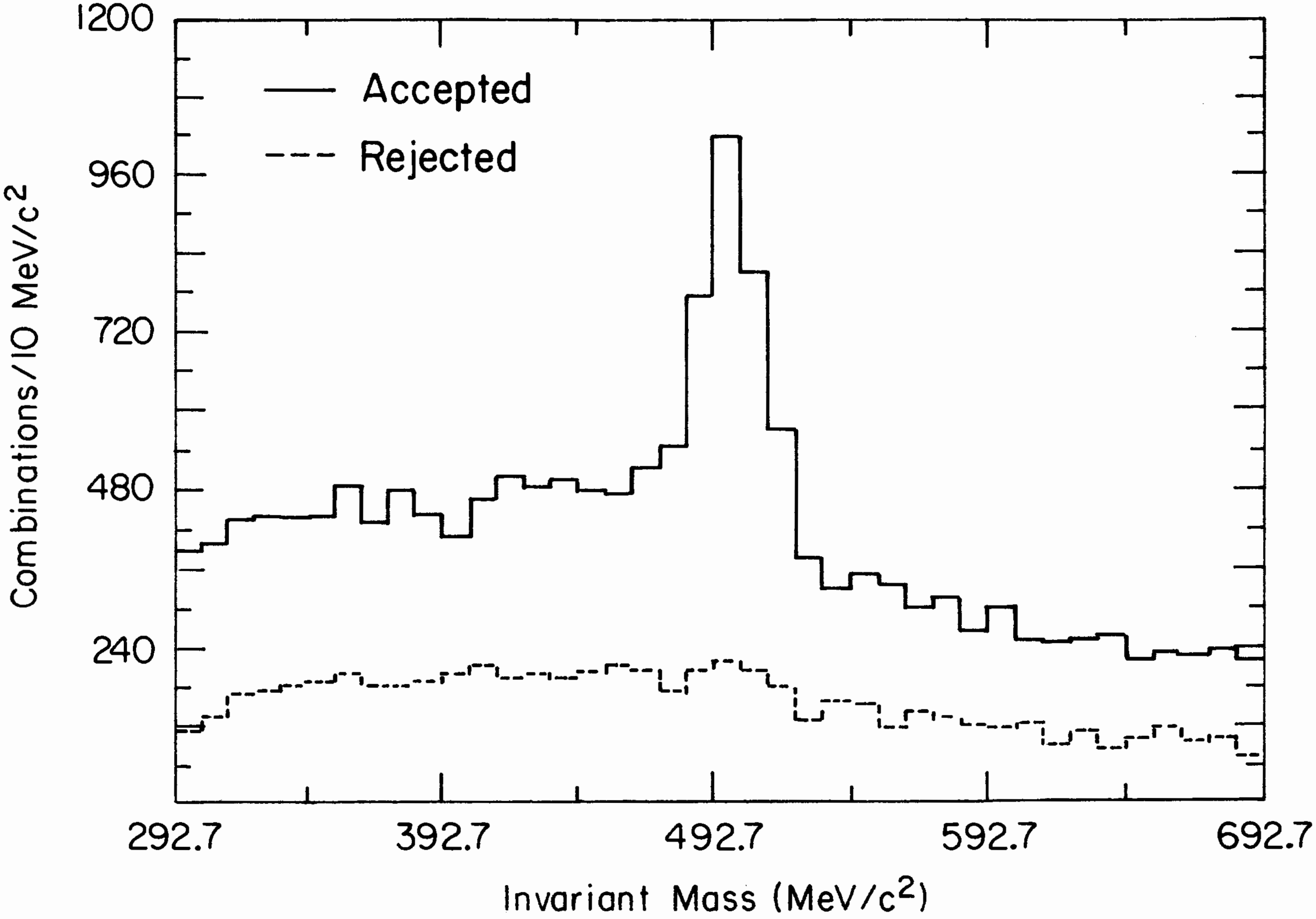
Accepted
Rejected
1200
960
720
480
240
Combinations/10 MeV/c²
292.7
392.7
492.7
592.7
692.7
Invariant Mass (MeV/c²)

Figure 4-10. The distribution of the Z position of the K0 candidate vertices for K0s plus background, while dashed includes mostly background.

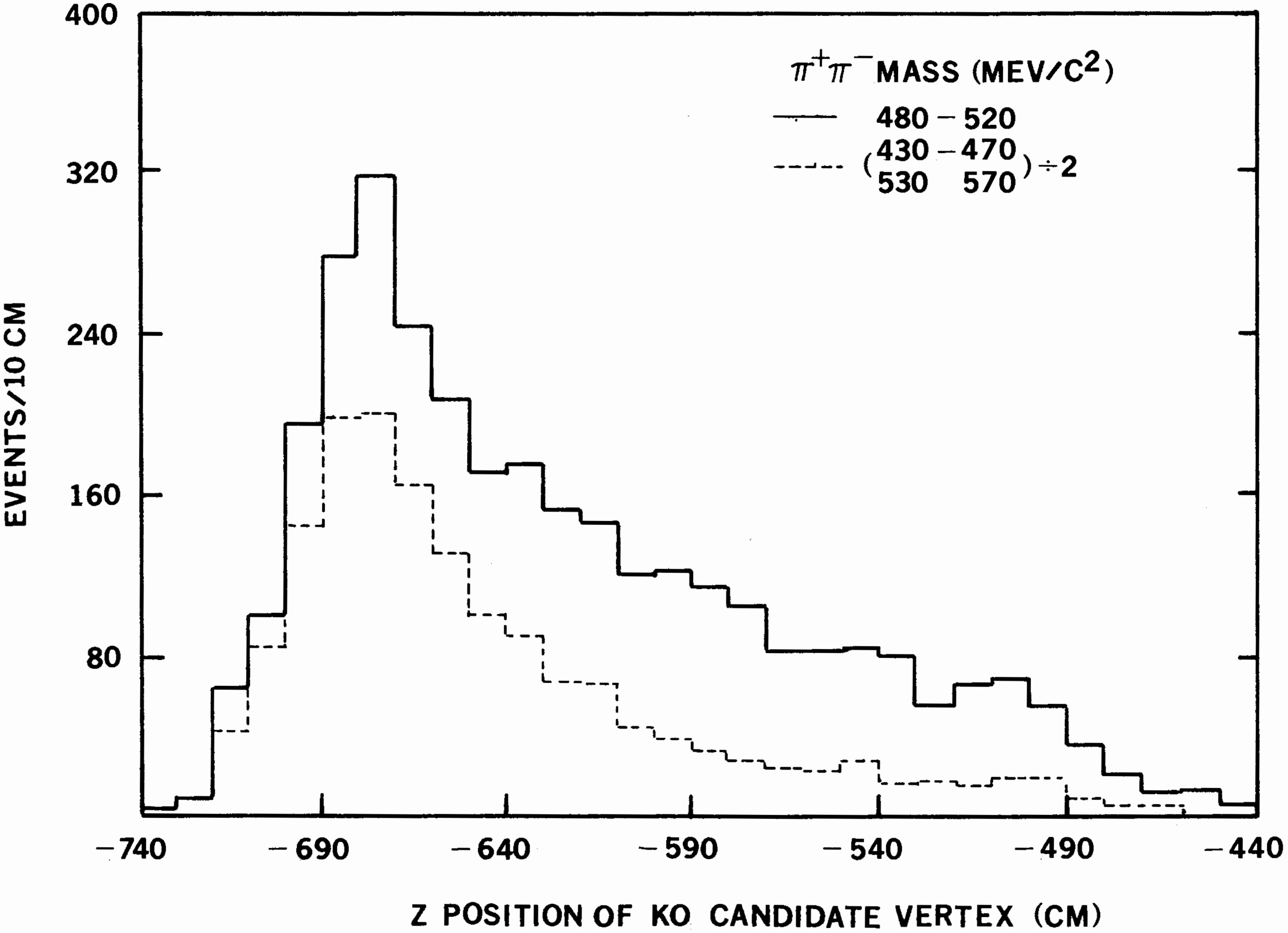

400
320
240
160
80
EVENTS/10 CM
$\pi^+\pi^-$ MASS (MEV/C^2)
480 – 520
($^{430}_{530}$ – $^{470}_{570}$) ÷ 2
–740
– 690
– 640
– 590
– 540
– 490
– 440
Z POSITION OF KO CANDIDATE VERTEX (CM)

Figure 4-11. Fraction of total signal as a function of the cut on the quantity QR, and of the momentum of the KO candidate.

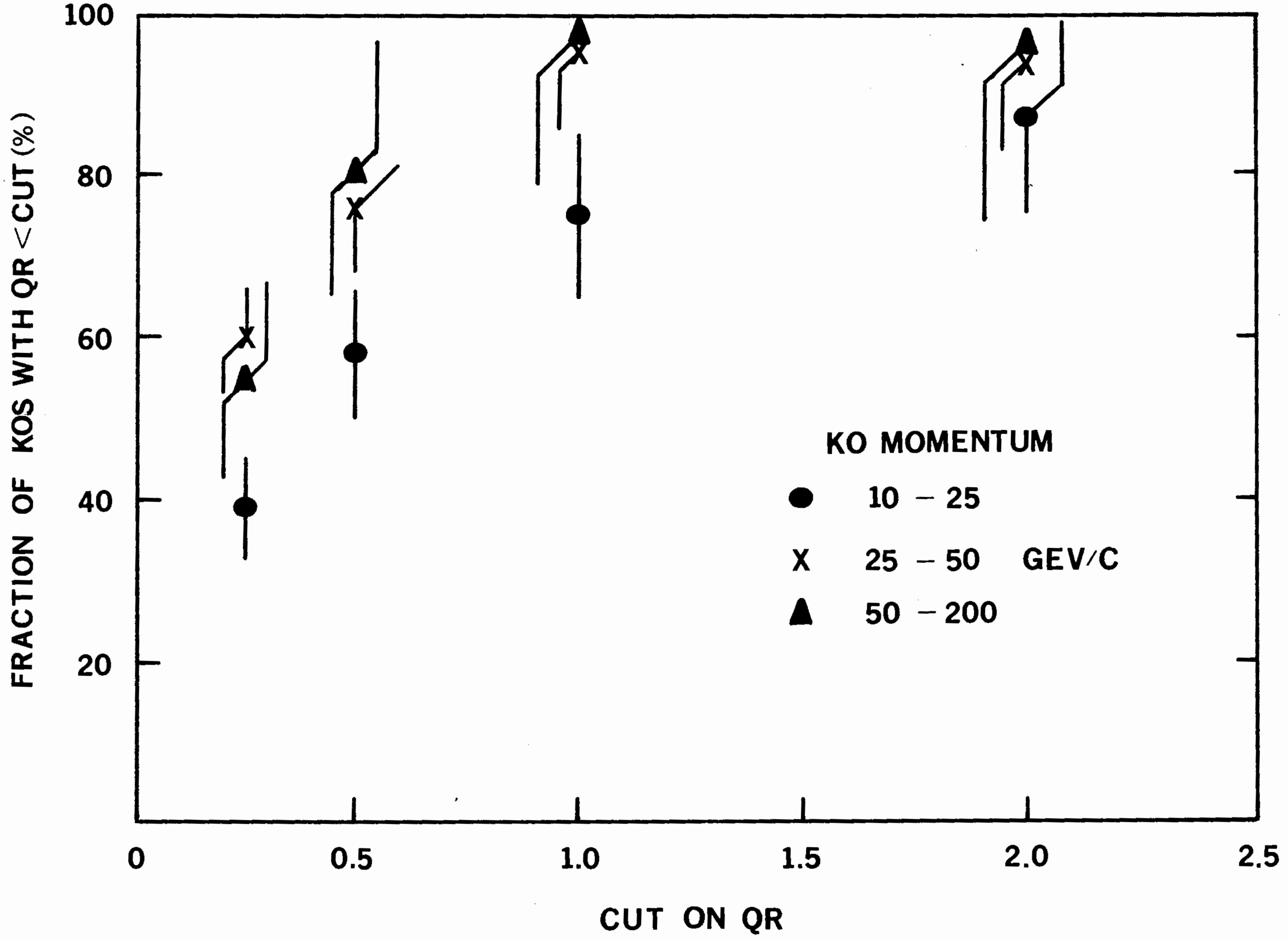
FRACTION OF KOS WITH QR < CUT (%)
100
80
60
40
20
0
0.5
1.0
1.5
2.0
2.5
CUT ON QR
KO MOMENTUM
● 10 – 25
X 25 – 50 GEV/C
▲ 50 – 200

Figure 4-12. Signal to background ratio as a function of the cut on the quantity QR for the indicated K0 candidate momentum ranges. Signal region was 480 to 520 Mev/c^1.

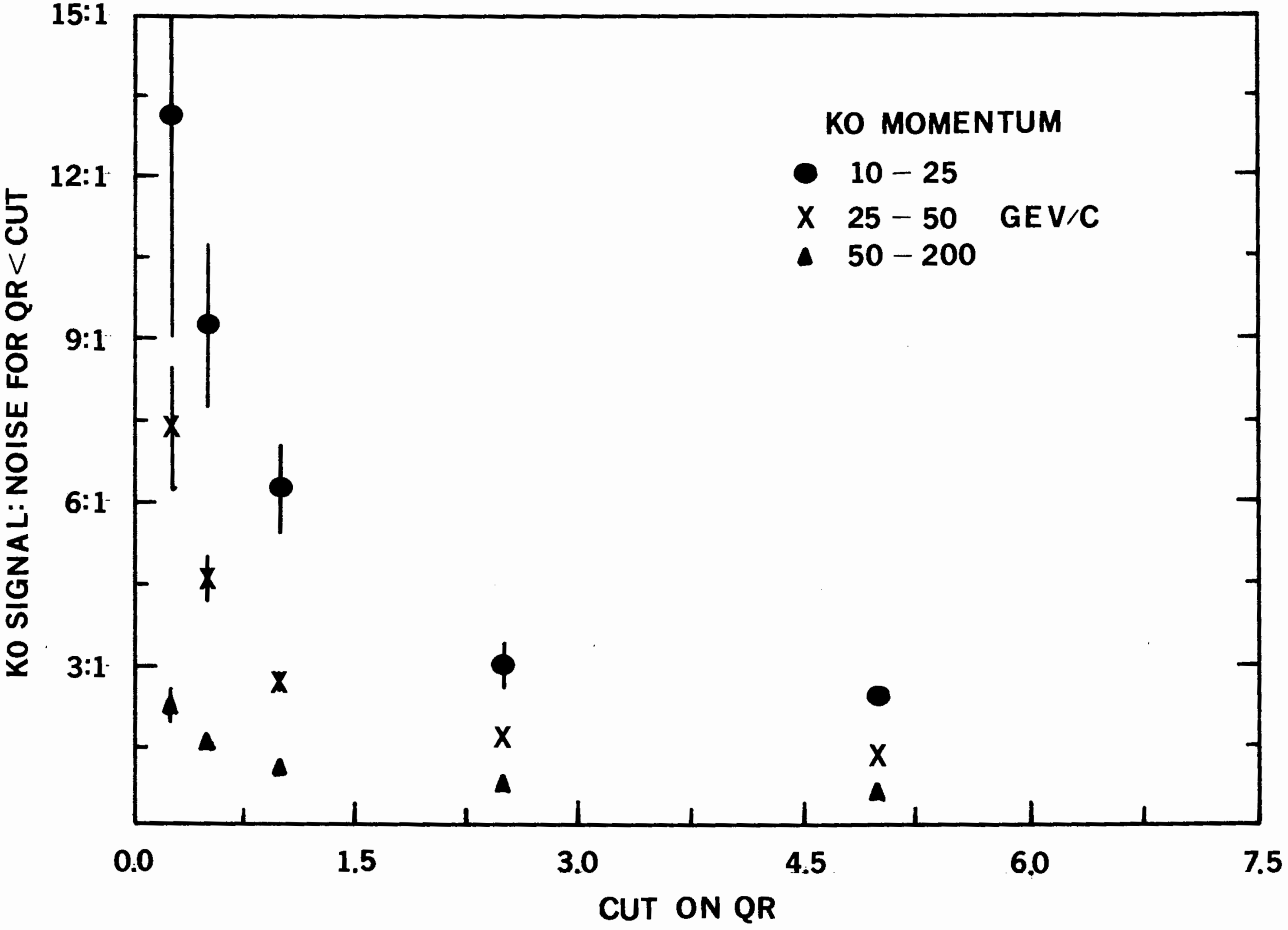
15:1
12:1
9:1
6:1
3:1
KO SIGNAL: NOISE FOR QR < CUT
0.0
1.5
3.0
4.5
6.0
7.5
CUT ON QR
KO MOMENTUM
● 10 – 25
X 25 – 50 GEV/C
▲ 50 – 200

Figure 4-13. Mass spectrum for $\pi^+\pi^-$pairs with QR < 1. (a) and (b) for pairs with QR > 1.

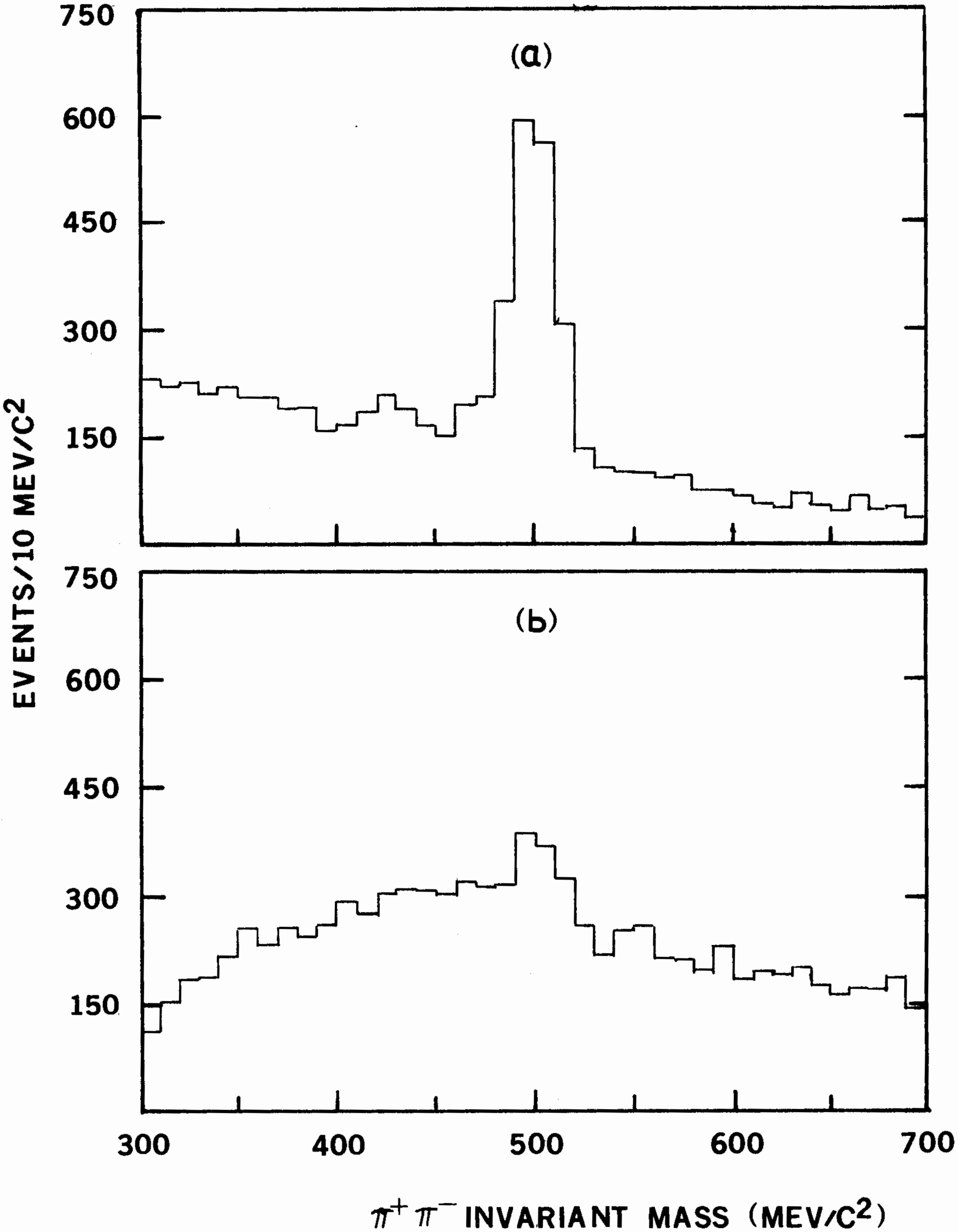
750
600
450
300
150
(a)
750
600
450
300
150
(b)
EVENTS/10 MEV/C2
300
400
500
600
700
π+ π− INVARIANT MASS (MEV/C2)

and (b) respectively. The background subtracted momentum distribution for the reconstructed KO's is shown in Figure 4-14. Figure 4-15 shows the KO lifetime distribution as a check that the reconstruction efficiency has no holes. The region over which the lifetime can be expected to be relatively insensitive to the limited decay space is indicated by the dashed line. The fit gives a slope corresponding to a lifetime of 88.5 picoseconds, compared to the published value of 88.6 picoseconds. A much larger deviation could be expected.

Finally, I show the KO acceptance as determined by a Monte Carlo program. The details of the Monte Carlo are described in Chapter 6. The KO detection efficiency as a function of the KO momentum is shown in Figure 4-16. The two plots were derived from two different generated KO momentum distributions, but the dependences on the KO momentum are statistically identical. Figure 4-17 shows the KO detection efficiency as a function of the distance of its decay point downstream of the primary vertex. The reason for the different detection efficiencies in Figures 4-16 and 4-17 is that each represents the efficiency integrated over the other variable.

Now that I have described the process by which the KO's were obtained, I can proceed to discuss the final analysis in which I studied the properties of both the $K0\pi^{\pm}$ and $K0\pi^{+}\pi^{-}$ final states.

Figure 4-14. Background subtracted KO momentum distribution. KO signal region was 460 to 540 Mev/c^2 to allow for worsening resolution at higher momentum.

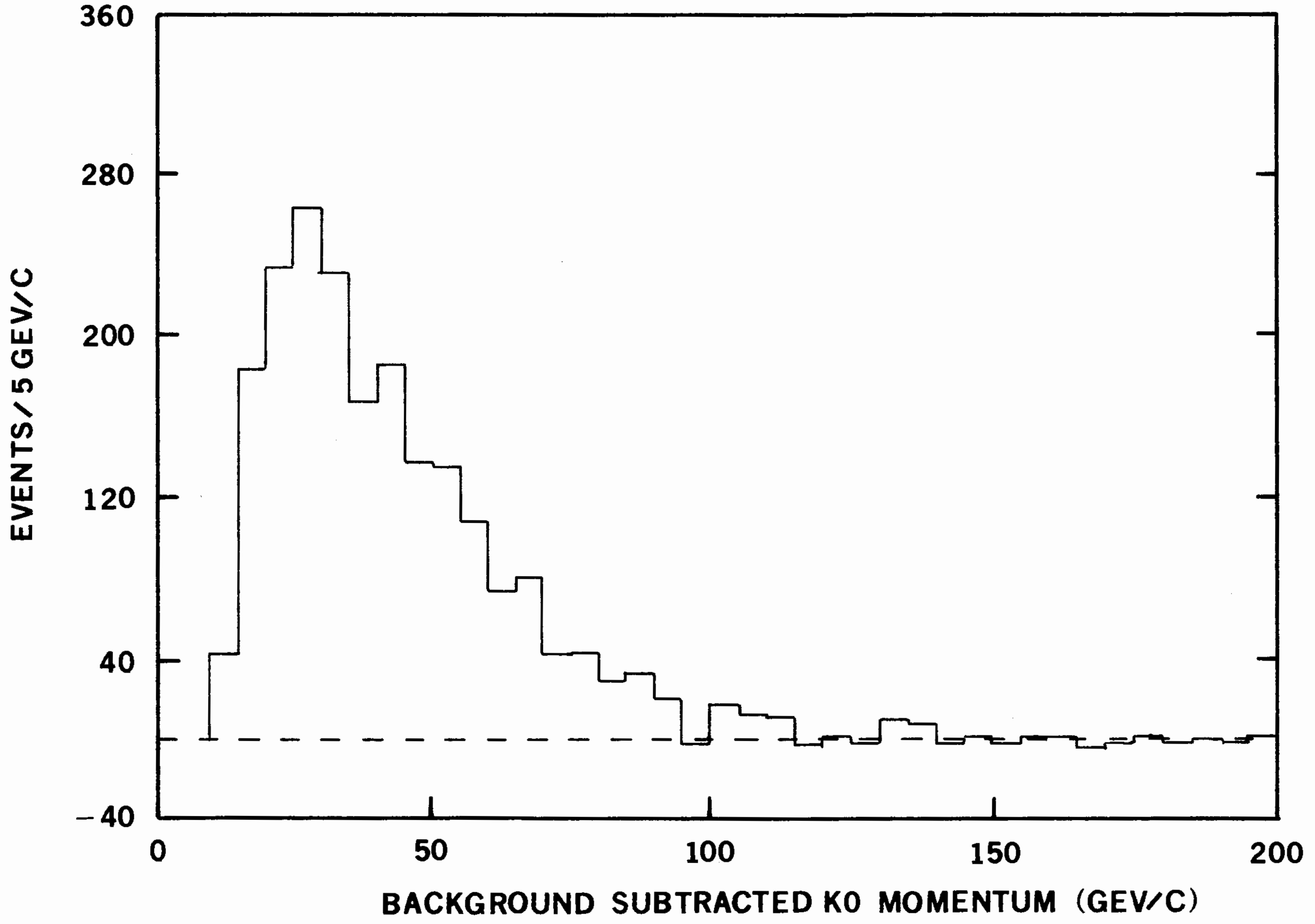
360
280
200
120
40
-40
EVENTS/ 5 GEV/C
0
50
100
150
200
BACKGROUND SUBTRACTED K0 MOMENTUM (GEV/C)

Figure 4-15. Background subtracted K0 proper lifetime distribution. The decay point was restricted to lie in the range -640 to -500 cm. The fit indicated gives a lifetime of 88.5 picoseconds, compared to the published value of 88.6.

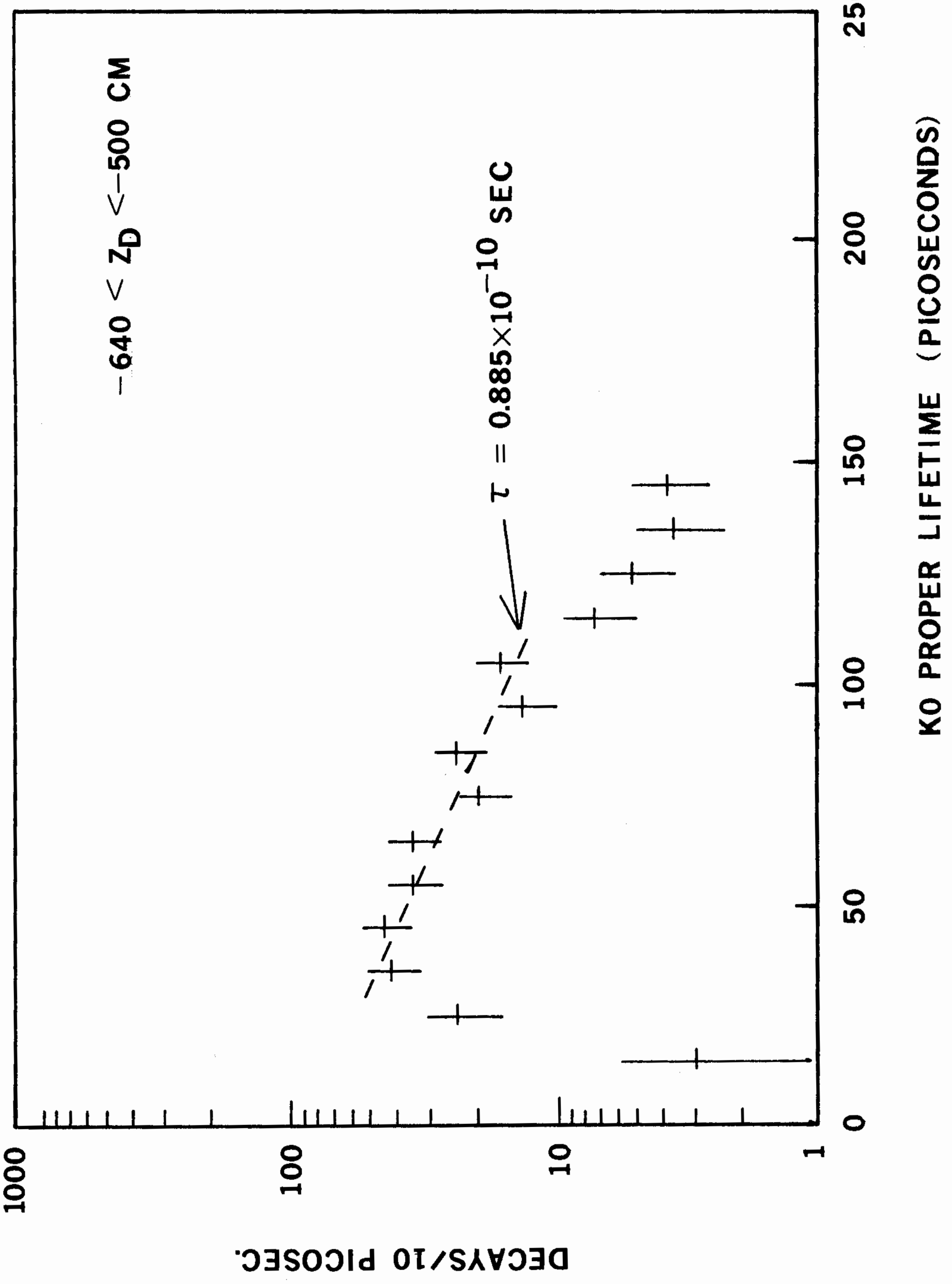
−640 < Z_D <−500 CM
τ = 0.885×10^−10 SEC
1000
100
10
1
DECAYS/10 PICOSEC.
0
50
100
150
200
250
K0 PROPER LIFETIME (PICOSECONDS)

Figure 4-16. KO detection efficiency as a function of the KO's momentum. The efficiency was determined by the Monte Carlo program discussed in Chapter 6.

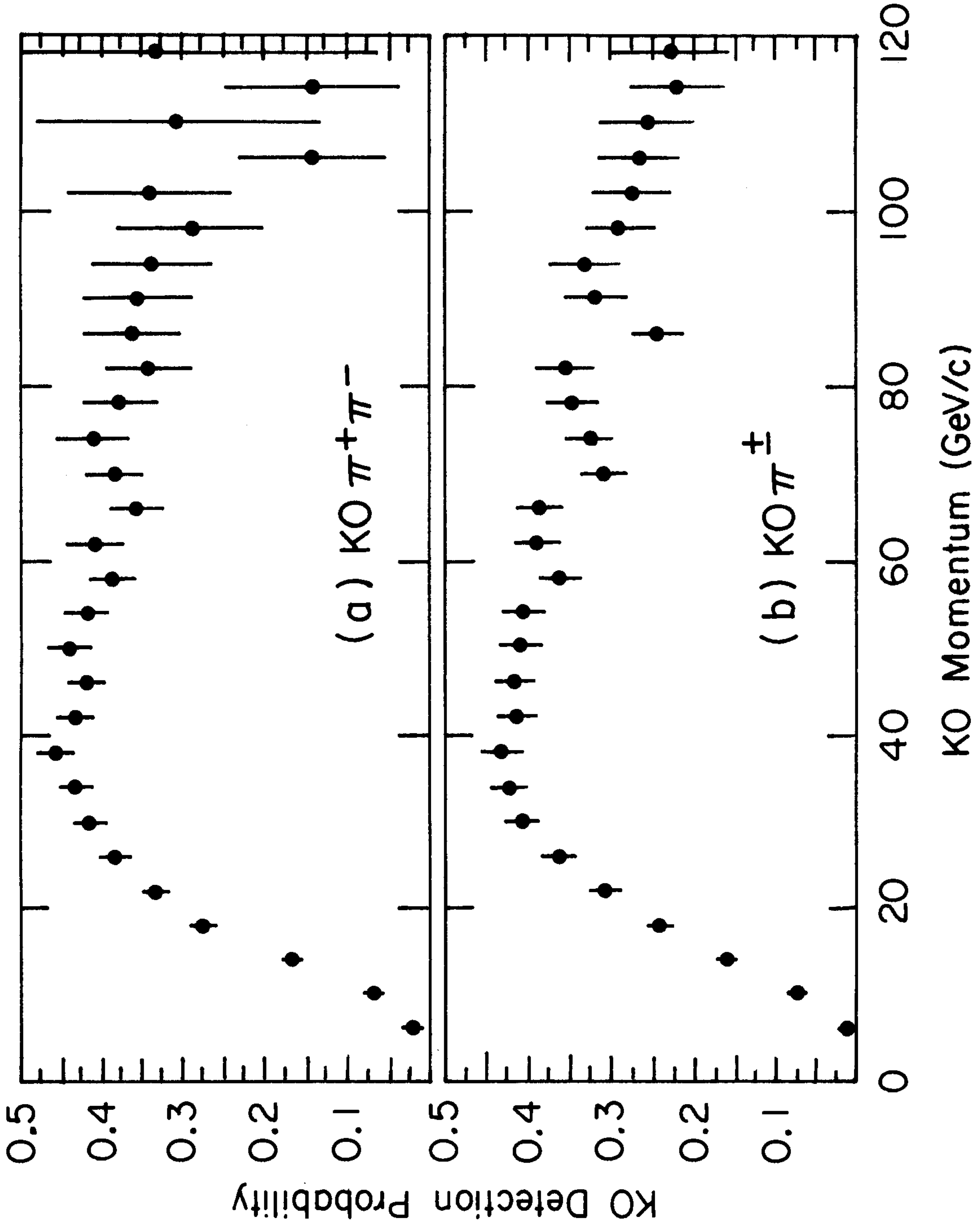

KO Detection Probability
0.5
0.4
0.3
0.2
0.1
(a) KO $\pi^+\pi^-$
(b) KO $\pi^\pm$
0
20
40
60
80
100
120
KO Momentum (GeV/c)

Figure 4-17. K0 detection efficiency as a function of the K0 decay point downstream of the primary vertex. This efficiency was also Monte Carlo determined.

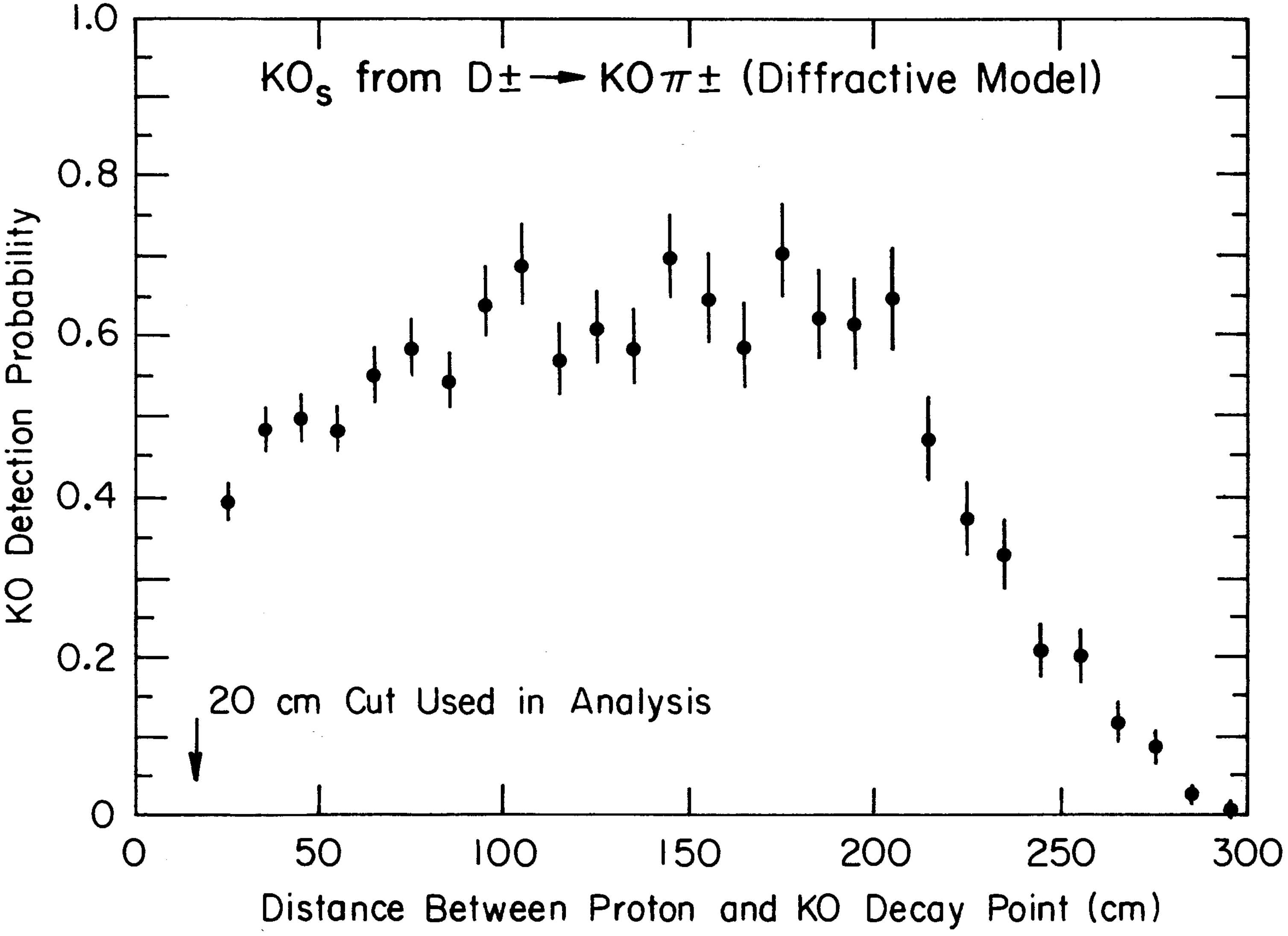
KO_s from D± → KOπ± (Diffractive Model)
KO Detection Probability
Distance Between Proton and KO Decay Point (cm)
20 cm Cut Used in Analysis
1.0
0.8
0.6
0.4
0.2
0
0
50
100
150
200
250
300

CHAPTER 5

FINAL DATA ANALYSIS

This chapter discribes the final stage of the data analysis and the results obtained. This phase of the analysis was primarily concerned with the search for evidence for the production of the D(1865) charmed meson and its subsequent decay into $KO\pi^{\pm}(D^{\pm})$ or $KO\pi^{+}\pi^{-}(D^{\circ}, \bar{D}^{\circ})$.

There is always a danger of extracting what one might call a "signal" (i. e., an excess of events with a sufficiently small probability of being a statistical fluctuation of the background), when one knows beforehand that a particle with a given mass exists. It is therefore necessary to fully explain and justify any cuts which must be applied to the data in order to see a "signal".

To this end, I will first describe the various cuts which I used, and then justify the particular value of each cut. The cuts fall into two separate categories:

1. Event cuts
2. Track related cuts

5.1 Discussion of Cuts

The event type cuts include cuts on the following quantities:

1. Proton momentum
2. Mass recoiling against proton
3. Deviation of fitted vertex from extrapolated recoil track
4. KO parameters

Cuts in the second category involve:

1. Track timing
2. Track type
3. Chi-square of track

The event cuts remove entire events from the data sample, while the track cuts remove only certain tracks, and thus limit the number of mass combinations.

Following is a description of each of the cuts listed. After describing what the cut does, I will attempt to justify the particular value that I used.

5.1.1 Event Cuts

5.1.1.1 Proton Momentum

The rough time of flight (TOF) cuts imposed by the trigger electronics were just that - rough. After the calibration of the recoil TOF, some recoil particles were substantially outside of the desired range of 12 - 32 nanoseconds for the 2 m flight path.

An analysis of FNAL bubble chamber experiment 154 data done by Professor R. D. Sard showed that at least 90% of the particles having:

1. Laboratory angle greater than 55 degrees from incident beam
2. Velocity corresponding to 11 to 30 ns TOF in our apparatus

were protons. The identification of the particles was based upon the amount of ionization produced by the particle (possible only for momenta below 1.4 Gev/c). The largest part of the contamination arises from pions with times of flight near the lower limit.

It was possible to distinquish proton from pions by the pulse height measured in the front recoil counters up to $\beta = 0.4$. At this value of β, the energy losses of pions and protons for the 1" thick scintillation counters become roughly equal. The 0.5" aluminum absorber and back recoil counters were designed to increase the discrimination region up to $\beta = 0.6$ (see section 3.2). However, the back counters did not work reliably. Thus I compromised and decided on a cut of $\beta < 0.50$, corresponding to a proton momentum of 0.53 Gev/c or less. The minimum TOF was 13.3 ns for the 2 m flight path.

5.1.1.2 Missing Mass

The mass, M_X, of the system recoiling against the recoil proton was defined in Chapter 1. The trigger electronics were designed to select events with M_X in the range of 3.5 to 7.0 Gev/c^2, but the actual acceptance extended somewhat above and below these limits. There is also the possibility that M_X could be non-physical in the case that the recoil particle was really a pion. That is, assigning the proton mass to the recoil particle is not consistent with the direction and velocity of the particle. Such events must be rejected.

The value of M_X should be greater than approximately 3.8 Gev/c^2 for the pair production of D(1865) mesons. However, the error on the determination of M_X is rather large and there is a systematic uncertainty in the TOF calibration, so any cuts which are used must be fairly liberal. I usually required that M_X be greater than 3.4 Gev/c^2.

5.1.1.3 Deviation of vertex from recoil track

I had briefly mentioned this distribution in section 4.3.3 during the discussion of error scaling. For each KO candidate, a refit of the primary vertex was done including the neutral track. Clearly, for the background events this does not have any special significance. For the real KO events however, this procedure gives the best estimate that is possible for the location of the primary vertex, since two non-vertex associated tracks have been eliminated, while one additional vertex associated track (the neutral's track) has been added.

The distribution of interest was obtained by computing the difference in Z between the fitted vertex and the recoil track extrapolated to the beam line and dividing by the expected error in the Z position of the vertex. This error was obtained from the covariance matrix of the least squares fit of the vertex. Figure 4-2 is reproduced here as Figure 5-1 for convenience. Note the Gaussian-like "peak" and the skewed "background". The indicated fit was done with a polynomial plus a Gaussian. The relative areas of the Gaussian and polynomial seem to indicate that up to 40% of the recoil tracks originated from secondary interactions rather than primary interactions. I should note that most of the events in the "background" (at least those less than 0 on the abscissa) correspond to the fitted vertex having been found upstream of the proton. I should also note that the distribution in Figure 5-1 was not obtained from the events with KO candidates but represents a sample of the data in which there were at least 4 linked tracks per event and at least 3 linked tracks were included in the vertex fit at the 5% confidence level. No stubs were used in the vertex fits.

Figure 5-1. Distribution of fitted vertex about the Z value obtained by extrapolation of the recoil track to the beam line. Negative deviations correspond to the vertex found upstream of the proton tracks. Z_ρ = proton Z; Z_M = main vertex Z.

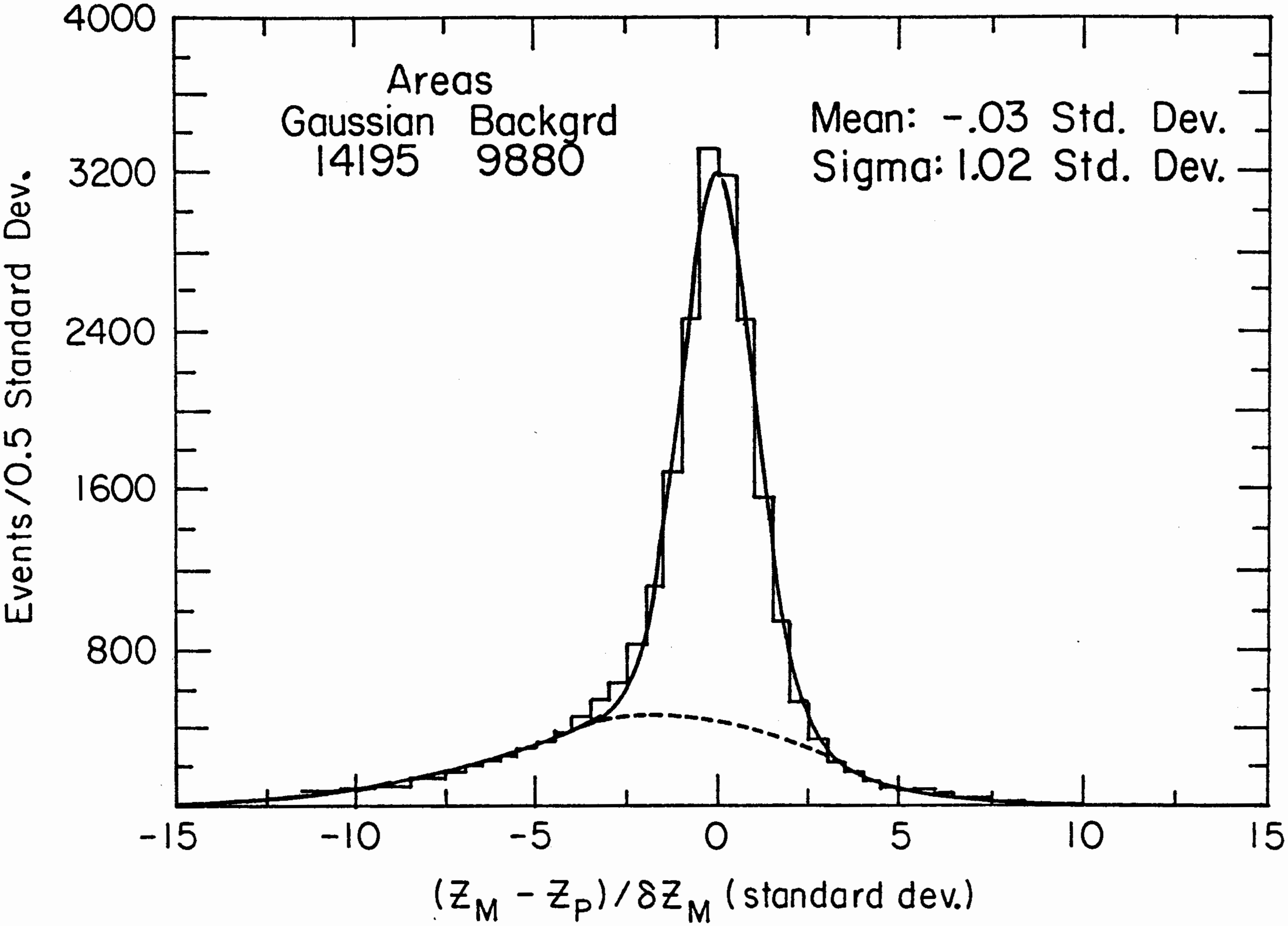
Areas
Gaussian Backgrd
14195 9880
Mean: -.03 Std. Dev.
Sigma: 1.02 Std. Dev.
Events/0.5 Standard Dev.
4000
3200
2400
1600
800
-15
-10
-5
0
5
10
15
$(Z_M - Z_P)/\delta Z_M$ (standard dev.)

To demonstrate that the events in the "peak" are really topologically different from those in the "background", I have prepared Figure 5-2. The number of tracks per event is shown for events in which the vertex is consistent with the recoil track to better than two standard deviations in (a), and in (b) for events where the difference is three or more standard deviations. The number of tracks includes the recoil and beam tracks. There is a clear tendency toward higher multiplicity in (b), which is probably the result of two processes:

1. The non-diffractive nature of the primary interaction
2. The extra particles from the secondary interaction

Based on these observations, I required the fitted vertex to be within two standard deviations of the recoil track. I believe that this cut is necessary to reduce the probability that the event had a secondary interaction and to enhance the probability that the event was diffractive in nature.

5.1.1.4 KO Parameters

The quantities which were used to increase the purity of the KO´s sample were discussed in section 4.3.

5.1.2 Track Cuts

As mentioned above, these cuts remove certain tracks from consideration in forming mass combinations. When looking for a signal in a multi-body final state, one must carefully eliminate the tracks which are "bad" to avoid an excessive combinatorial background. Thus I studied the characteristics of the various types of the tracks carefully, including their contributions to several known particles.

Figure 5-2. The number of tracks per event, including the beam and recoil proton tracks, for (a) the events with the fitted vertex within 2 standard deviations of the recoil track, and (b) the events with the vertex more than 3 standard deviations from the recoil track.

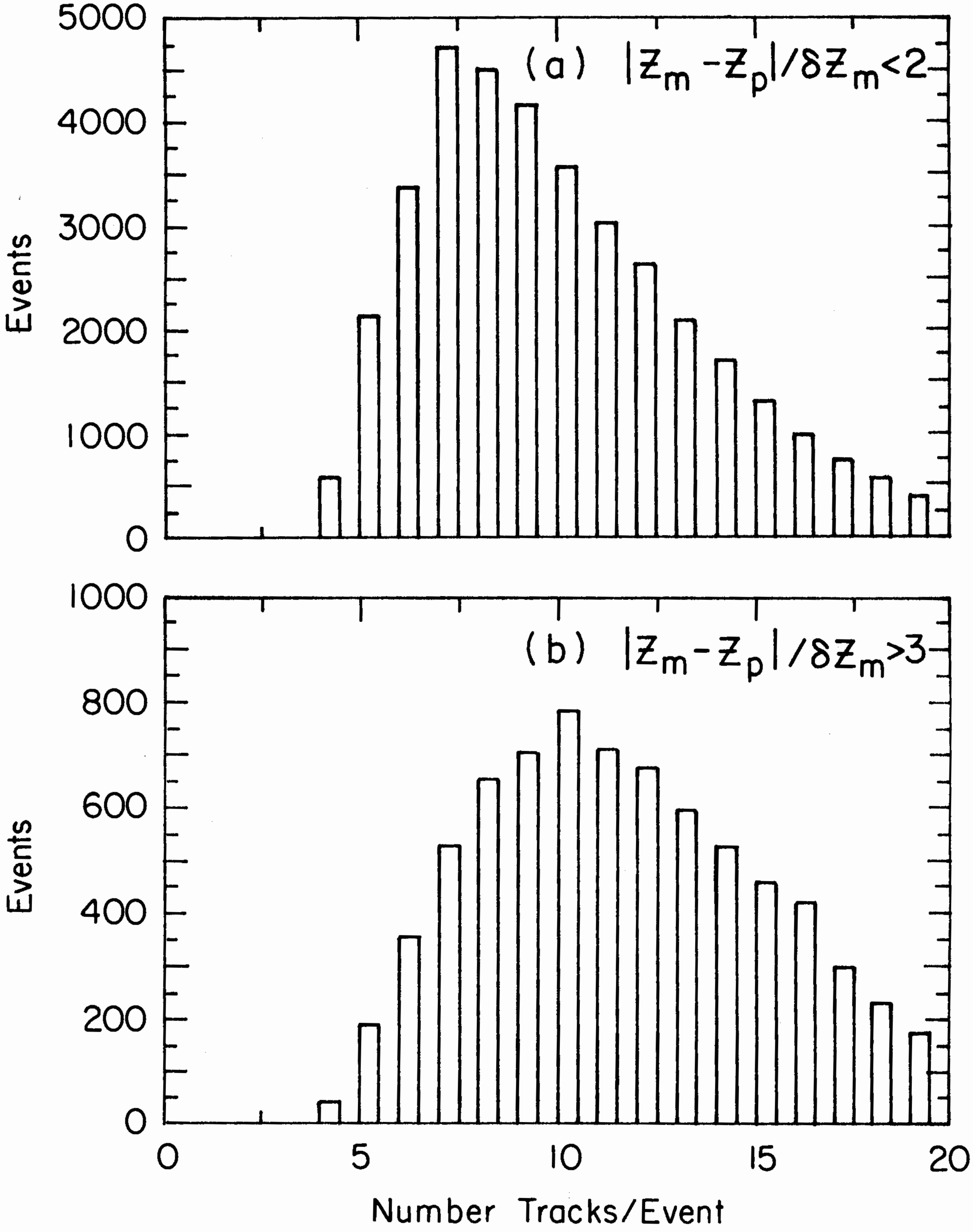
(a) $|Z_m - Z_p|/\delta Z_m < 2$
(b) $|Z_m - Z_p|/\delta Z_m > 3$
Events
Events
5000
4000
3000
2000
1000
0
1000
800
600
400
200
0
0
5
10
15
20
Number Tracks/Event

5.1.2.1 Track Timing

I first studied the timing properties of the three types of tracks. To perform this study, I encoded the results of my retiming algorithm (see section 4.3.2) into a new quantity, T:

$$T = 4 \times INT + AMB - 2 \times OUT + 7$$

The constant was added to avoid negative numbers. INT, AMB, and OUT are the numbers of uniquely in-time, ambiguously in-time, and out-of-time counters for a particular track. The usual range of INT, AMB, and OUT was 0 to 2 with a value of 3 occuring occasionally due to the overlap of the scintillation counters. Table 5-1 shows the distribution in percent of the allowed values of T for the three track types. For example, 31.9% of the stubs did not have any timing information (T=0), while 24.3% were out of time in 2 counters (T=3). The value of T was constrained to lie between 1 and 15, unless there was no timing information in which case T was 0. The value of T was somewhat momentum dependent since the lower momentum tracks sometimes passed through only one counter.

To test the effectiveness of T as a timing indicator, I looked at the value of T for the pion tracks from KO decay and the muon tracks from ψ decay (Alverson, 1979). I also studied the effect that a cut on T had on the number of observed $K^{*\pm}(892)$ decaying into $KO\pi^{\pm}$. Table 5-2 shows the results of this study. I found that 152 KO's in a sample of 1445 (all KO's with QR < 1.) had at least one track with T in the range 1-8. Note that T = 8 corresponds to one counter ambiguously in-time and none uniquely in-time or out-of-time. There were cases of low momentum tracks which hit only the G hodoscope and were ambiguous (the G hodoscope counters were horizontal and there was not much dispersion of the tracks in the Y

TABLE 5-1

FRACTION OF TOTAL NUMBER OF TRACKS WITH EACH VALUE OF T

T	FRACTION (%)		
	LINKED	UNLINKED	STUBS
0	3.5	7.3	31.9
1	0.0	2.6	3.6
2	0.0	0.0	0.1
3	0.6	16.6	24.3
4	0.2	0.8	1.2
5	1.6	3.7	5.1
6	2.0	4.2	5.9
7	2.7	5.1	2.0
8	2.6	3.4	3.6
9	14.6	15.7	11.8
10	0.8	0.9	0.6
11	5.1	4.5	2.1
12	22.4	14.0	4.9
13	1.4	0.8	0.0
14	0.0	0.0	0.0
15	42.4	20.3	2.8

TABLE 5-2

FRACTION OF GOOD LINKED TRACKS WITH 1<T<8

PARTICLE	TOTAL NUMBER	NUMBER WITH 1<T<8 FOR > 1 TRACK	FRACTION OF TRACKS
KO	1445 ± 53	152 ± 8	0.053 ± 0.003
Ψ	147 ± 13	7 ± 1	0.024 ± 0.003
$K^*(892)$	180 ± 40	0.03-0.05	0.03-0.05

direction).

The pions from KO decay tended to be somewhat lower in momentum than the muons from Ψ decay. Since the muons were detected in the P hodoscope, they always passed through at least two counters in the G and H (or H´) hodoscopes. That is why only 7 out of 147 Ψ events had a muon track with T between 1 and 8.

The statistics on the number of $K^*(892)$ particles was poor (180+-40) and so I was not able to obtain a measure of the signal loss with any degree of certainty. I did, however, plot the ratio of the mass spectrum with a cut of T > 8 to that obtained with no cut on T and observed that the cut reduced the signal and background at the same relative rate of about 5 to 10%. The same trick yielded a somewhat smaller reduction in the KO signal relative to the background. The sample of KO´s with no T cut had a signal-to-noise ratio of 1.25:1.0 while the sample with 0 < T < 8 had a signal-to-noise of 0.9:1.0.

The conclusion is that requiring T to be greater than 8 cuts out at most 5% of the linked tracks which are known to be good. The probability of losing a mass combination with two tracks ranges from 5% to 10% depending on the tracks´ momenta.

The second cut on the tracks relates to the type of the track. The question is whether the stubs and unlinked tracks should be used in mass combinations. To answer that question, I once again studied the di-muon and $KO\pi^\pm$ mass spectra.

Using all muon candidates regardless of track type, I determined that there were a total of 149 +- 21 Ψ's. I then used only the linked muon tracks and found 147 +- 13 Ψ's with a much reduced background. Figure 5-3 (a) and (b) show respectively the di-muon mass spectrum for both muons

Figure 5-3. The di-muon mass spectra for (a) both muon tracks linked and (b) one or both muon tracks unlinked.

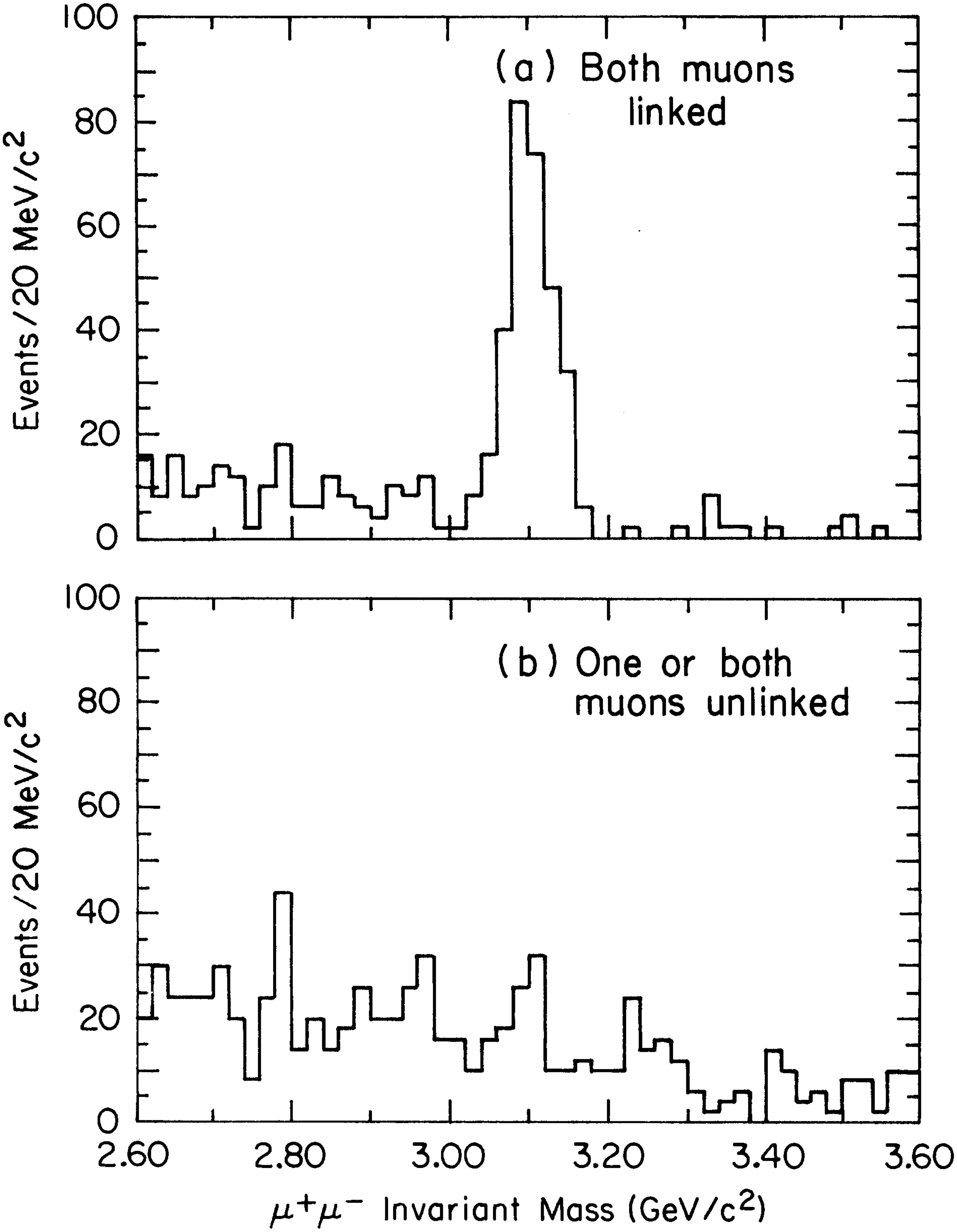
(a) Both muons linked
(b) One or both muons unlinked
Events/20 MeV/c^2
0
20
40
60
80
100
2.60
2.80
3.00
3.20
3.40
3.60
$\mu^+\mu^-$ Invariant Mass (GeV/c^2)

linked and for at least one muon unlinked. I have required T to be greater than 8 for the timing in the M,N,M', and P hodoscopes. There is no visual evidence of the ψ in (b).

This does not prove that the lower momentum unlinked tracks are also "bad". To gain some information about (possibly) lower momentum tracks I studied the $K0\pi^{\pm}$ mass spectrum for linked, unlinked, and low-momentum tracks. Even when I required T to be greater than 8 I observed no significant $K^{*}(892)$ signal in either the unlinked or low-momentum tracks. In Figure 5-4 (a) and (b) I show the $K0\pi^{\pm}$ mass spectrum for linked pion tracks and unlinked pion tracks respectively. No timing cuts were applied to the tracks for these mass spectra. The mass spectrum for $K0\pi^{\pm}$ in which the pion track was a stub rose very rapidly from threshold and peaked at a much lower mass than the spectrum for the linked tracks. This may have resulted from the stub having very similar track parameters to one of the linked tracks from the K0.

I have thus concluded that any signal to be found which contained a stub or an unlinked track would be much less reliable than a signal with only linked tracks. Furthermore, any gain in real signal which could possibly result from the inclusion of the stubs and unlinked tracks would likely be more than offset by the subsequent increase in the combinatorial background.

I have therefore used only linked tracks in the final analysis. Since only a tiny fraction of the linked tracks can be shown to be truly out-of-time, I typically did not use timing cuts. I will indicate those cases in which timing cuts were used when they arise.

5.1.2.2 Chi-square of Track

Figure 5-4. The KO mass spectra for (a) linked pion tracks and (b) unlinked pion tracks.

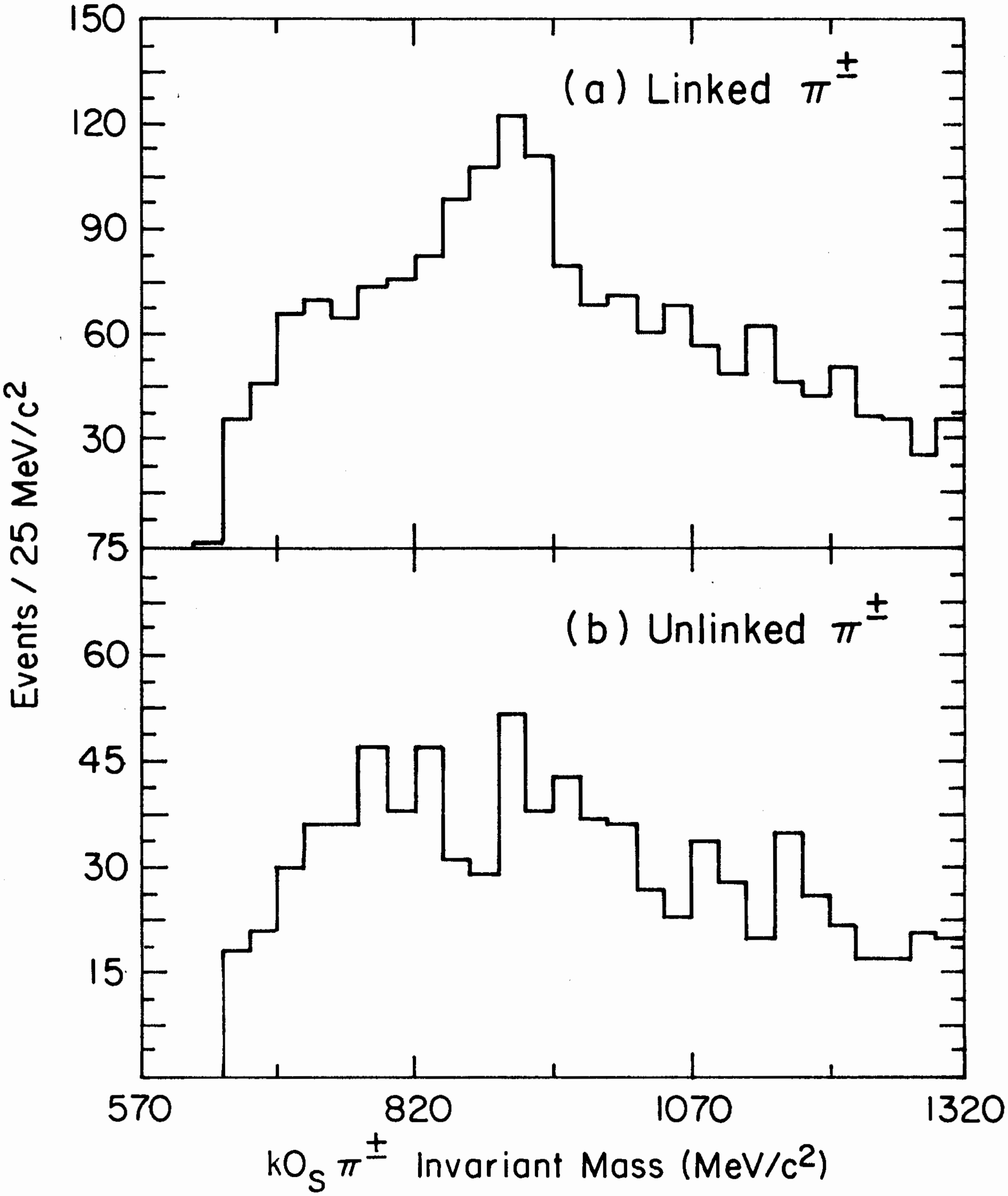
(a) Linked $\pi^{\pm}$
(b) Unlinked $\pi^{\pm}$
Events / 25 MeV/c^2
150
120
90
60
30
75
60
45
30
15
570
820
1070
1320
kO$_S$ $\pi^{\pm}$ Invariant Mass (MeV/c^2)

One of the quantities which resulted from the vertex refitting process was the contribution of each linked track to the total chi-square of the primary vertex. This quantity, χ_t^2, is defined by:

$$\chi_t^2 = (X_v - X_i)^2/\delta X_i^2 + (Y_v - Y_i)^2/\delta Y_i^2$$

where X_v, and Y_v are the coordinates of the fitted primary vertex and X_i, Y_i (δX_i, δY_i) are the coordinates (errors) of track i at the Z position of the vertex. If the track was not included in the final fit of the vertex, the formula remains the same, although the track had no influence on the vertex position.

To illustrate the effect of this cut I used my old friends the ψ and $K^*(892)$. Figures 5-5 and 5-6 show the number of ψ's and $K^*(892)$'s found as a function of the cut on the chi-square of the track(s). For the di-muon spectra, the cut is on the sum of the chi-squares of the two muon tracks, while for the $K0\pi^{\pm}$ spectrum it is on the chi-square of the single pion track. From these figures, I conclude that a cut of 10.0 on a single track or 15.0 on two tracks should not cause a significant loss (< 5%) of a vertex associated signal.

5.1.3 Cut Summary

The following list gives the values of the cuts which I have attempted to justify in the preceding section.

1. Proton momentum less than 0.53 Gev/c ($\beta < 0.5$)
2. Mass recoiling against proton greater than 3.4 Gev/c^2
3. Deviation of vertex from recoil track less than 2.0 standard deviations
4. Linked tracks only

5. Track chi-square less than 10.0 for one track or less than 15.0 for two tracks.

5.2 Results for $K0\pi^+\pi^-$ Final State

This section presents the results of the analysis of the $K0\pi^+\pi^-$ final state. I will first show the results obtained with the set of cuts described in the previous section. Then the results using both more and less restrictive cuts will be shown.

Figure 5-7 shows the $K0\pi^+\pi^-$ invariant mass spectrum obtained with the cuts listed in section 5.1.3. There were, in addition, two cuts on K0 parameters:

1. $480 < \pi^+\pi^-$ mass < 520 Mev/c^2
2. QR < 1.0

There is an excess of 26 ± 8 events in the bin from 1835 to 1885 Mev/c^2. This bin is (roughly) centered on the published mass of the neutral D meson: 1863 Mev/c^2. A maximum likelihood fit with an exponential background plus a Gaussian signal is shown in Figure 5-8. The parameters of the Gaussian are:

1. Mean: 1874 ± 6 Mev/c^2
2. FWHM: 36 ± 10 Mev/c^2
3. Area: 26 ± 8 events

The mass and FWHM are consistent with the fact that the mass and FWHM of the K0 were 499.5 Mev/c^2 and 25 Mev/c^2, and those of the ψ were 3103 and 70 Mev/c^2 respectively. Thus the absolute mass scale is slightly high. Of course, the mass resolution (FWHM) is usually better for combinations

Figure 5-5. Number of ψ's detected as a function of the cut (abscissa) on the total χ^2_t of the two muon tracks.

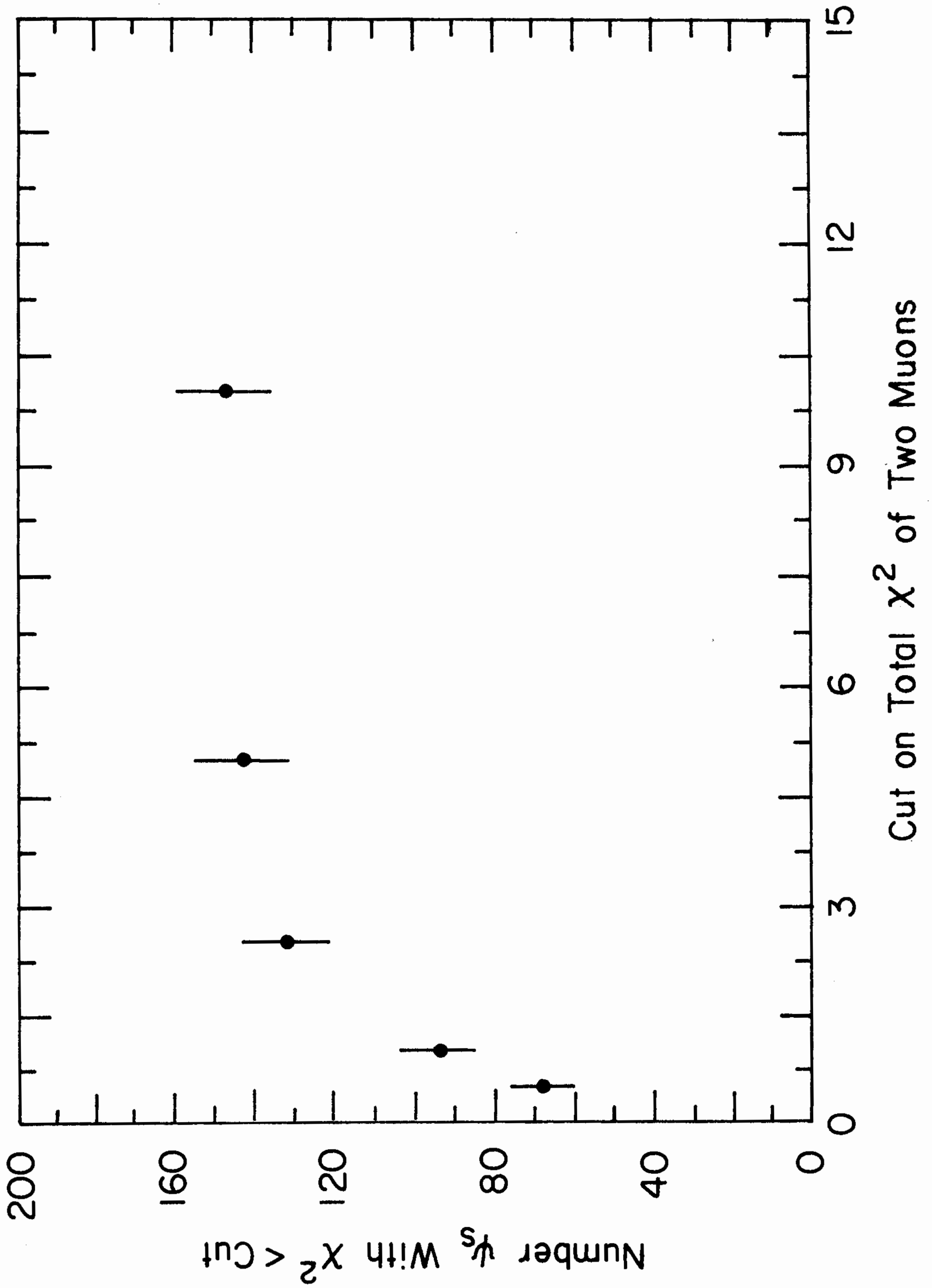
Number ψs With χ² < Cut
0
40
80
120
160
200
Cut on Total χ² of Two Muons
0
3
6
9
12
15

Figure 5-6. Number of $K^*(892)$'s detected as a function of the cut (abscissa) on the χ_t^2 of the pion track.

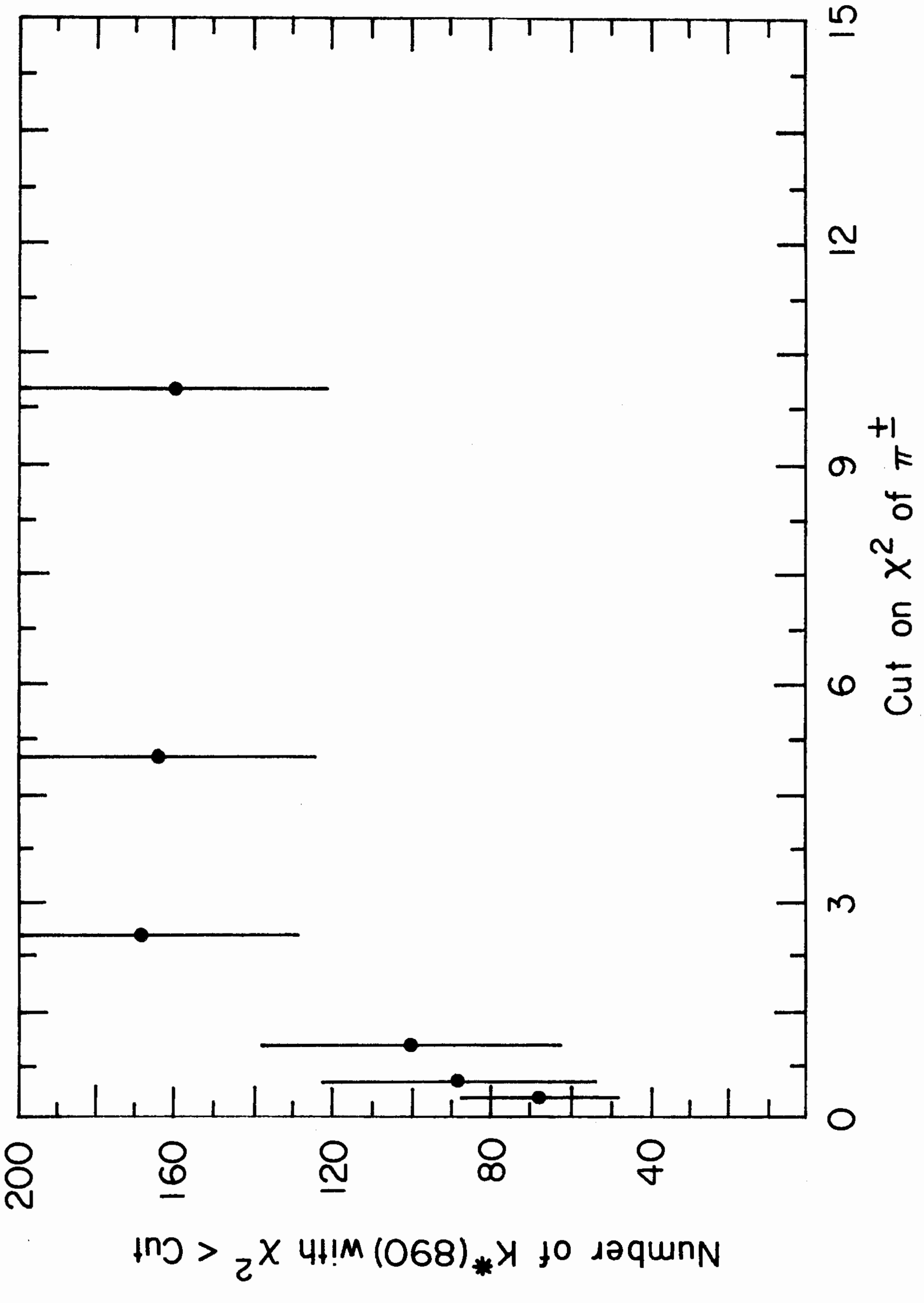
Number of K*(890) with χ^2 < Cut
200
160
120
80
40
0
3
6
9
12
15
Cut on χ^2 of $\pi^\pm$

Figure 5-7. The $K0\pi^+\pi^-$ invariant mass spectrum obtained with the cuts described in the text. The bin from 1835 to 1885 Mev/c^2 contains the D^0 signal.

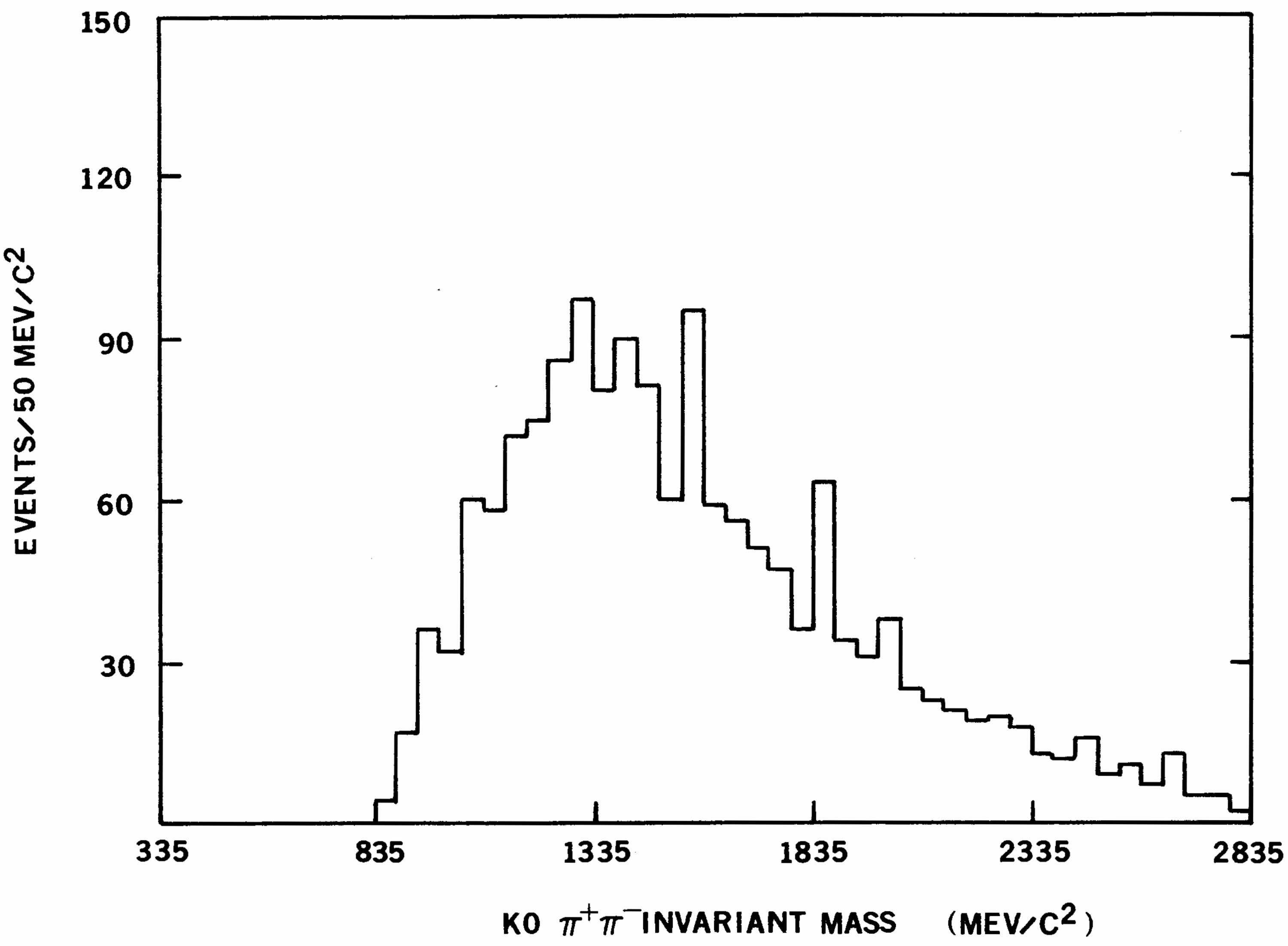
150
120
90
60
30
EVENTS/50 MEV/C^2
335
835
1335
1835
2335
2835
KO $\pi^+\pi^-$ INVARIANT MASS (MEV/C^2)

Figure 5-8. A maximum likelihood fit with Gaussian signal and exponential background. The mean and FWHM of the Gaussian are 1874 and 36 Mev/c^2 respectively. The area is 26 ± 8 events.

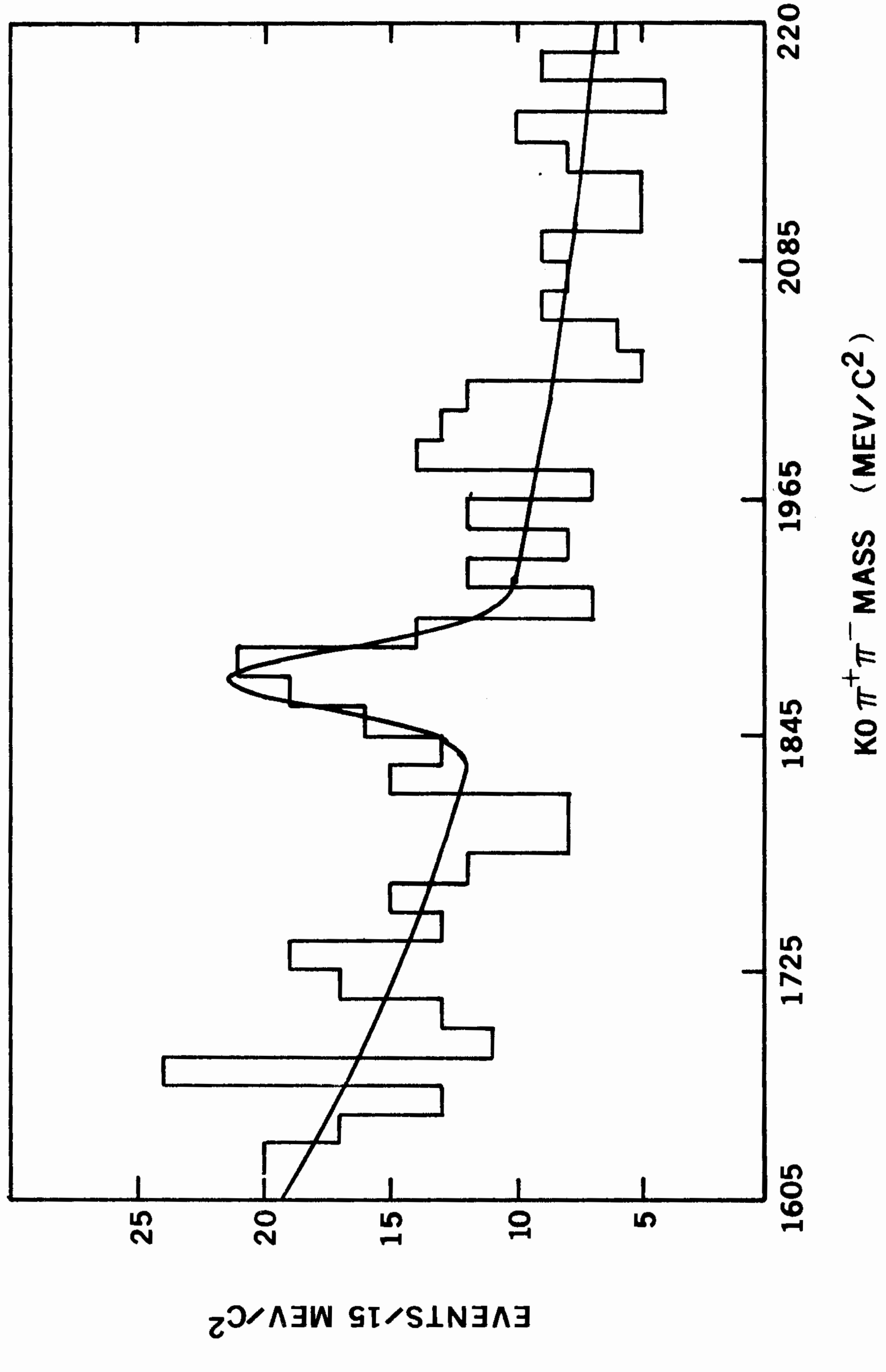
EVENTS/15 MEV/C2
25
20
15
10
5
1605
1725
1845
1965
2085
2205
K0 $\pi^+\pi^-$ MASS (MEV/C^2)

involving 4 tracks (as in $K0\pi^+\pi^-$) than for 2 tracks.

By relaxing some of the cuts, I obtained the mass spectrum in Figure 5-9. The particular cuts loosened and their new values were:

1. Proton momentum < 0.62 Gev/c ($\beta < 0.55$)
2. Deviation of primary vertex from recoil track < 2.5 standard deviations
3. Missing mass cut removed

The background has increased but there is no significant change in the net signal. A fit such as that in Figure 5-8 yielded an area of 27 ± 9 events and virtually the same mass and FWHM.

Finally, an example of the mass spectrum for tighter cuts is shown in Figure 5-10. The cuts for this plot were slightly different in type from those used in the previous plots. Most of the changes involve the K0 parameters. The cut on QR was replaced by three cuts while the only other change from the cuts used in Figure 5-7 was a decrease of the maximum proton momentum and the addition of an upper cut on M_X. The set of cuts thus became:

1. Proton momentum < 0.47 Gev/c ($\beta < 0.45$)
2. $3.4 < M_X < 7.0$ Gev/c^2 (upper cut is new, but reasonable due to proton acceptance cutoff at that value)
3. $-640 < Z_D < -440$ cm (new cut, see Figure 4-9)
4. Distance of closest approach (K0 vertex) < 4.0 mm (new cut, see Figure 4-4)
5. Momentum of K0 > 25 Gev/c (new cut, see Figure 4-12)

6. Sum of chi-squares of pion tracks < 15.0 (no change).
7. Deviation of primary vertex from recoil track < 2.0 standard deviations (no change)

A maximum likelihood fit gives an area of 21 ± 7 events. Thus the tighter cuts have resulted in a possible reduction of the signal by 5 events but the background is smaller by a factor of 2.

Using the mass spectrum in Figure 5-9 (loosest cuts), I have studied the kinematic distributions of the signal plus background and the background. By subtracting the background distribution, I can extract some information concerning the production mechanism. Figure 5-11(a) shows the Feynman X distribution for the signal plus background and the background only. The signal region was always 1835 to 1885 Mev/c^2, while the background distributions were obtained by giving each event in the two bins on either side of the signal (four bins total) a weight of 0.25. The background subtracted Feynman X distribution is shown in Figure 5-11(b).

The corresponding process was done for the distributions of the invariant four-momentum transfer to the proton, t, the mass recoiling against the proton, M_X, and the $\pi^+\pi^-$ invariant sub-mass. These distributions are shown in Figures 5-12, 13, and 14 respectively. The combination of Feynman X values around 0.5, relatively small momentum transfer to the proton, and M_X consistent with $D\bar{D}$ production seems to fit a diffractive production process.

Figure 5-14 indicates a slight enhancement in the $\pi^+\pi^-$ sub-mass at the ρ^0 mass, but it is not significant enough to claim observation of the decay mode $D^0 \to K0\rho^0$. I also studied the $K0\pi^\pm$ sub-masses, but saw no evidence for the cascade process:

Figure 5-9. The $K0\pi^+\pi^-$ mass spectrum with somewhat relaxed cuts.

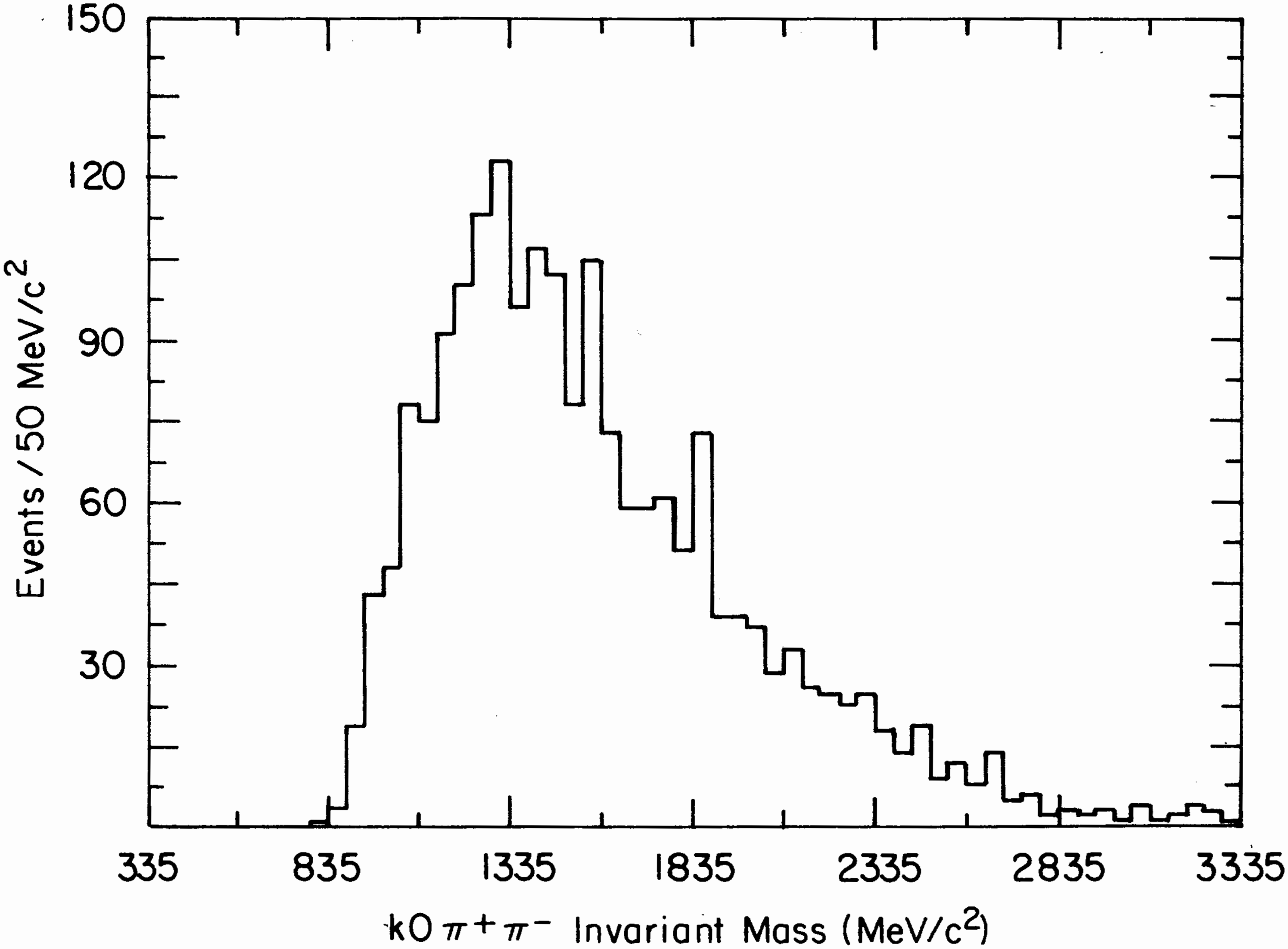

150
120
90
60
30
Events / 50 MeV/c^2
335
835
1335
1835
2335
2835
3335
kO $\pi^+\pi^-$ Invariant Mass (MeV/c^2)

Figure 5-10. The $K0\pi^+\pi^-$ mass spectrum for tighter cuts than used for Figure 5-7.

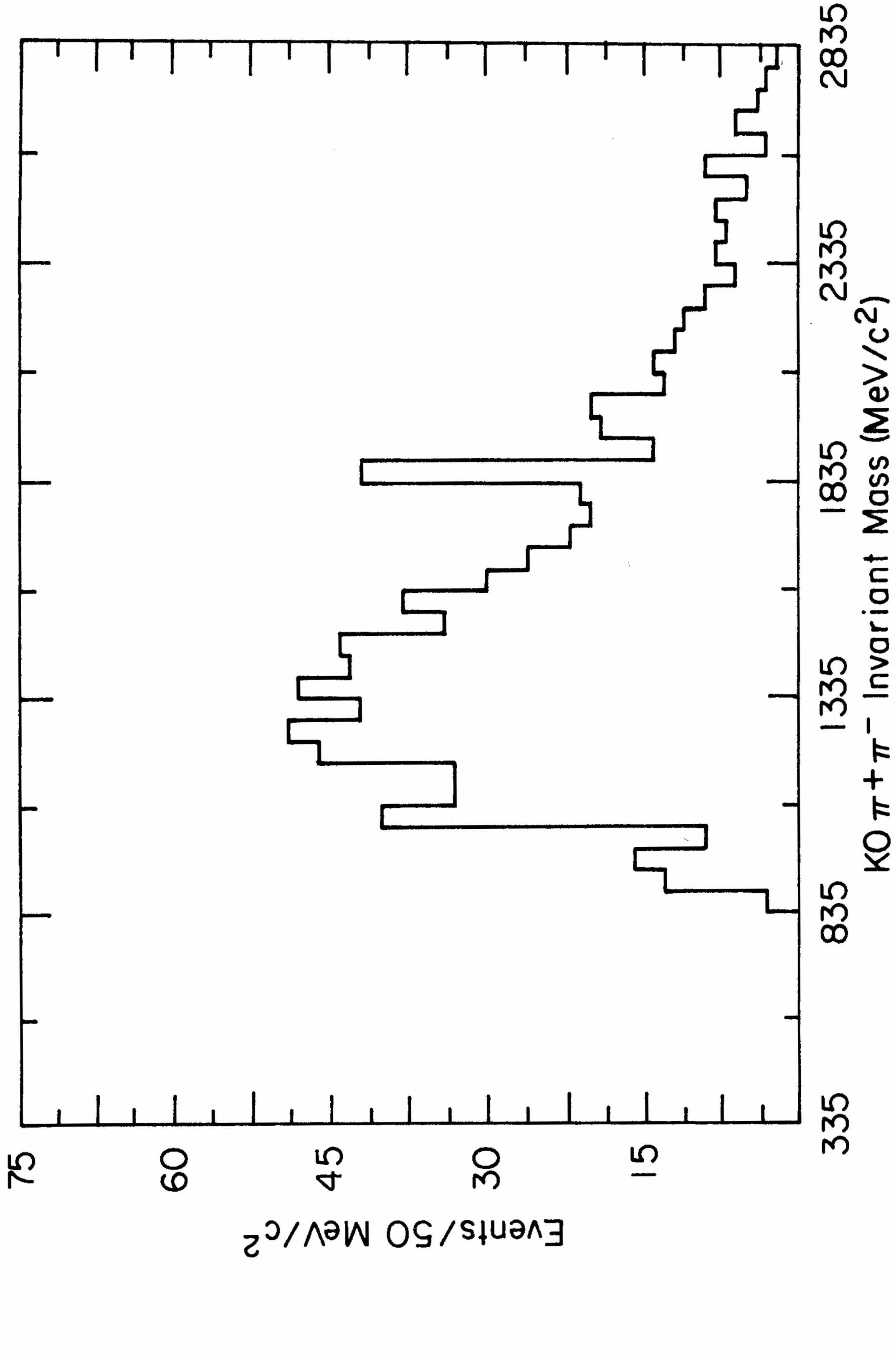
Events/50 MeV/c^2
75
60
45
30
15
335
835
1335
1835
2335
2835
K0 $\pi^+\pi^-$ Invariant Mass (MeV/c^2)

Figure 5-11. The distribution of Feynman X for (a) the signal and background and (b) background subtracted. The background was taken from the two bins on each side of the signal bin (1835-1885 Mev/c^2) and weighted accordingly.

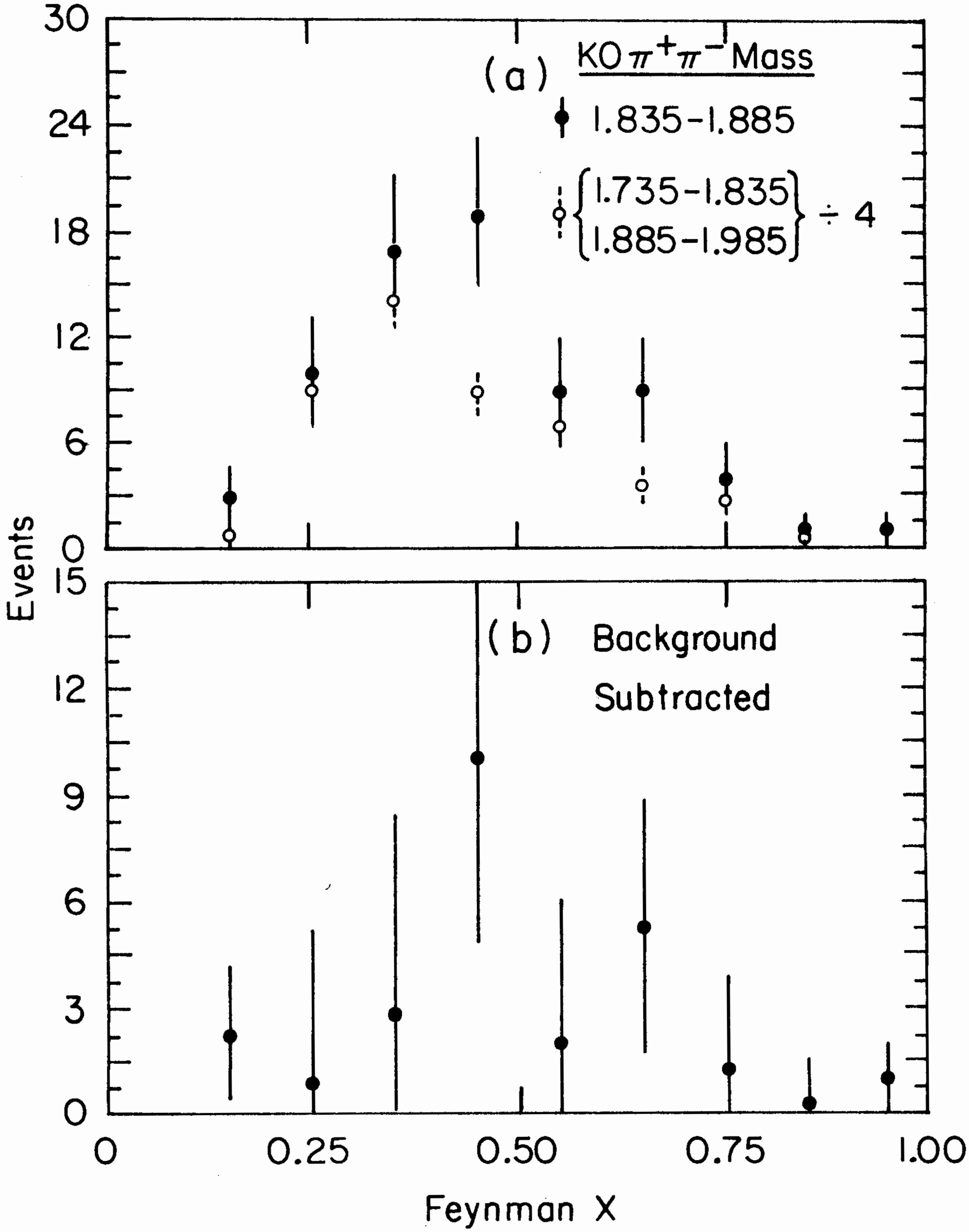
(a)
KO π+π− Mass
1.835-1.885
{1.735-1.835, 1.885-1.985} ÷ 4
(b) Background Subtracted
Events
Feynman X
0
6
12
18
24
30
3
9
15
0.25
0.50
0.75
1.00

Figure 5-12. The distribution of t (invariant four-momentum transfer to the recoil proton) for (a) signal and background and (b) the background subtracted signal.

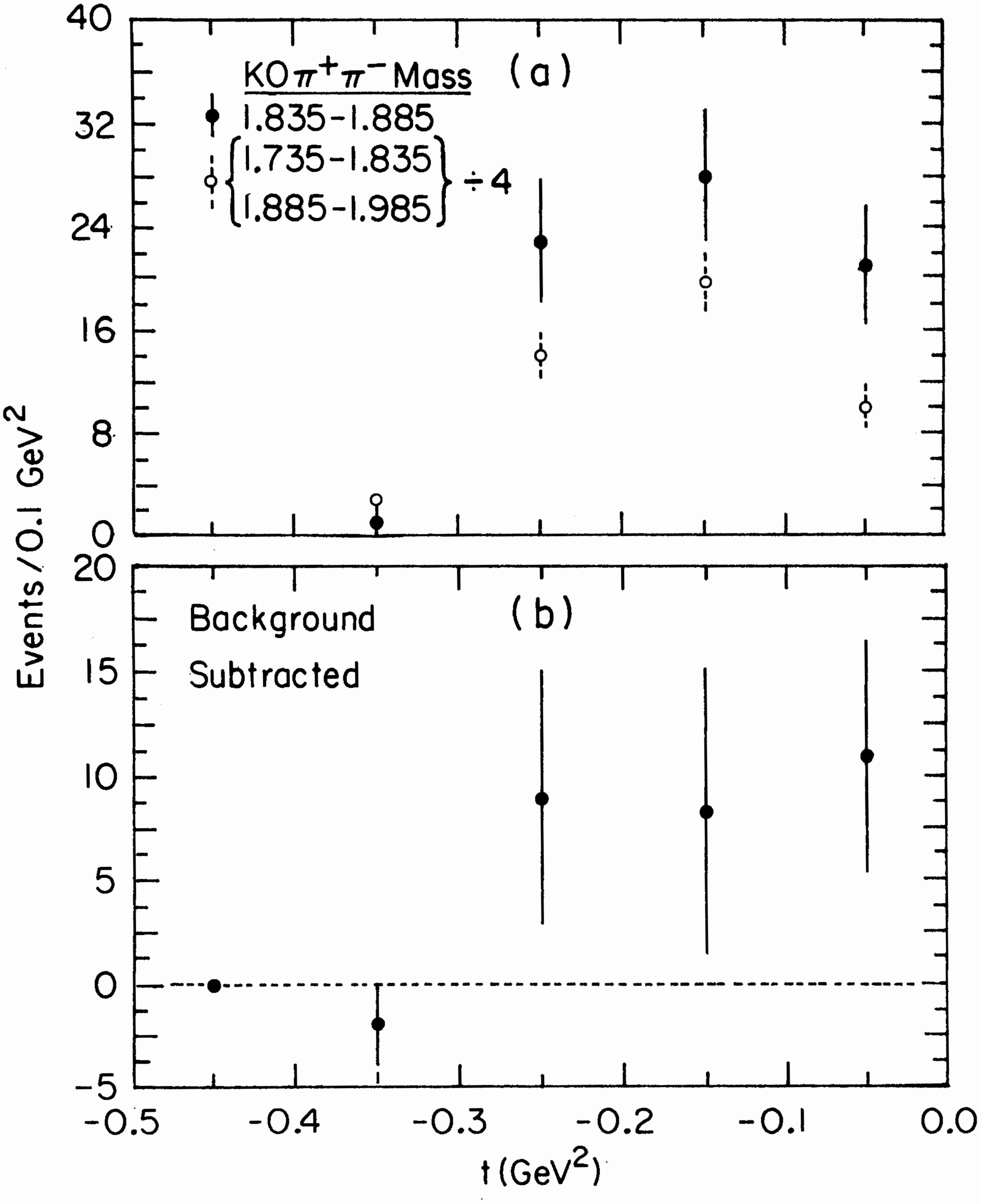

40
32
24
16
8
0
KOπ⁺π⁻ Mass
(a)
1.835-1.885
1.735-1.835
1.885-1.985
÷4
Events/0.1 GeV²
20
15
10
5
0
−5
Background
Subtracted
(b)
−0.5
−0.4
−0.3
−0.2
−0.1
0.0
t (GeV²)

Figure 5-13. The distribution of M_X for (a) the signal and background regions and (b) the background subtracted signal.

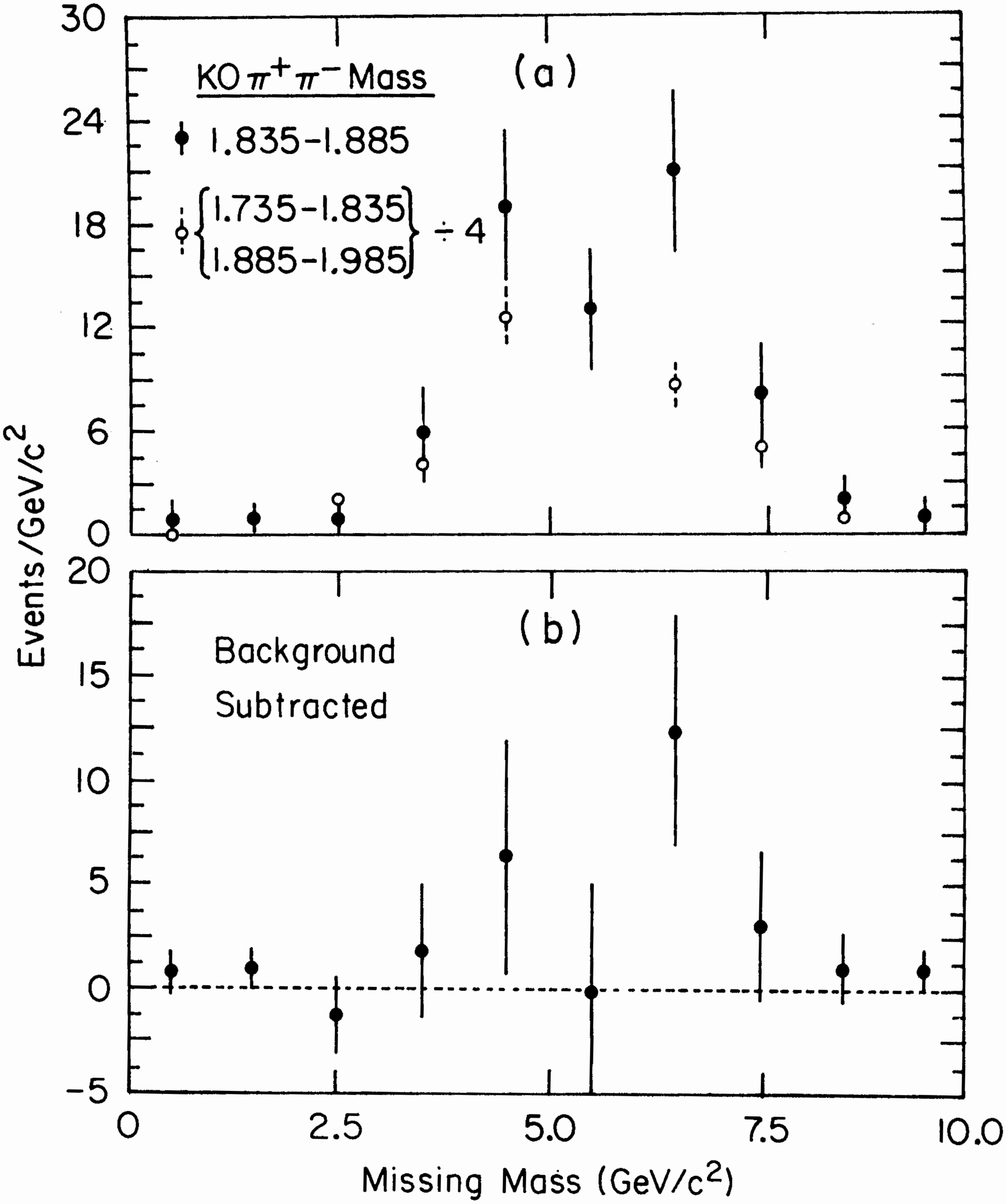
KO $\pi^+\pi^-$ Mass
(a)
1.835-1.885
{1.735-1.835 / 1.885-1.985} ÷ 4
(b)
Background Subtracted
Events/GeV/c²
Missing Mass (GeV/c²)
30
24
18
12
6
0
20
15
10
5
0
-5
0
2.5
5.0
7.5
10.0

Figure 5-14. The $\pi^+\pi^-$ sub-mass for the $K0\pi^+\pi^-$ system for (a) the signal and background regions and (b) the background subtracted signal.

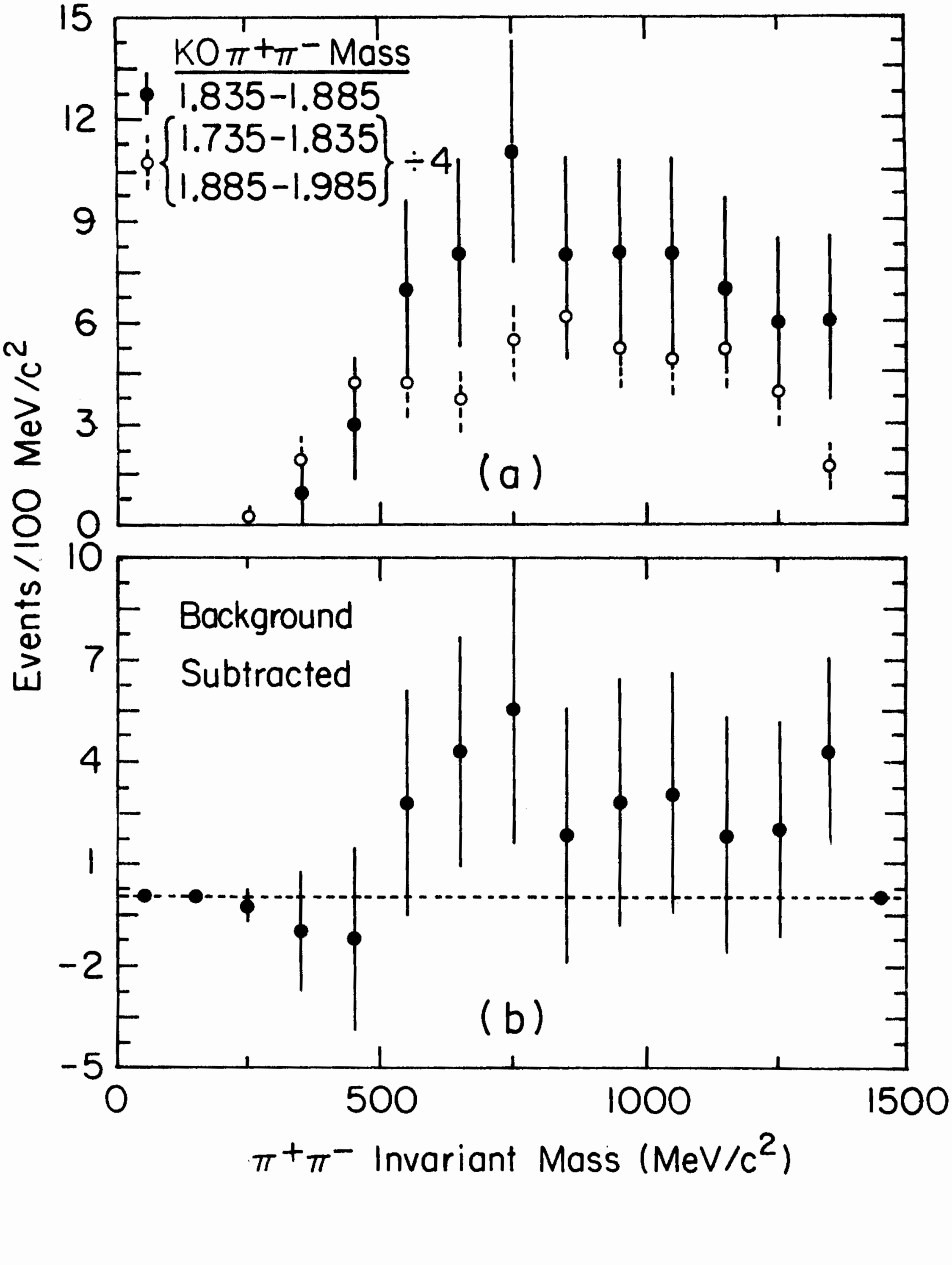
K0$\pi^+\pi^-$ Mass
1.835-1.885
{1.735-1.835, 1.885-1.985} ÷4
(a)
Background
Subtracted
(b)
Events/100 MeV/c²
15
12
9
6
3
0
10
7
4
1
-2
-5
0
500
1000
1500
$\pi^+\pi^-$ Invariant Mass (MeV/c²)

$$D^{o} \to K^{*-}(892)\,\pi^{+}$$
$$\hookrightarrow K0\,\pi^{-}$$

In Figure 5-15, I compare the Feynman X distribution of the background subtracted signal (Figure 11(b)) with the distributions predicted by both diffractive (a) and central (b) production models. The diffractive model is described in Chapter 6. For a typical central model, I assumed that $d\sigma/dX \propto (1-X)^3$, roughly the dependence of ψ production. The diffractive model distribution fits the data better than that of the central model.

In conclusion, I observed an excess of 26 ± 8 events consistent with the decay of the neutral D meson. The production cross section implied by this number of events is calculated in Chapter 6 after a description of the acceptance calculation.

5.3 Results for $K0\pi^{\pm}$ Final State

The only change in cut practices for the $K0\pi^{\pm}$ analysis concerned the KO mass cut. The mass cut for the $K0\pi^{+}\pi^{-}$ analysis was an absolute cut. This cut was loosened and augmented by a relative mass cut. This relative cut was based on the calculated mass resolution for each KO candidate. The deviation of the calculated mass from the known KO mass was required to be less than twice the probable error.

The reason for switching to a relative mass cut was two-fold:

1. KO´s from two body D decay have higher average momentum than those from three body decay
2. The combinatorial background is less of a problem for two body decay modes, so cuts can be less restrictive.

Since the KO mass resolution worsens with increasing KO momentum, a fixed mass cut tends to remove high momentum KO´s. The absolute mass cut was set

Figure 5-15. Comparison of Feynman X distribution for background subtracted D^o signal with predictions of diffractive model (a) and (b) central production model with $d\sigma/dX \propto (1-X)^3$.

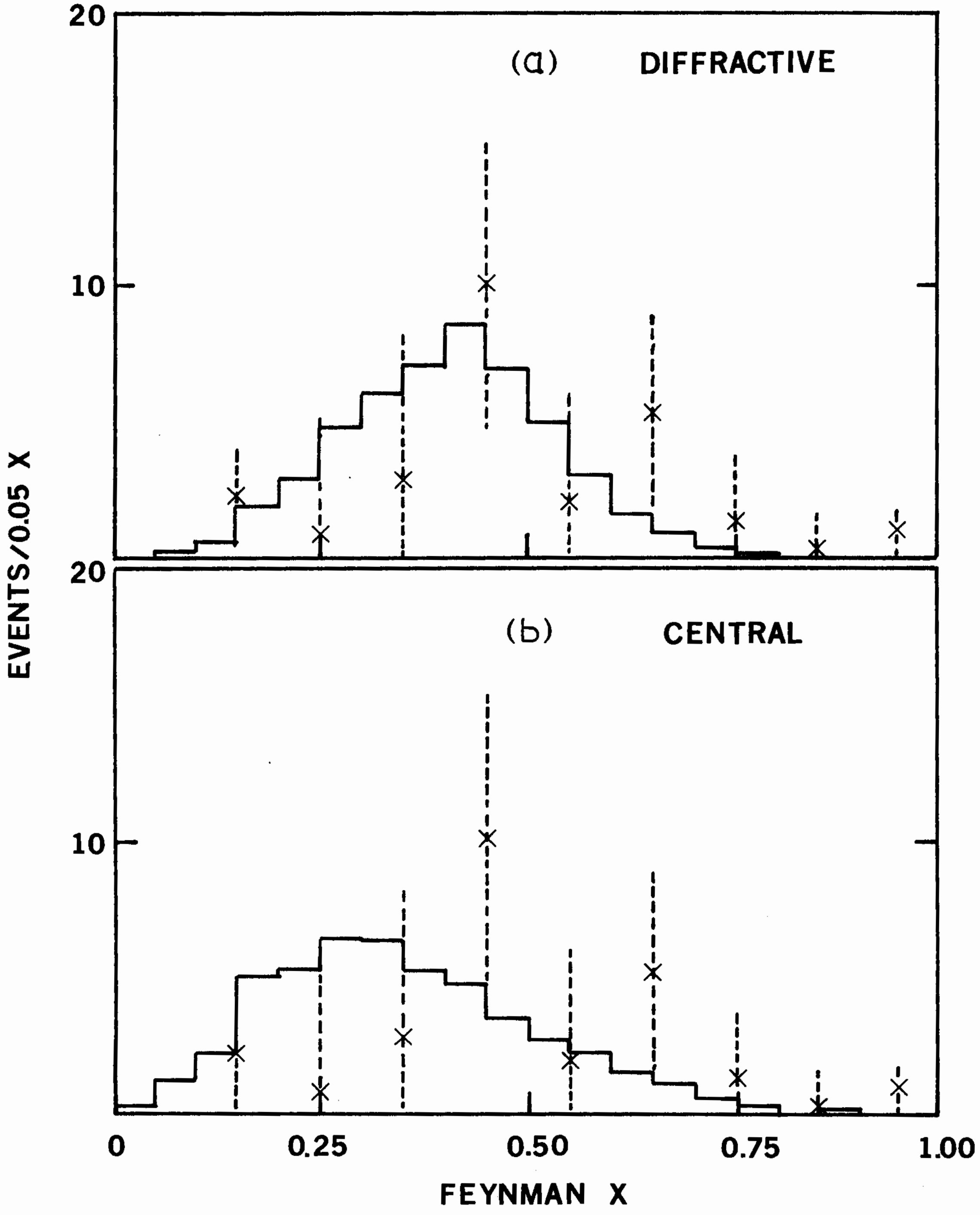
20
(a)
DIFFRACTIVE
10
EVENTS/0.05 X
20
(b)
CENTRAL
10
0
0.25
0.50
0.75
1.00
FEYNMAN X

to 350 to 650 Mev/c^2 basically to remove low mass electron-positron pairs from photon conversions. These show up with masses slightly larger than twice the pion mass, but have large errors on the mass due to the very small opening angle between the tracks.

The evidence for the charged D meson decaying into $K0\pi^{\pm}$ is weak. There is an excess of high momentum (> 40 Gev/c) K0 candidates with $K0\pi^{\pm}$ masses in the 1.84 to 1.88 Gev/c^2 region. In Figures 5-16 and 5-17 I show the $K0\pi^-$ and $K0\pi^+$ invariant mass spectra respectively. The superimposed curves are the result of a maximum likelihood fit such as that done for the $K0\pi^+\pi^-$ mass spectrum. Here the mass and FWHM of the Gaussian were fixed at 1878 Mev/c^2 and 45 Mev/c^2 respectively. The mass value was determined by allowing the mass to be a free parameter and fitting the signal obtained with no K0 momentum cut.

The cuts used to extract these mass spectra were:

1. $350 < \pi^+\pi^-$ mass < 650 Mev/c
2. K0 mass less than 2.0 standard deviations from known mass
3. QR < 1.
4. Missing mass, M_X, > 3.4 Gev/c
5. Deviation of vertex from recoil track less than 3.0 standard deviations (relaxed from value used in $K0\pi^+\pi^-$)
6. Proton momentum < 0.62 Gev/c (relaxed also)
7. K0 momentum > 40 Gev/c

There is no signal consisent with D^+ decay while there is a possible signal consistent with D^- decay. The fits give the areas to be:

Figure 5-16. The K0 π^- invariant mass spectrum for K0 momenta greater than 40 Gev/c. The maximum likelihood fit was done with the mean and FWHM of the Gaussian fixed at 1878 and 45 Mev/c^2 respectively. The area of the Gaussian was 12.5 ± 4.6 events.

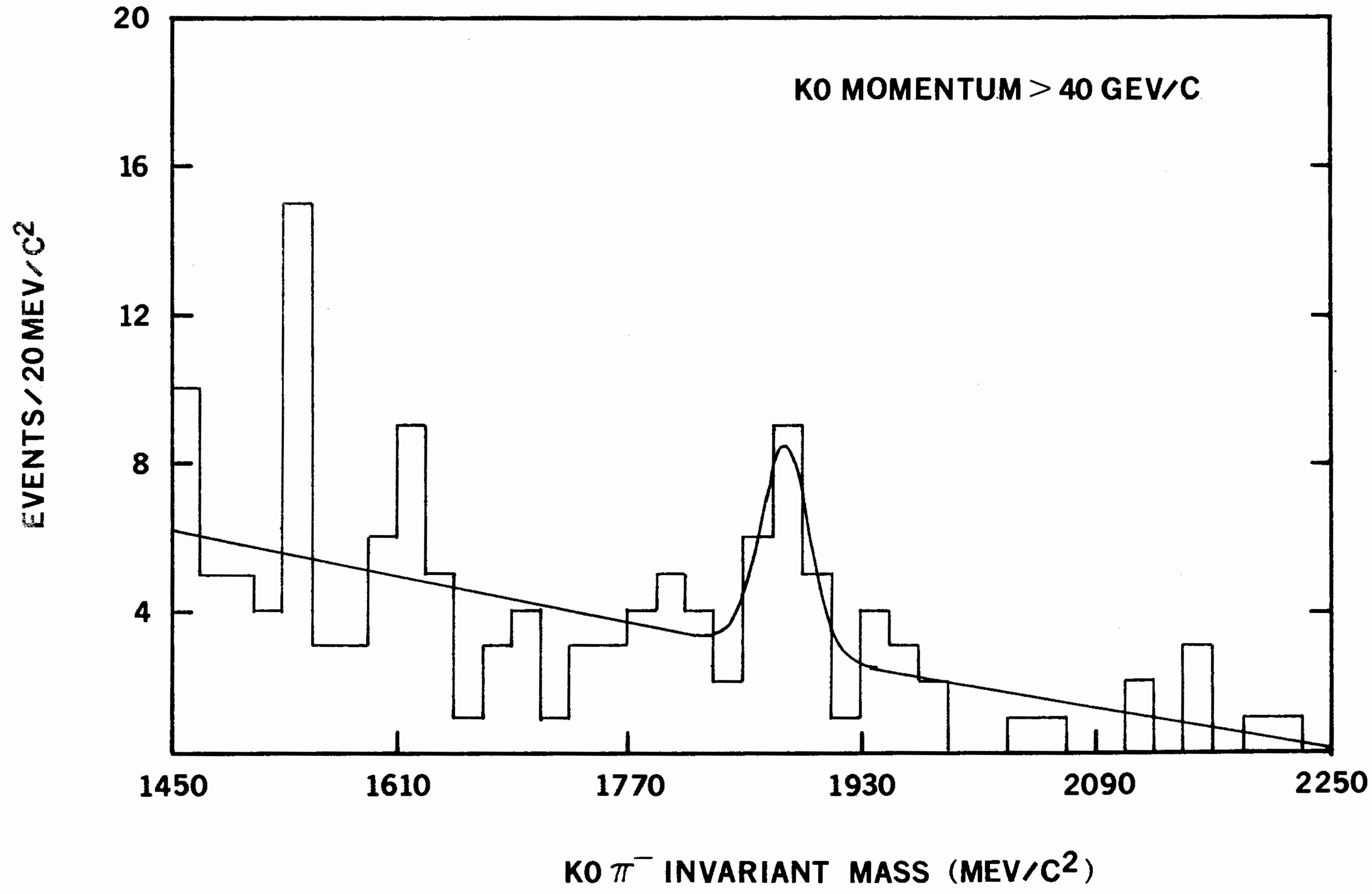
KO MOMENTUM > 40 GEV/C
20
16
12
8
4
EVENTS/20 MEV/C^2
1450
1610
1770
1930
2090
2250
KO π^- INVARIANT MASS (MEV/C^2)

Figure 5-17. The $K0\pi^{+}$ invariant mass spectrum for K0 momenta greater than 40 Gev/c. The maximum likelihood fit was done with the mean and FWHM of the Gaussian fixed at 1878 and 45 Mev/c^2 respectively. The area of the Gaussian was 0.2 ± 3.0 events.

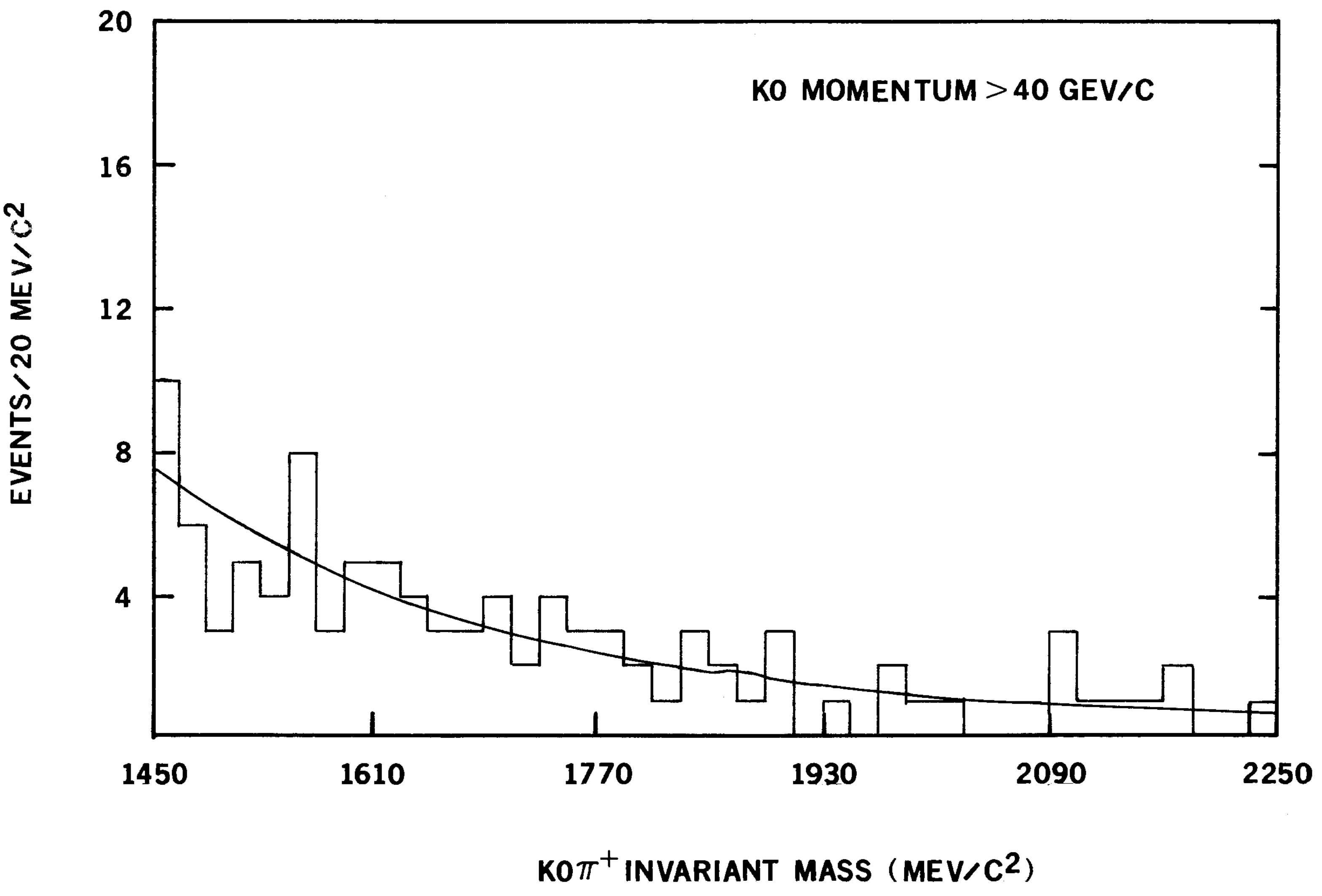
K0 MOMENTUM > 40 GEV/C
EVENTS/20 MEV/C2
20
16
12
8
4
1450
1610
1770
1930
2090
2250
K0π+ INVARIANT MASS (MEV/C2)

1. D^+: 0.2 ± 3.0 events
2. D^-: 12.5 ± 4.6 events

The dependence of the number of events on the KO momentum cut is illustrated in Figure 5-18. The number of events from the maximum likelihood fits described is plotted as a function of the KO momentum cut. The dashed curve shows the dependence obtained from the Monte Carlo data. The Monte Carlo is described in Chapter 6. The data points for the 40 Gev/c cut were obtained from Figures 5-16 and 5-17.

It is evident that the signal has a marginal significance. The fact that the $D^\pm$ has been observed through its $K^\mp\pi^\pm\pi^\pm$(exotic) decay mode in the same sample of data (MacKay, 1980) makes the results somewhat more believable. A total of 50 ± 12 $D^\pm$ were seen in that decay mode, corresponding to a cross section of about 10μb in the diffractive region. There were approximately equal numbers of D^+ and D^-.

The fact that I observe a signal only in the KOπ^- mass spectrum is a possible indication that the signal is only a fluctuation of the background. There is also the possibility that there is an excess of D^- due to the fact that the final state (excluding the recoil proton) must have a net negative charge.

There was one additional test which I made. If the muon trigger for a $D\bar{D}$ event resulted from the muon from the semi-leptonic decay of one of the Ds, there will be a correlation between the charge of the muon and the charge of the reconstructed D. The muon and the reconstructed D should have opposite charges. I have imposed such a cut on the KOπ^- and KOπ^+ mass spectra shown in Figure 5-19. The charge of the triggering muon was inferred from the side (positive or negative X) of the M' and/or P

Figure 5-18. The maximum likelihood number of D^- and D^+ events as a function of the KO momentum cut. The dashed curve shows the dependence obtained from the Monte Carlo discussed in Chapter 6.

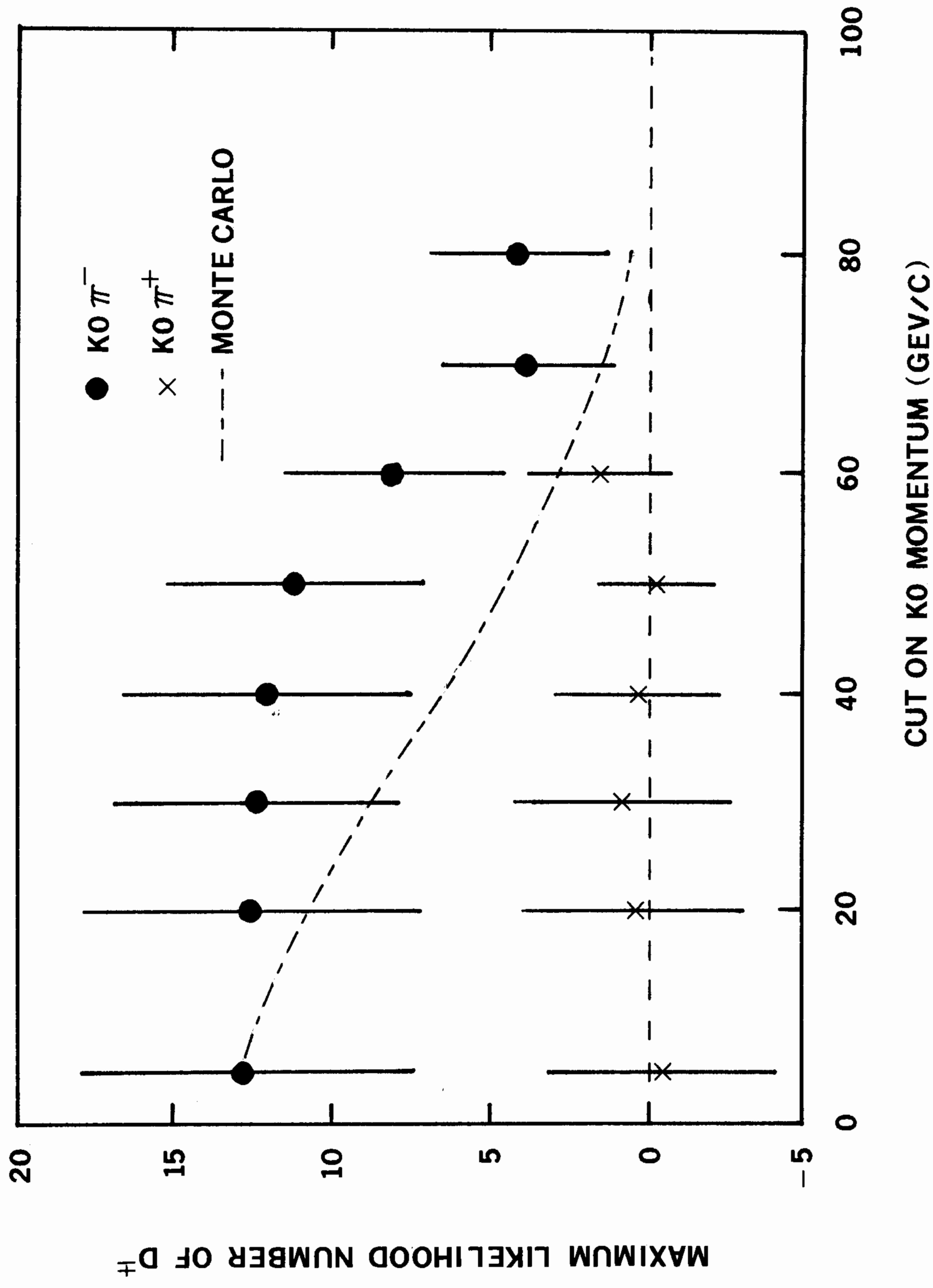
● K0 π^-
× K0 π^+
- - - MONTE CARLO
MAXIMUM LIKELIHOOD NUMBER OF D±
CUT ON K0 MOMENTUM (GEV/C)
20
15
10
5
0
−5
0
20
40
60
80
100

Figure 5-19. The $K0\pi^-$ mass spectrum requiring a "μ^+" (a) and (b) the $K0\pi^+$ spectrum requiring a "μ^-". The charge of the triggering particle was inferred from the side of the M′ and/or P hodoscopes in which the fired counter(s) was located.

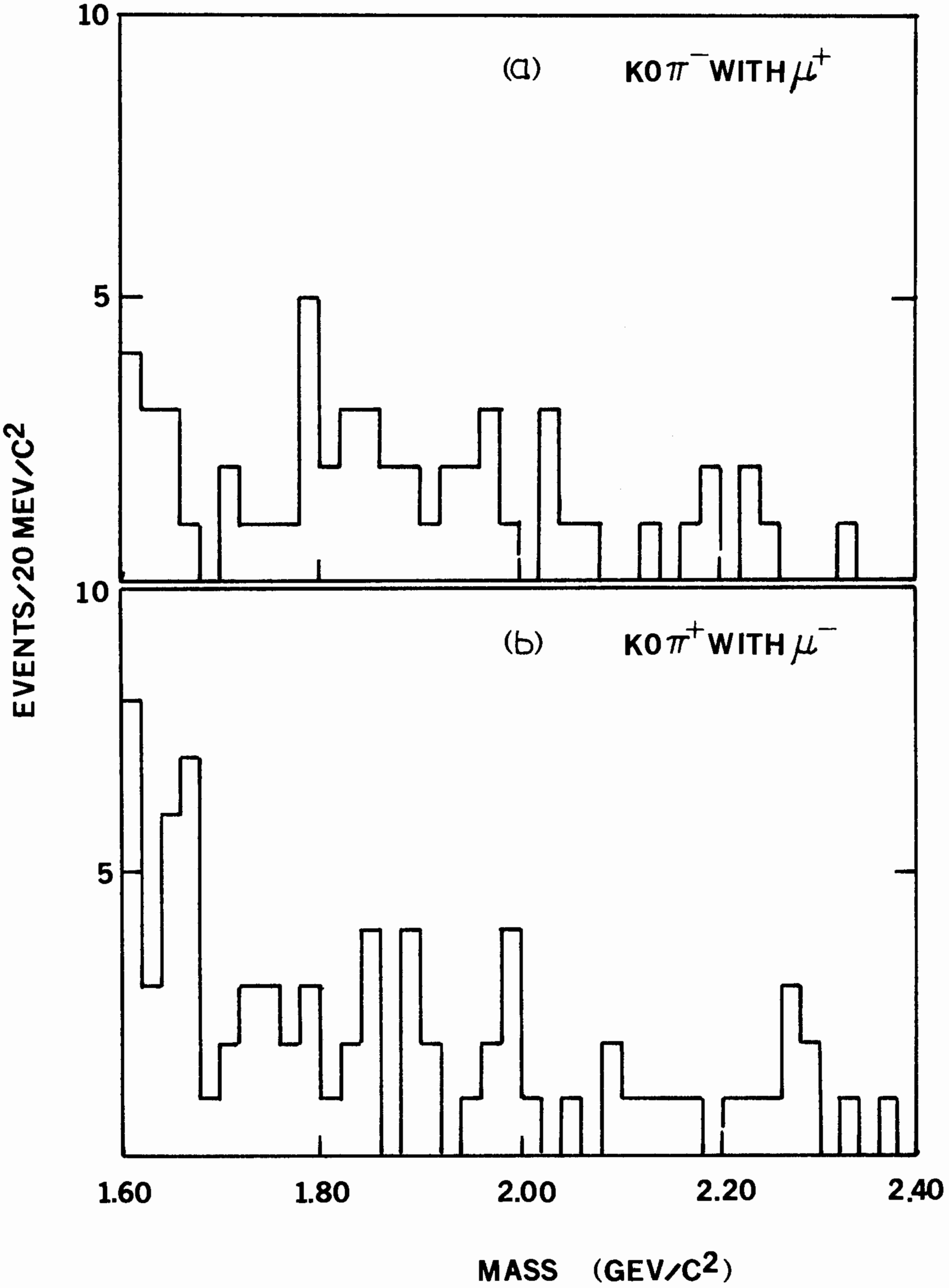
10
(a) K0π^- WITH μ^+
5
10
(b) K0π^+ WITH μ^-
5
EVENTS/20 MEV/C^2
1.60
1.80
2.00
2.20
2.40
MASS (GEV/C^2)

hodoscope having a fired counter. Since the transverse momentum kick (2.1 Gev/c) of the CCM was larger than most muons' transverse momenta, the correlation between muon charge and X intercept at the M' and P hodoscopes was very good. One additional cut was used: the mass recoiling against the $K0\pi^{\pm}$ after removing the recoil proton was required to be greater than 1.4 Gev/c^2. This cut removes combinations which were not consistent with pair production of charmed particles.

From these plots, I calculated the 90% confidence level upper limits on the number of $D^{\pm}$ events coming from D^+D^- production assuming a prompt muon trigger from one of the Ds. The limits are given in Table 5-3, which is a summary of the results. In view of recent developments ($B(D^+ \to \mu^+ + X) = 23\%$; $B(D^0 \to \mu + X) < 4\%$, 90% confidence level) concerning the semi-leptonic branching ratios for the charged and neutral D (Bacino, 1980), no correlation between the charge of the muon and the charge of the D would be found if the other D were neutral. Less than 1.6% (40% muon acceptance X 4% $B(D^0 \to \mu + X)$) of all D s produced would result in a prompt muon trigger, which is considerably less than the 5% probability of a trigger from background sources (pion decay and penetration of the steel absorber by hadrons).

The 12 $K0\pi^-$ events consistent with D^- decay have roughly equal numbers of muons (determined by counter positions as described above) of the same and opposite charge.

Although 12 events is not much to go on, I have tried to extract the Feynman X distribution of these possible D^- candidates. As for the $K0\pi^+\pi^-$ data, I show in Figure 5-20 the Feynman X distribution for the signal bin and background bins, and the background subtracted distribution in (b). I have not done this for the M_X or momentum transfer distributions, simply because the statistical significance is inadequate.

The numbers of events and limits on the numbers of events are categorized in Table 5-3. These values are used to calculate cross sections or limits on cross sections in Chapter 6. The numbers of $D^{\pm}$ with no muon cuts were obtained with the same cuts (except for the muon cut) as used to obtain the limits for $D^{\pm}$ with an oppositely charged muon. The values are very slightly different, but still consistent with those found above.

TABLE 5-3

RESULTS OF $K0\pi^{+}\pi^{-}$ AND $K0\pi^{\pm}$ ANALYSIS

CHARMED MESON	NUMBER (90% CL UPPER LIMITS)
$D^{0} + \overline{D^{0}}$	26 ± 8
D^{-}	10 ± 5
D^{+}	2^{-2}_{+4}
D^{-} with μ^{+}	< 5
D^{+} with μ^{-}	< 5

Figure 5-20. The Feynman X distribution for the $K0\pi^-$ events. The distribution for the signal and the background regions are shown in (a), and the background subtracted distribution in (b).

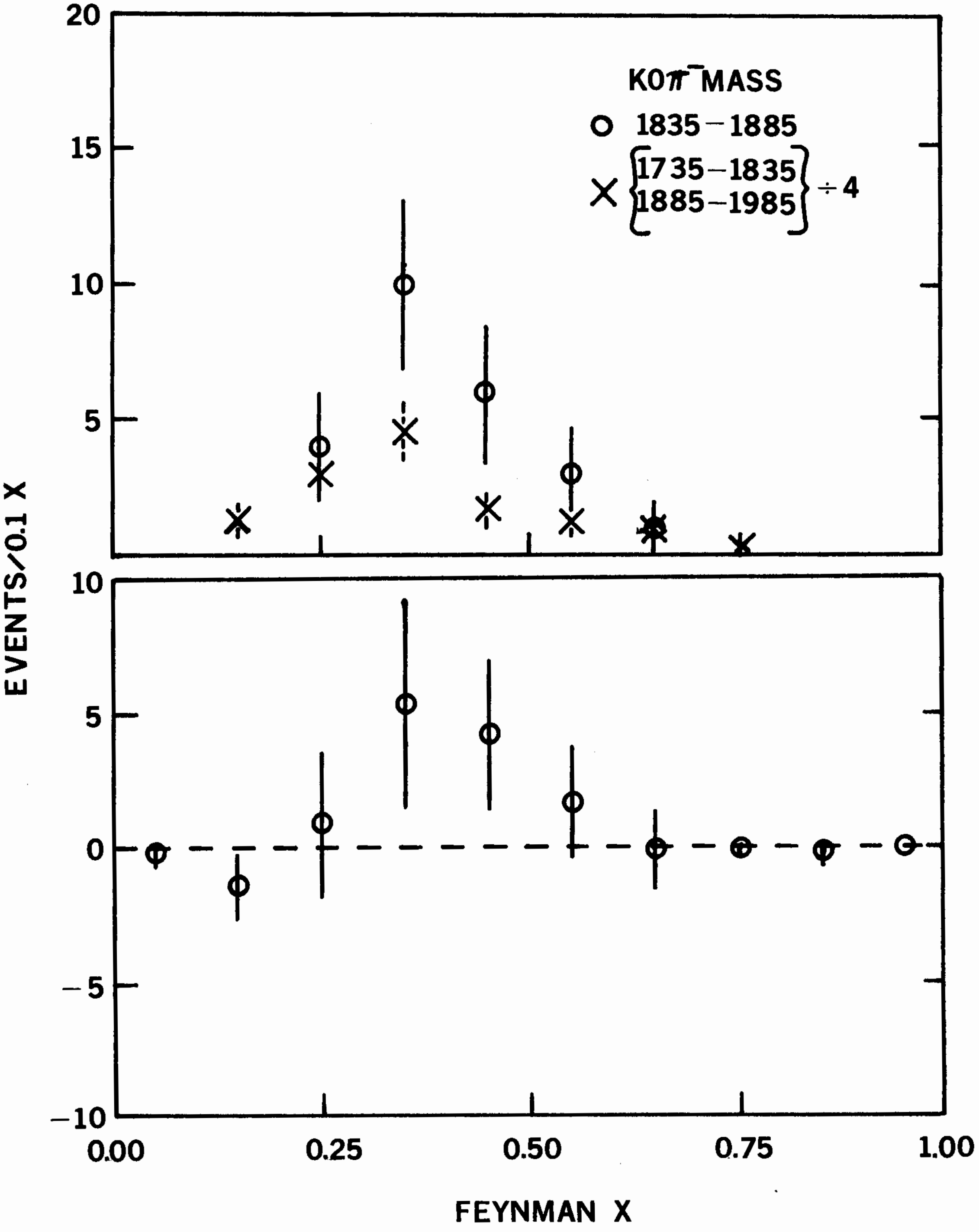
K0π⁻ MASS
○ 1835 – 1885
× {1735 – 1835, 1885 – 1985} ÷ 4
20
15
10
5
0
−5
−10
EVENTS/0.1 X
0.00
0.25
0.50
0.75
1.00
FEYNMAN X

CHAPTER 6

ACCEPTANCE AND CROSS SECTIONS

This chapter covers the details of the acceptance and cross section calculations. The acceptance was calculated with a simple model of diffractive hadronic interactions.

6.1 Acceptance Calculations

The probability of detecting a D meson, given that one was produced, is needed for a cross section calculation. The usual method for determining the acceptance in such complex experimental situations is by a Monte Carlo technique. Since the acceptance of the particle in question depends upon its momentum, the model by which the particle is produced partially determines the acceptance.

This experiment was optimized (for acceptance) by using a parametrization of results of previous experiments on diffractive processes. Thus it was natural to use this same model for the acceptance calculation. The model used produced a recoil proton plus a high momentum "fireball" according to:

$$\frac{d^2\sigma}{dt\,dM_X^2} \propto e^{-b|t|}$$

where t is the four-momentum transfer to the recoil proton and M_X is the mass of the recoiling system. These variables were defined in Chapter 1.

The exponential slope, b, is a function of M_X and is given by:

$$b = 4.6 + 7.0 \times \exp(-34.7 \times M_X^2/s)$$

where s is the total center of mass energy squared. This parametrization of the M_X dependence of the exponential slope fits both 40 Gev Serpukhov $\pi^- + P \rightarrow P + X^-$ data (Antipov, 1973) and 205 Gev $P + P \rightarrow P + X^+$ data

(Barish, 1973).

The Monte Carlo method I used for determining the acceptance plus reconstruction efficiency for the D meson decaying into $K0\pi^{\pm}$ and $K0\pi^{+}\pi^{-}$ was as follows:

1. Generate recoil protons by above recipe until one is accepted
2. Let X^{-} decay into $D\bar{D}\pi$
3. Let one D decay into $K\mu\nu$ and check muon acceptance - if not accepted, start over at step 1.
4. Let other D decay into $K0\pi^{\pm}$ $(K0\pi^{+}\pi^{-})$
5. Let K0 decay into $\pi^{+}\pi^{-}$ with known lifetime and check for acceptance of $\pi^{+}\pi^{-}$. If either pion not accepted (linked), start over at step 1.

The acceptance criteria for the proton were complex in view of the 1 MU.P trigger requirements (see section 3.2). The proton was required to have a momentum consistent with the time-of-flight cuts in the trigger, and had to pass through an allowed MWPC and recoil scintillation counter combination. The muon acceptance was determined the intercept of its track with the M′ and P hodoscopes. The limits used corresponded to the counters used in the 1 MU.P trigger (see Figure 3-8).

I have thus simulated a 1 MU.P trigger with the additional requirement that the K0 decay within the fiducial region and the two pions from the K0′s decay be linked or at most one be a stub. This requirement simply avoided further processing of an event with no chance of having a detectable K0.

I will now explain the process by which the probability of a track being linked, unlinked, or low-momentum (stub) was determined. A Monte Carlo program, written by several persons and somewhat modified by myself, existed which could simulate the apparatus. It included MWPC and WSC inefficiencies, extra sparks at random, and generated output (coordinates of sparks in the chambers, etc.) which could then be analyzed in a (almost) normal manner.

Using this program, I generated events with tracks of fixed momentum and perpendicular momentum but random azimuthal orientation. The origin of the tracks was uniformly distributed throughout the LH2 target. I gave the program MWPC efficiences (listed in Table 6-1) determined from the real data. The WSC efficiencies were set at 90%. Tracks were propagated through the CCM by use of a map of the magnetic field.

The program generated 1000 tracks at each of 50 different combinations of $|\vec{P}|$, and $P_\perp$. These events were analyzed by the trackfinding programs, after which I tabulated the fractions of linked, unlinked, and low-momentum tracks at each generated value of $|\vec{P}|$, $P_\perp$. Interpolation between generated values was done by fitting each set of three points with a cubic polynomial. This was done first for the total momentum and then each of the interpolated points was further interpolated with respect to $P_\perp$. The result was a three-dimensional matrix of probabilities indexed by $|\vec{P}|$, $P_\perp$, and track type. Figure 6-1 summarizes these results for a representative sample of $|\vec{P}|$, $P_\perp$ values.

To use these probabilities in the acceptance Monte Carlo, I simply look up the three probabilities corresponding to linked, unlinked, and stub for the $|\vec{P}|$, $P_\perp$ values of the track in question. The final outcome is determined by the value of a random number. The process is analagous to

TABLE 6-1

MWPC EFFICIENCIES USED IN MONTE CARLO

PLANE NUMBER	PLANE TYPE	EFFICIENCY
7	Y	0.82
8	X	0.87
9	Y	0.88
10	X	0.86
11	Y	0.90
12	X	0.90
13	Y	0.87
14	X	0.83
61	U	0.49
62	V	0.75
63	U	0.87
64	V	0.00
67	Y	0.74
68	X	0.90
69	X	0.92
70	Y	0.88
27	X	0.93
28	Y	0.95

Planes listed in order of increasing Z.

Figure 6-1. The efficiency for finding and linking a track as a function of the track's $|\vec{P}|$ and $P_{\perp}$.

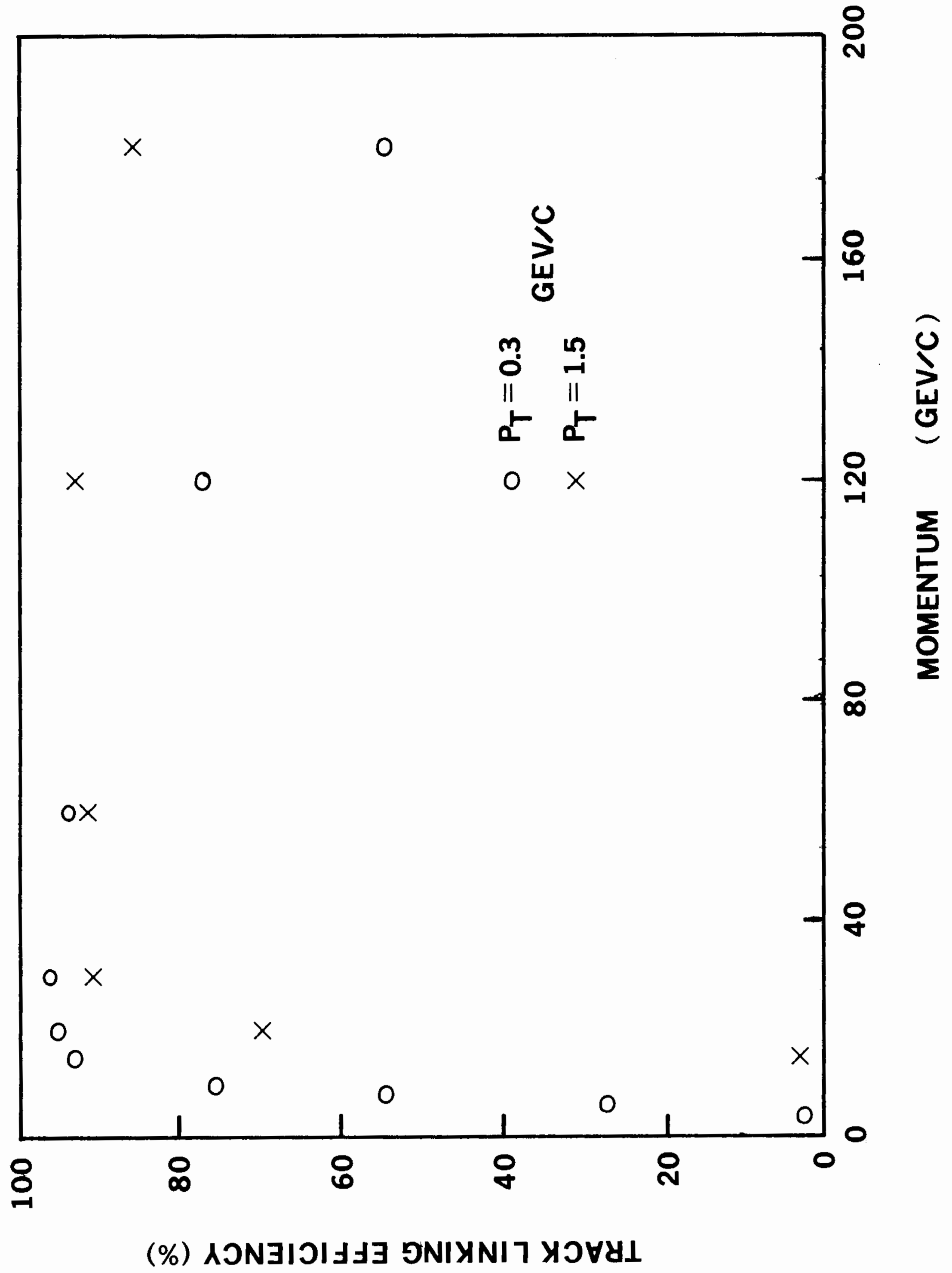
TRACK LINKING EFFICIENCY (%)
0
20
40
60
80
100
MOMENTUM (GEV/C)
0
40
80
120
160
200
○ $P_T = 0.3$ GEV/C
× $P_T = 1.5$

tossing a ball over one's head while blindfolded into four bins marked Linked, Unlinked, Stub, and None of the Above. (The ball is constrained to fall into one of the bins with unit probability.) The relative sizes of the bins are set by the probabilities in the matrix. Each track generated in the acceptance Monte Carlo was tagged in this way, while only the tracks from the KO were required to be linked (or at most one stub).

The last step in the acceptance calculation was to perform the KO reconstruction analysis and to count the number of D mesons found. To simulate the real data for the purpose of KO reconstruction (the tracks are still exactly as generated), the experimental resolution was introduced by adding Gaussian deviations to the track parameters and momenta. With these resolutions determined by the probable errors found from the real data, distributions such as χ^2_V, DCA, and the KO mass spectrum looked much like the real data.

With the KO's which passed the reconstruction process, I formed the appropriate mass combinations and determined the number of D mesons reconstructed. As in the analysis of the real data, only linked tracks were allowed to contribute. The final number for the total D detection probability was then obtained by dividing the number of reconstructed Ds by the total number of protons generated.

The acceptance was calculated at several values of M_X from slightly above $D\overline{D}$ production threshold to the upper limit of the proton acceptance. Figure 6-2 summarizes the results for the total efficiency as a function of M_X for both the $KO\pi^{\pm}$ and $KO\pi^{+}\pi^{-}$ decay modes. Figure 6-3 shows the acceptance of the spectrometer for these decay modes as a function of the Feynman X of the D. A breakdown of the contributions of the proton, muon, and KO acceptance as well as the contributions from the KO reconstruction

Figure 6-2. The total detection efficiency for the (a) KO$\pi^+\pi^-$ decay mode and (b) KO$\pi^\pm$ decay mode. This efficiency includes the proton acceptance, muon acceptance, KO acceptance and reconstruction efficiency and the efficiency for linking the tracks.

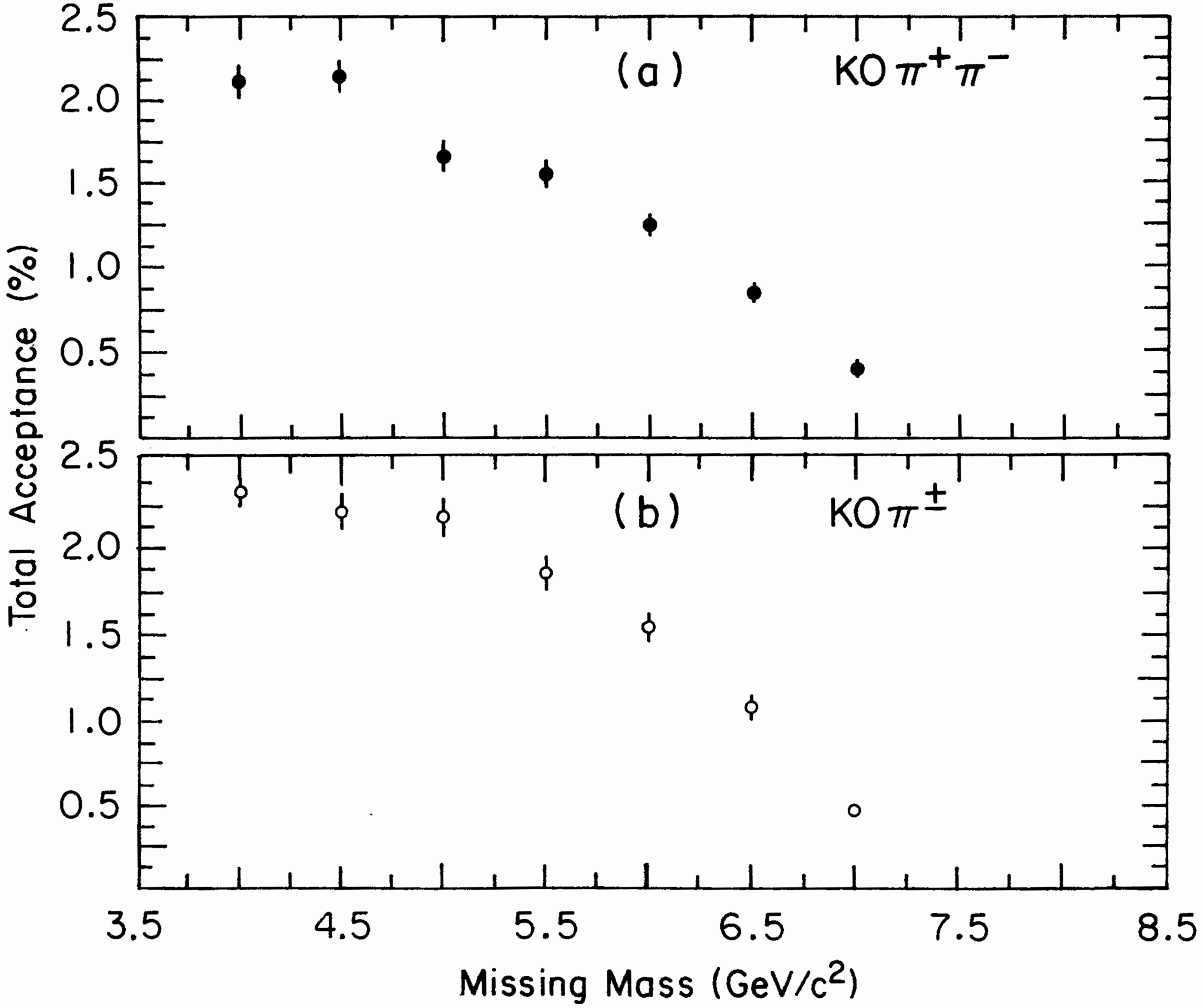
(a)
KO$\pi^+\pi^-$
(b)
KO$\pi^\pm$
Total Acceptance (%)
2.5
2.0
1.5
1.0
0.5
2.5
2.0
1.5
1.0
0.5
3.5
4.5
5.5
6.5
7.5
8.5
Missing Mass (GeV/c^2)

Figure 6-3. The acceptance of the D (excluding proton) as a function of its Feynman X for (a) the $K0\pi^+\pi^-$ decay mode and (b) the $K0\pi^\pm$ decay mode.

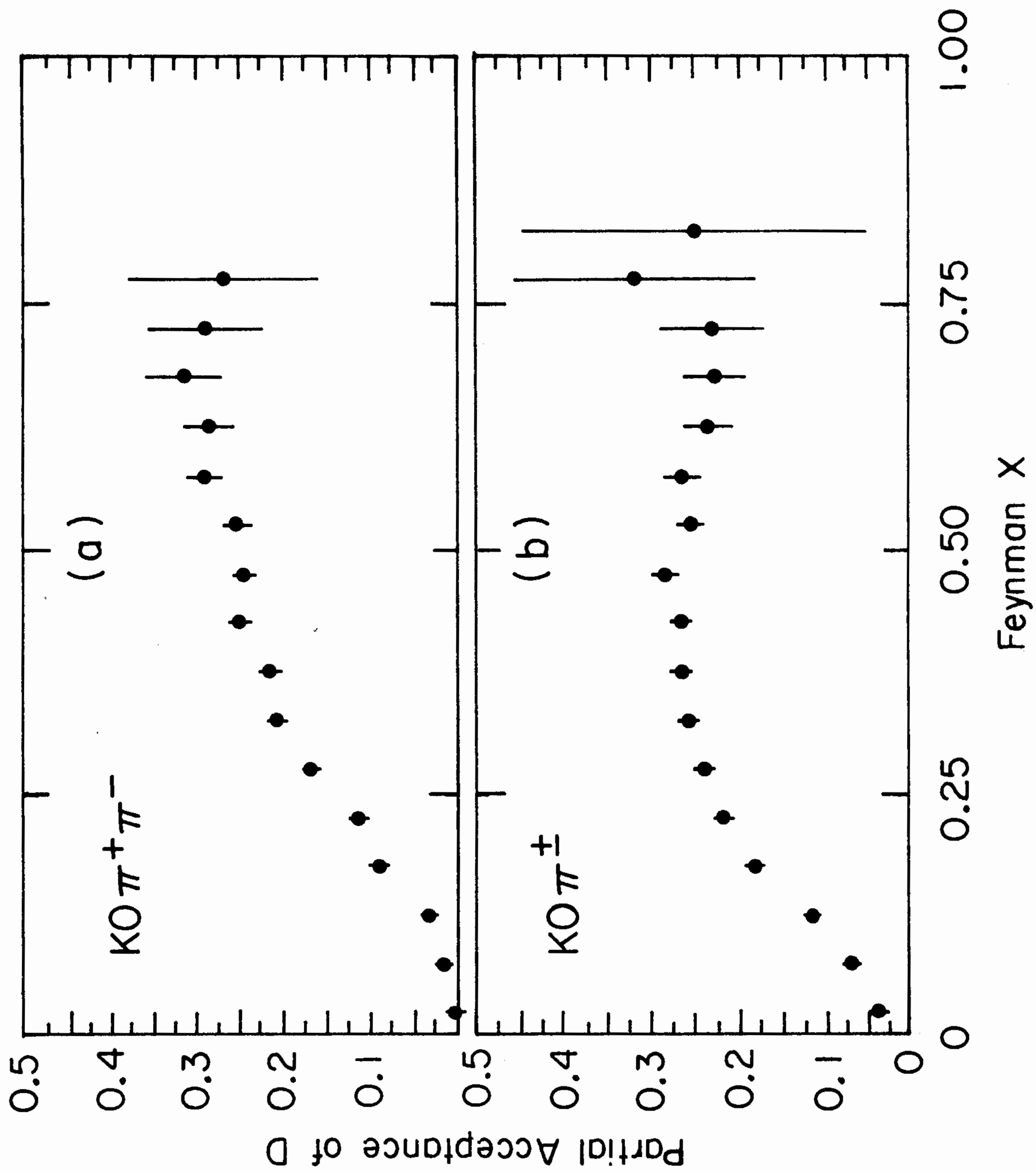
(a)
KOπ+π−
(b)
KOπ±
Partial Acceptance of D
0.5
0.4
0.3
0.2
0.1
0
Feynman X
0
0.25
0.50
0.75
1.00

efficiency and track linking probabilities is shown in Table 6-2 for the $K0\pi^+\pi^-$ decay mode and in Table 6-3 for the $K0\pi^\pm$ decay mode. The fractions shown are obtained by the successive requirements of proton, muon, and K0 acceptance, and are thus correlated. For example, removing the muon requirement would tend to shift the momentum of the D which decays hadronicly upward thus changing the K0 momentum spectrum, and subsequently, the K0 acceptance. As discussed in Chapter 2, recent results indicate different semi-leptonic branching ratios for the D^o and D^+. This result makes the cross section calculation result dependent not only on the Monte Carlo model, but also on the ratio of charged D's to neutral D's in the final state. If the D recoiling against the detected D was neutral, the odds would be in favor of a non-prompt muon trigger, whereas if the recoil D was charged, the opposite would be true. Thus I have calculated the trigger and reconstruction efficiency for the case of a muon trigger from background sources.

The calculation was made by using the above model and releasing the muon requirement. The probability of a background muon trigger was given by the observed trigger rate divided by the rate at which recoil protons were detected. This probability was about 5%. The efficiencies resulting when a prompt muon was not required were shown in the last column of Tables 6-2 and 6-3.

6.2 Sensitivity Calculations

The results of the efficiency calculations for the possible production and decay schemes are listed in Table 6-4. The numbers shown are the sensitivities in microbarns per $D\bar{D}$ event. These are the cross sections which would be necessary to reconstruct one event of the given topology. There are two possible trigger mechanisms for any $D\bar{D}$ event. Thus the total

TABLE 6-2

BREAKDOWN OF ACCEPTANCE FOR K0$\pi^+\pi^-$ DECAY MODE

M_X	PROTON	MUON	K0(ACC)	P·μ·K0	LINKEDπ's	K0(DET)	TOTAL EFF.	NO MUON
4.0	0.183	0.478	0.433	0.038	0.825	0.670	0.0210	0.0362
4.5	0.216	0.432	0.446	0.020	0.810	0.637	0.0214	0.0348
5.0	0.221	0.403	0.406	0.036	0.783	0.585	0.0165	0.0344
5.5	0.229	0.372	0.406	0.035	0.761	0.582	0.0155	0.0306
6.0	0.217	0.355	0.379	0.029	0.726	0.589	0.0124	0.0310
6.5	0.169	0.351	0.365	0.022	0.717	0.533	0.0084	0.0228
7.0	0.087	0.332	0.349	0.010	0.683	0.586	0.0040	0.0095

TABLE 6-3

BREAKDOWN OF ACCEPTANCE FOR K0$\pi^{\pm}$ DECAY MODE

M_X	PROTON	MUON	K0(ACC)	P·μ·K0	LINKEDπ	K0(DET)	TOTAL EFF.	NO MUON
4.0	0.178	0.466	0.402	0.033	0.923	0.765	0.0233	0.0434
4.5	0.212	0.426	0.392	0.035	0.933	0.680	0.0222	0.0497
5.0	0.222	0.378	0.388	0.033	0.924	0.718	0.0219	0.0504
5.5	0.223	0.356	0.387	0.031	0.921	0.655	0.0187	0.0431
6.0	0.216	0.343	0.361	0.027	0.910	0.631	0.0155	0.0407
6.5	0.164	0.330	0.362	0.020	0.902	0.599	0.0108	0.0299
7.0	0.087	0.320	0.338	0.009	0.905	0.589	0.0048	0.0166

TABLE 6-4

SENSITIVITIES FOR DETECTING D^a PRODUCED WITH D^b

D^a	D^b	SENSITIVITY (μb/$D\bar{D}$ event)
$D^{\pm}$	$D^{\mp}$	1.71 ± 0.57
$D^{\pm}$	D^o	3.57 ± 1.21
D^O	D^-	1.03 ± 0.34
D^o	$\bar{D}^o$	2.28 ± 0.75
$D^{\pm}(\mu^{\mp})$	$D^{\mp}$	2.09 ± 0.72

probability of triggering on the production and then reconstructing one of the Ds is the sum of the products of the trigger efficiency times the reconstruction efficiency for each mechanism. I have calculated this probability for each of the possible combinations of detected and recoil Ds.

For example, the probability of detecting a D^0 which decayed into $K0\pi^+\pi^-$ and which was produced in association with a $\overline{D^0}$ is given by:

$$P(D^0\overline{D^0}) = [B(\overline{D^0} \to \mu + X) \times \epsilon_\mu(D^0)] + [P(\mu_B) \times \epsilon(D\ )]$$

The subscript μ on ϵ indicates that a prompt muon was required in the acceptance calculation. $P(\mu_B)$ is the probability of a background muon trigger - 5%. I have factored out the branching ratio of the D^0 into $K0\pi^+\pi^-$, and required that the D^0 decay into $K0\pi^+\pi^-$ with unit probability. The branching ratio will be put into the sensitivity separately. The values of the branching ratios used in the cross section calculations were:

1. $B(D^\pm \to \mu^\pm + X) = 0.21 \pm 0.03$
2. $B(D^0 \to \mu + X) = 0.04$ (90% CL upper limit)
3. $B(D^\pm \to K0\pi^\pm) = 0.019 \pm 0.006$
4. $B(D^0 \to K0\pi^+\pi^-) = 0.039 \pm 0.012$

Finally, the sensitivity was calculated by the formula:

$$\eta = (F \times T \times P \times B(D \to K0m\pi) \times (1/3) \times E)^{-1}$$

where:

1. F is the total flux of beam pions for the data analyzed (1.1×10^{10})
2. T = (40 cm of LH2) x (0.0708 g/cm^3 [density of LH2]) x (6.02×10^{23} protons/gram [Avagadro's number]) = 1.7 /barn

3. Factor of 1/3 for $KO \to KO_S \to \pi^+\pi^-$ ($B(KO_S \to \pi^+\pi^-) = 2/3$)
4. P is the probability of detecting the D with the trigger and the apparatus used
5. E is the cut efficiency

Only the cut on QR for the KO enters into the calculation of E. The other cuts were either taken into account in the Monte Carlo program or necessary to insure a diffractive trigger. The value of E is thus determined by the fraction of KO's which were removed by requiring QR < 1.0. This fraction was found to be 9% thus giving a value of 0.91 for E.

6.3 Cross Section Calculations

Combining the results in Tables 5-3 and 6-4, I have calculated cross sections or limits on cross sections. They were obtained by assuming that all of the events observed (or not observed) were produced in the indicated combinations. The actual cross sections are weighted (unknown weights) averages of the appropriate values.

The results are listed in Table 6-5. The limit on $\sigma(D^+D^-)$ was obtained from the limits on the number of $D^\pm$ produced with an oppositely charged muon. In this case the non-prompt muon will be oppositely charged only 50% of the time on the average. This reduces the total probability P slightly. The limit given of 17.7μb at the 90% CL is about twice the cross section for D^+D^- production calculated by MacKay (MacKay, 1980). The 10 ± 5 possible D^- events yield a cross section of 35.7 ± 21.6μb if the recoil D was neutral. The non-observation of D^+ (< 9 events at the 90% CL) implies an upper limit of 54μb at the 90% confidence level, again if the recoil D was neutral. The 26 ± 8 events consistent with the D^0 imply cross sections of 26.8 ± 12.1μb for

TABLE 6-5

CROSS SECTIONS FOR THE INDICATED ASSUMPTIONS OF $D\bar{D}$ PRODUCTION

D(detected)	D(recoil)	CROSS SECTION (μb; 90% CL upper limits)
$D^{\pm}$	$D^{\mp}$	< 17.7
D^{-}	D^{0}	35.7 ± 21.6
D^{+}	$\overline{D^{0}}$	< 54
D^{0} or $\overline{D^{0}}$	$D^{\mp}$	26.8 ± 12.1
D^{0} or $\overline{D^{0}}$	$\overline{D^{0}}(D^{0})$	59.3 ± 26.7

a $D^{\pm}$ recoiling and 59.3 ± 26.7 μb for a D^{0} recoiling. The actual inclusive D^{0} cross section must be between these two values (including errors).

6.4 Comparison With Other Data

Most of the reports of positive evidence for charm production comes from experiments at higher center of mass energies and proton-proton interactions. However, a few of these experiments report substantial forward production cross sections.

Indirect evidence for charm production comes from several beam dump experiments (Hansl, 1978; Bosetti, 1978; Alibran, 1978). If the observed excess of electron neutrinos is attributed to the semi-leptonic decay of charmed hadrons, cross sections (model dependent) of 30 to 400 μb are obtained.

Drijard et al (Drijard, 1979a) report production of Λ_c^+ charmed baryons in proton-proton collisions. Assuming a uniform Feynman X dependence for the cross section, they calculated $\sigma(\Lambda_c^+)B(\Lambda_c^+ \to pK^-\pi^+) \simeq \sigma(\Lambda_c^+)B(\Lambda_c^+ \to \Delta^{++}K^-) \simeq 3$ μb. They also state with large uncertainties a cross section of 60-200 μb for $D^{\pm}$ production (Drijard, 1979b). The $D^{\pm}$ data was also consistent with a flat X_F and P_T cross section dependence.

Giboni et al (Giboni, 1979) looked at the diffractive process $P+P \to P+X^+$. Their results were obtained by calculating the acceptance with a parametrization of the diffractive process as I have done. They obtained $\sigma B(\Lambda_c^+ \to pK^-\pi^+) \simeq 0.7\text{-}1.8$ μb and $\sigma B(\Lambda_c^+ \to \Lambda^0\pi^+\pi^-\pi^+) \simeq 0.3\text{-}0.7$ μb. These values are consistent with those of Lockman et al (Lockman, 1979) who also report evidence for the diffractive production of the Λ_c^+ in the interval $0.75 < X_F < 0.90$ with $\sigma B(\Lambda_c^+ \to pK^-\pi^+) = 2.8 \pm 1.0$ μb and $\sigma B(\Lambda_c^+ \to \Lambda^0\pi^+\pi^-\pi^+) = 2.3 \pm 0.3$ μb.

A recent estimate (Abrams, 1980) of $B(\Lambda_c^+ \to pK^-\pi^+)$ is 0.022 ± 0.010. This value implies total cross sections (in the appropriate kinematic regions) of 40-150 μb for the observations above.

Thus there are several reports of charm production either produced in diffractive interactions or consistent with a diffractive production mechanism. The differing experimental conditions and kinematic regions (not to mention the model dependence) make a direct comparison to my results difficult. Neither the energy dependence of the cross sections or their dependence on the incident hadron is known. More and better experiments will be needed before the hadronic production of charm is understood. There is at least now some data to help in the design of the second generation experiments.

CHAPTER 7

CONCLUSIONS

A total of 26 ± 8 events have been observed which are consistent with the production and subsequent decay of the D^0 charmed meson through its $K0\pi^+\pi^-$ channel. The cross section implied by this number of events depends on the species of the recoiling D. The extreme hypotheses that either all production occurs via D^0D^- or all production occurs via $D^0\overline{D}^0$ lead to cross sections of 26.8 ± 12.1 and 59.3 ± 26.7 μb. The actual cross section must lie between these limits. I find in addition that the inclusive D^+D^- production cross section is smaller than 17.7 μb at the 90% confidence level. Assuming that the 10 ± 5 events consistent with the D^- are real, I calculate a cross section for inclusive D^-D^0 production of 35.7 ± 21.6 μb. The non-observation of a D^+ signal implies that the $D^+\overline{D}^0$ cross section is less than 54 μb at the 90% CL.

REFERENCES

Abrams, G. S., et al., Phys. Rev. Lett. 44, 10, (1980)

Alibran, P., et al., Phys. Lett. 74B, 134, (1978)

Alverson, G. O., thesis, University of Illinois, 1979.

Antipov, Y. M., et al., Nucl. Phys. B63, 182, (1973)

Ascoli, G. et al., "Search for Charmed Particles Revised Proposal 369", (October ,1975).

Aubert, J. J., et al., Phys. Rev. Lett. 33, 1404, (1974)

Augustin, J.-E., et al., Phys. Rev. Lett. 33, 1406, (1974)

Bacino, W., et al., Phys. Rev. Lett. 45, 329, (1980)

Bander, M. et al., Phys. Rev. Lett. 44 , 7, (1980).

Barish, S. J., et al., Phys. Rev. Lett. 31, 1080, (1973)

Barger, V., and R. J. N. Phillips, Phys. Rev. D12, 2623, (1975)

Bjorken, B. J., and S. L. Glashow, Phys. Lett. 11, 225, (1964)

Bosetti, P. C., et al., Phys. Lett. 74B, 143, (1978)

Carlson, S. E. and R. Suaya, Phys. Rev. D17, 760, (1978).

Drijard, D. et al., Phys. Lett. 85B, 452, (1979a).

Drijard, D. et al., Phys. Lett. 81B, 250, (1979b).

Giboni, K. L. et al., Phys. Lett. 85B, 437, (1979).

Glashow, S. L., J. Iliopoulous, and L. Maiani, Phys. Rev. D2, 1285, (1970)

Gustafson, G. and C. Peterson, Phys. Lett., 67B, 81, (1977).

Hansl, T., et al., Phys. Lett. 74B, 139, (1978)

Hicks, R. G., thesis, University of Illinois, 1978.

Jones, L. M. and H. W. Wyld, Phys. Rev. D17, 1782, (1978).

Lockman, W. et al., Phys. Lett. 85B, 443, (1979).

MacKay, W. W., Thesis, University of Illinois, 1980

Perruzzi, I., et al., Phys. Rev. Lett. 37, 569, (1976) Pordes, S., thesis, Harvard University, 1976.

Proudfoot, J., Thesis, University of Oxford, 1978

Rosen, S. P., Phys. Rev. Lett., 44 , 4, (1980).

Roy, P., Theory of Lepton-Hadron Processes at High Energies, Oxford, 1975.

Smith, E. B., Thesis (unpublished), University of Illinois

Trilling, G., Talk at XX International Conference on High Energy Physics, Madison, Wisconsin, 1980

APPENDIX

LEAD GLASS DATA ANALYSIS

This appendix covers the details of the Lead Glass Cerenkov counter array. The main areas covered are:

1. Lead glass calibration system
2. Lead glass energy calibration with positrons
3. Lead glass data analysis and results

The mechanical description of the array and counters can be found in section 3.4.

A.1 Lead Glass Calibration System

The energy calibration monitoring system used for the lead glass Cerenkov counter array consisted of a stable high voltage mercury reed pulse generator, a charging line , a clipping line, a high frequency passive distribution network, and LEDs (light emitting diodes) mounted on the individual counters. Figure A-1 shows this system schematically, as well as the logic to provide the ADC (analog-to-digital converter) gate signals. At the array, the high voltage pulse was passively divided into 128 signals, of which 80 were used to drive the LEDs. One signal was returned to the electronics where it was attenuated and used to trigger the gate generator for the ADCs. This signal was also digitized with the PMT (photomultiplier tube) anode signals as a check on the stability of the high voltage reed pulser.

A complete calibration consisted of 100 pulses taken at each of 5 different high voltage settings (actually 0 volts for pedestals and 4 non-zero voltages). The ADC data for each pulse was written on Dec-tape by

Figure A-1. Schematic diagram of LED pulser system.

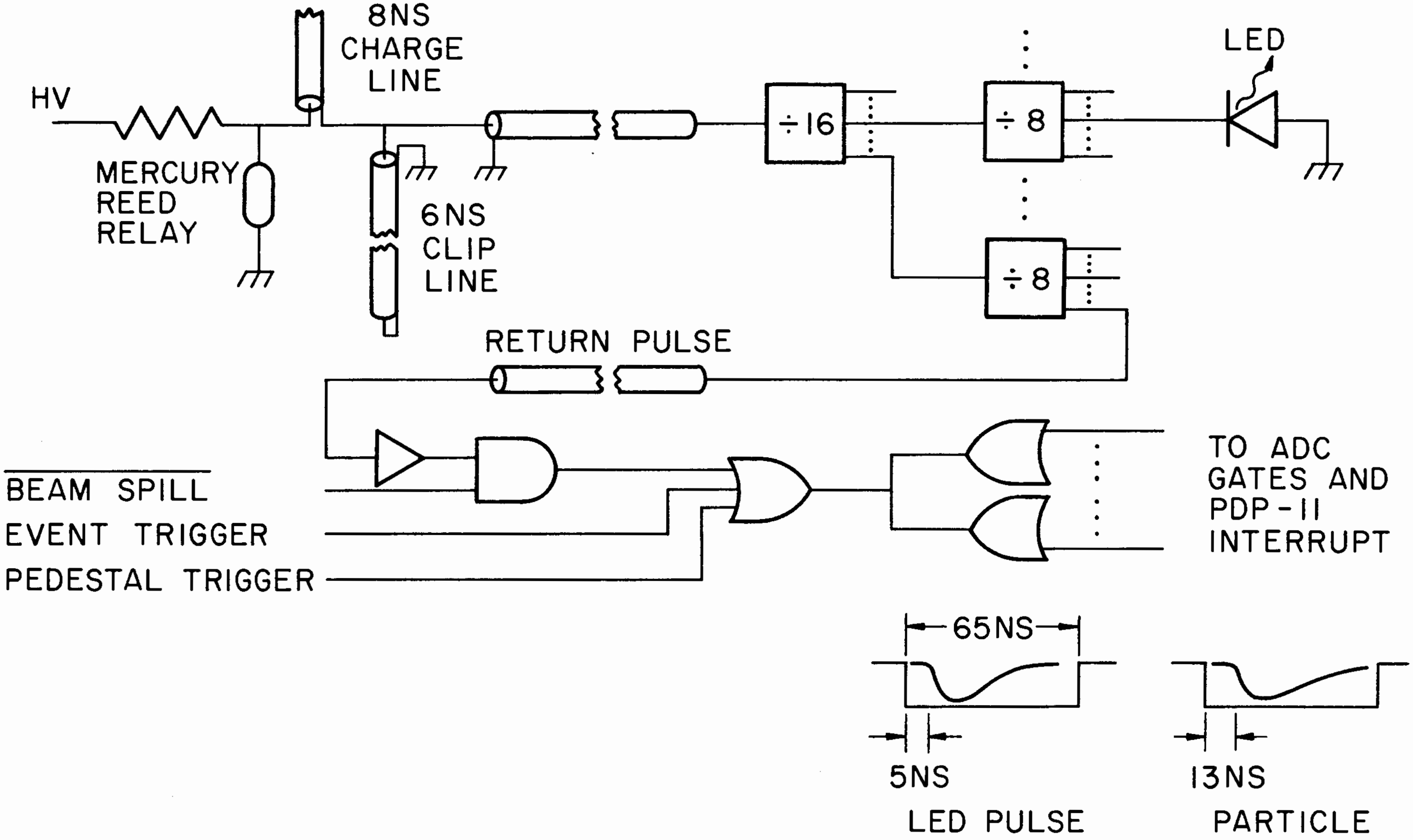
HV
MERCURY
REED
RELAY
8NS
CHARGE
LINE
6NS
CLIP
LINE
÷16
÷8
÷8
LED
RETURN PULSE
BEAM SPILL
EVENT TRIGGER
PEDESTAL TRIGGER
TO ADC
GATES AND
PDP-11
INTERRUPT
65NS
5NS
LED PULSE
13NS
PARTICLE

the PDP-11 on-line computer dedicated to the lead glass array. The ADC pulse heights were also averaged for each counter and voltage. These could then be compared to the nominal values stored on the computer and the differences displayed. The averaged pedestals and pulse heights corresponding to the maximum pulser voltage were then sent to the XDS Sigma-3 main on-line computer for inclusion in the begin run records.

The short term stability of the pulser was excellent. The typical pulse varied by less than 0.5% from the average. Figures A-2(a) and (b) illustrate the long term stability of the lead glass system. The relative gain of several counters is shown as a function of time. The gains are relative to those at time 0 on the plots (not time 0 of the experiment). The two counters shown in Figure A-2(a) are adjacent counters in the array. The gains usually tended to change in the same relative direction, since most changes were caused by temperature variations or beam intensity variations. Figure A-2(b) shows the gain change for two counters near the beam line. The increase in gain is due to the decrease in LED pulse height caused by the yellowing of the lead glass (see section A.3.5). The pulse height from the counter directly in the pion beam had decreased to zero by the middle of the experiment.

The PMT high voltages were also recorded during the calibration sequence. They were read directly by the PDP-11 through a multiplexer and digital voltmeter. As with the ADC pulse heights, the high voltages were compared to the desired values and adjusted if necessary.

By attenuating the PMT anode signals and decreasing the PMT high voltage, the energy at which majority of the ADCs overflowed was increased to approximately 30 Gev. The counters were originally used for detecting photons up to about 5 Gev (Shupe, 1976).

Figure A-2. Relative gain changes as a function of time. Two adjacent counters away from the beam line are shown in (a), while two counters near the beam line are shown in (b).

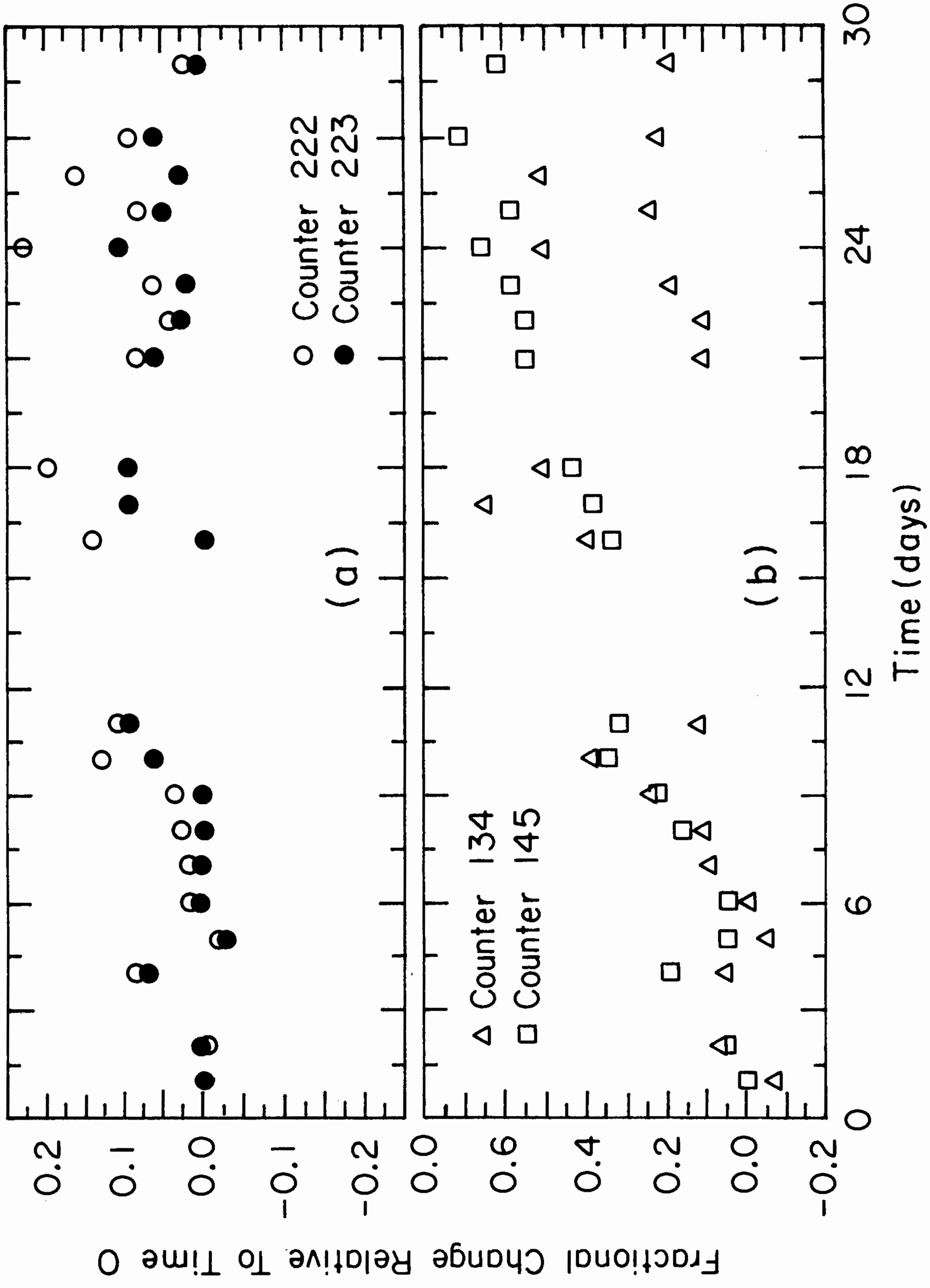
(a)
○ Counter 222
● Counter 223
(b)
△ Counter 134
□ Counter 145
Fractional Change Relative To Time 0
0.2
0.1
0.0
-0.1
-0.2
0.8
0.6
0.4
0.2
0.0
-0.2
0
6
12
18
24
30
Time (days)

A.2 Energy Calibration with Positrons

In addition to proper monitoring of the PMT gains, an absolute energy calibration must be done at some time. It would have been preferable to perform such calibrations regularly during the data logging. There were, however, no facilities for producing an electron beam in the Muon Lab at that time. Consequently, it was necessary to move the lead glass array to an experimental area in Proton West to do the electron calibration. Since the experiment which had just finished (FNAL E95) had used lead glass arrays, there existed the necessary apparatus for the calibration process. Extreme care was taken to reproduce the conditions under which the data was taken. Signal cables were adjusted to the same length and the same pulser cable was used. However, there was no means to reproduce the conditions of the CCM fringe field or the effects of an intense pion beam.

A schematic diagram of the calibration set-up is shown in Figure A-3. Positrons were produced by converting the photons from neutral pion decay into e e pairs and selecting out the positive particles of the correct energy with bending magnets. The beam production apparatus is not shown. Two modules of MWPCs recorded the positron trajectories, while the scintillation counters provided the event trigger. Since the MWPCs were near the face of the array, and the positrons were incident perpendicularly, a very simple trackfinding algorithm was sufficient.

Although it was possible to steer the positron beam in both transverse directions, the range of movement was limited to about a 10 cm radius. Therefore, it was deemed more practical to place the array on a hydraulically operated lift table (shown in the inset in Figure A-3) to achieve the necessary vertical positioning. The lift table was, in turn, placed on a track so that the array could be moved horizontally, although

Figure A-3. Schematic diagram of calibration apparatus. Positron beam is produced upstream and enters from left through beam pipe. The scintillation counters provided the trigger signal, and the MWPCs recorded the particle´s impact position.

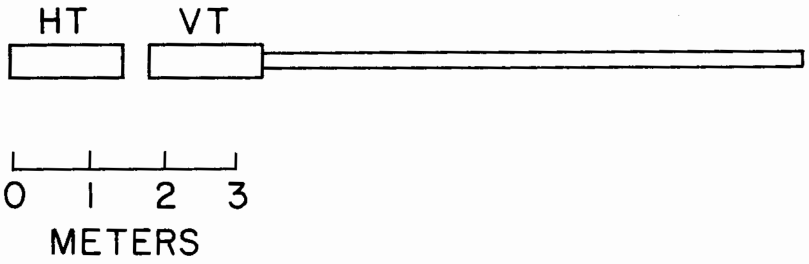

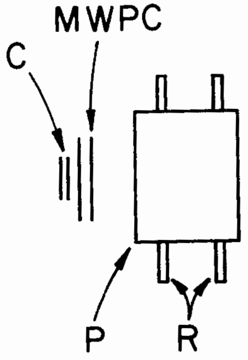

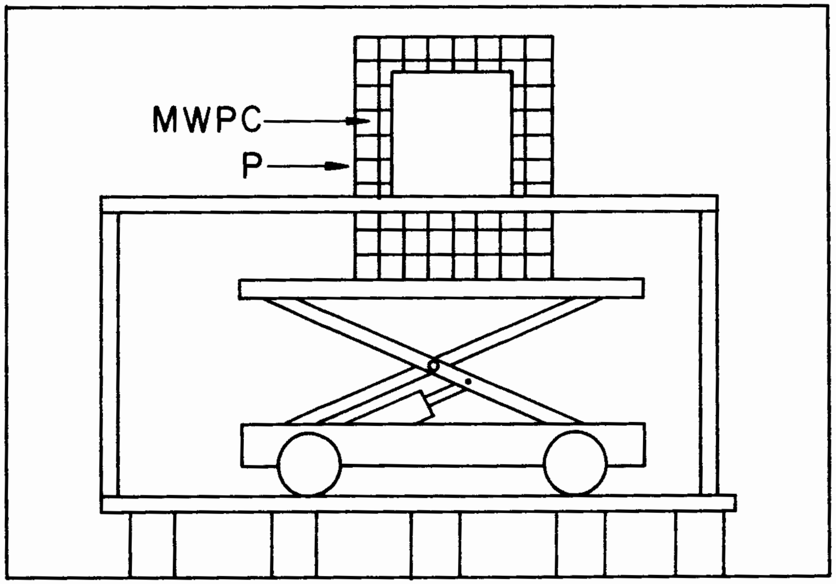

HT	HORIZONTAL TRIM MAGNET
VT	VERTICAL TRIM MAGNET
C	TRIGGER SCINTILLATION COUNTERS
MWPC	32 x 32 cm X,Y AND U,V (±45° TILT)
R	RAILS FOR HORIZONTAL POSITIONING
P	LEAD GLASS ARRAY

most of the horizontal positioning was done by the beam steering magnets. The vertical position of the table could be adjusted from within the Port-a-kamp to within 0.5 mm of the desired position with a closed-circuit television camera which was focussed on a meter scale and pointer arrangement. Using this procedure for positioning the array in the beam, the entire array was calibrated with only one access to the experimental area to move the table horizontally (however, many accesses were required to debug and repair various pieces of the apparatus).

Since lead glass had also been used in E95, the task of acquiring the data was relatively straightforward. The profiles of the beam were monitored and adjusted by means of histograms of the wires hit. The cracks between the lead glass counters were located with scatter plots of the pulse height in one versus the pulse height in the adjacent counter. A typical set of beam profiles is shown in Figure A-4.

Since the calibration of each column of counters required only two hours of beam , LED pulser calibrations were normally done once per column. About 5000 triggers were recorded for each counter. However, not all triggers were from positrons. Depending on the beam quality, up to 80% of the triggers were caused by muons in the beam, or by positrons hitting other counters. Figure A-5(a) shows the pulse height distributions (ADC pedestals have been subtracted) obtained from a good counter (222) at nominal beam energies of 15.5 and 24 Gev. Figure A-6 shows the corresponding results for a yellowed counter (134) at 15.5 Gev. Note the double peaks from minimum ionizing muons. The second peak stems from muons which pass through the lead glass light pipe as well as the counter. Each counter in the array was calibrated with 15.5 Gev positrons. In addition, about 30 counters were calibrated at 24 Gev and 14 counters at 8 Gev. A

Figure A-4. Profiles of the positron beam for Y (a) and X (b). The abscissa is the number of the wire recording a hit.

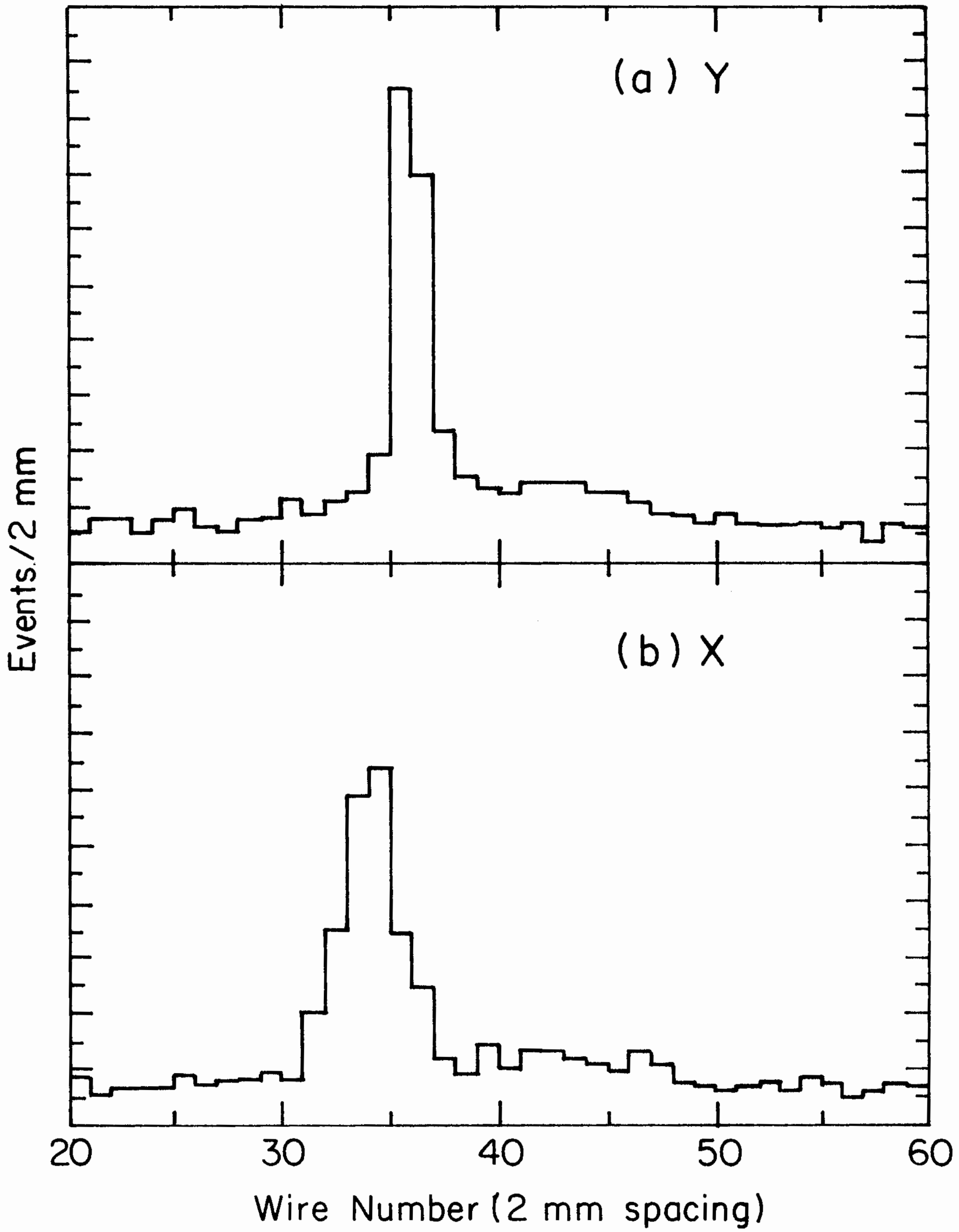
(a) Y
(b) X
Events/2 mm
20
30
40
50
60
Wire Number (2 mm spacing)

Figure A-5. Pulse height distribution resulting from positrons 15.5 and 24.0 Gev positrons for a non-yellowed counter. This counter was located in the third row from the top and the third column from the left in Figure A-1.

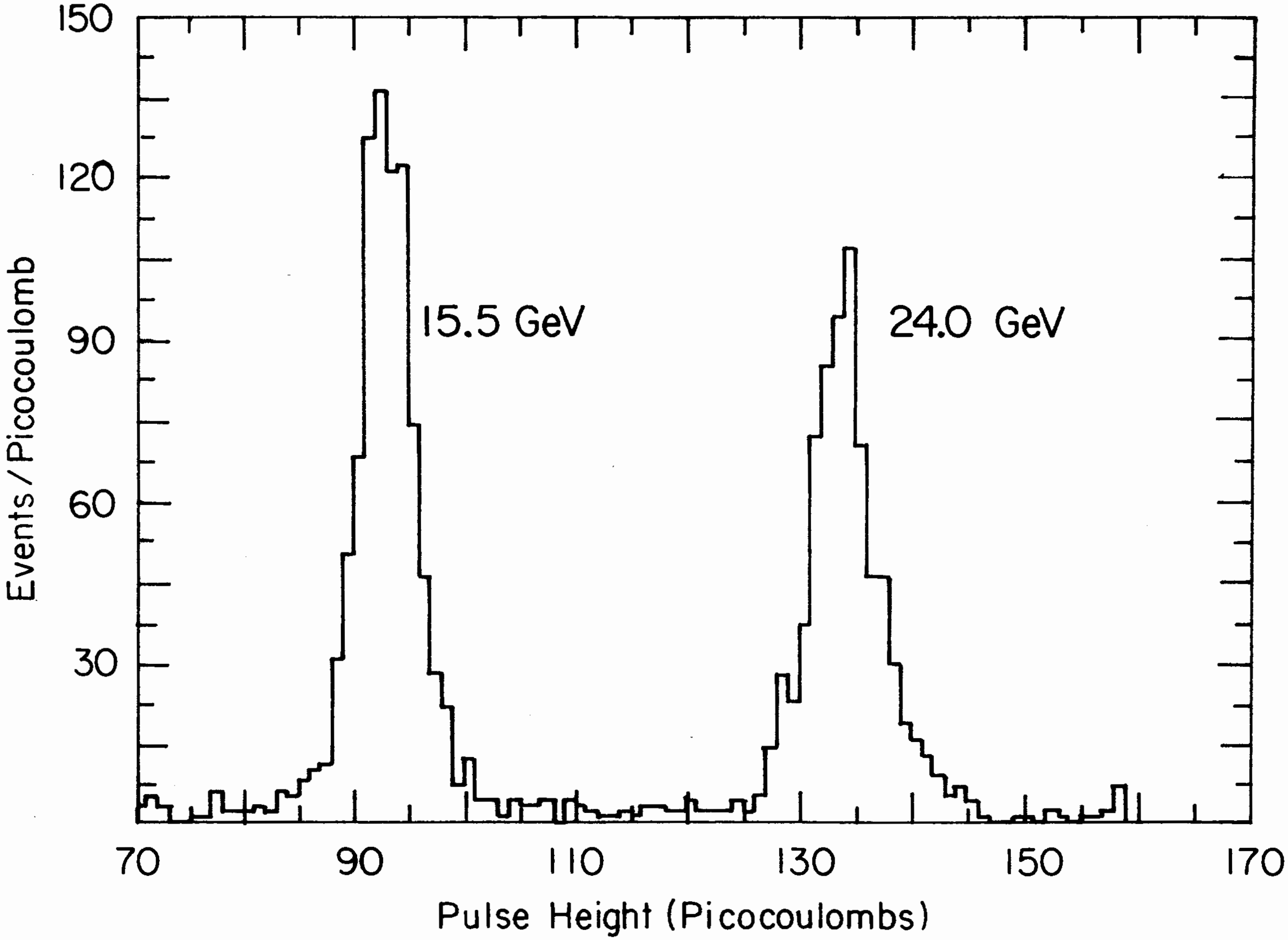
150
120
90
60
30
Events / Picocoulomb
15.5 GeV
24.0 GeV
70
90
110
130
150
170
Pulse Height (Picocoulombs)

Figure A-6. Pulse height distribution resulting from 15.5 Gev positrons for a yellowed counter. This counter was located in the fifth row from the top and the sixth column from the left in Figure 3-10.

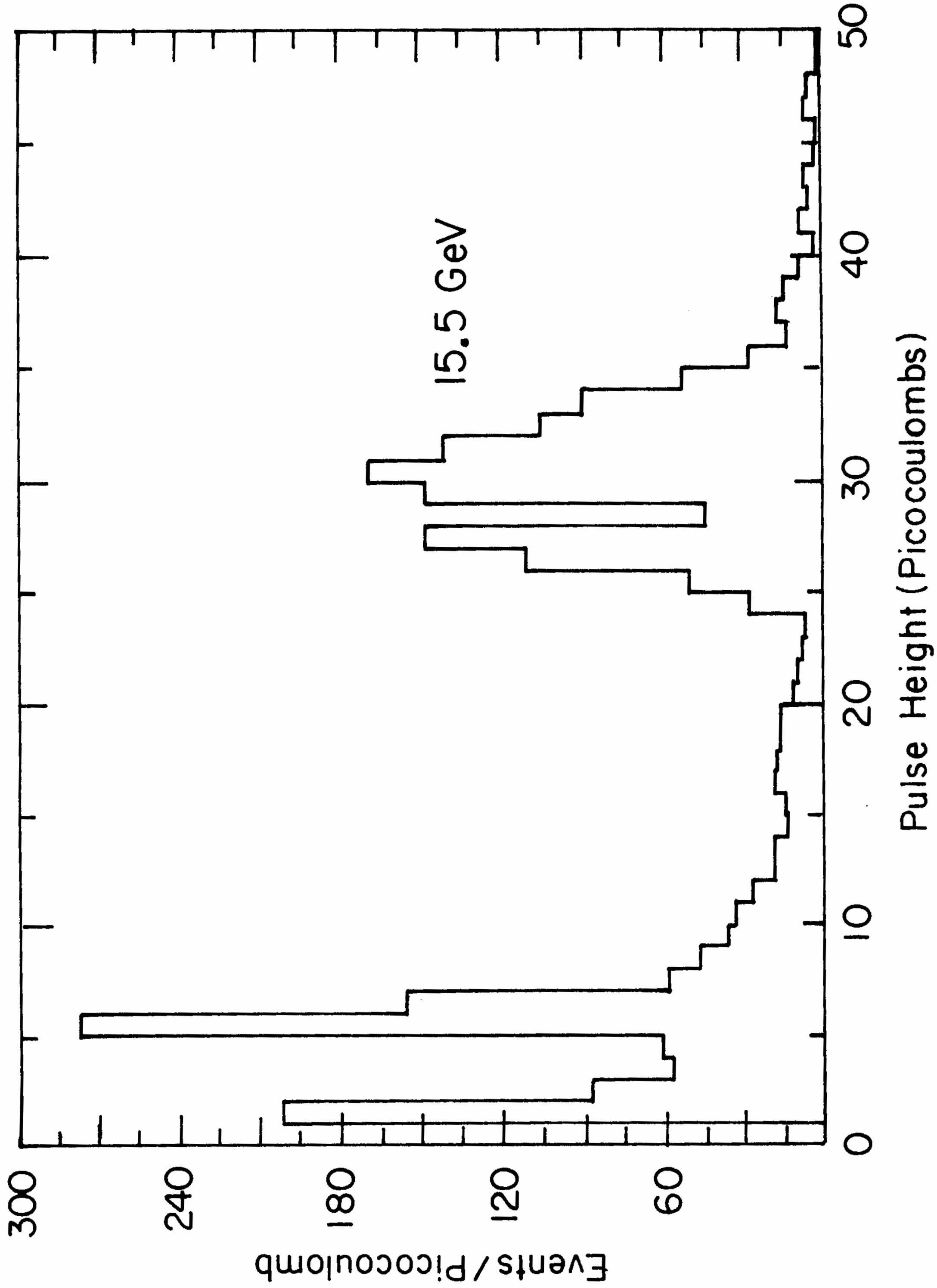
15.5 GeV
Events / Picocoulomb
300
240
180
120
60
Pulse Height (Picocoulombs)
0
10
20
30
40
50

few of the yellowed counters were also studied at 30 Gev.

Due to a lack of running time and problems with poor beam quality, an insufficient number of counters were calibrated at several energies. As a result, a linearity curve is not shown. The few counters which were calibrated at more than one energy were either yellow or on the edge of the array or both. In addition, the MWPCs were uselessly inefficient for a few of the later runs.

The second phase of the calibration procedure involved an iterative adjustment of the gains so that the average total shower energy (see section A.3.1 for a definition of the total shower energy) was equal to the nominal beam energy. Gain, as used here, is the number which converts the ADC pulse height in picocoulombs to energy deposited. Of course, the initial gain is given by:

$$GO = \text{Beam Energy}/\langle\text{net charge}\rangle$$

In computing the average charge, only events were taken in which a single track was found in the MWPCs within 8 mm of the peak in the beam profile for that counter.

Since the energy leakage from the central counter averages 10% with the beam approximately centered, the following algorithm was used to derive the actual gain of the counters.

In all energy calculations, the gains of the surrounding 8 counters were assumed to be correct. Thus, the energy actually deposited in the central counter was calculated as:

$$E(\text{central}) = \text{Beam energy} - \text{Energy in surrounding counters}$$

and the corrected gain was given by:

$$G' = \langle E(\text{central})/\text{net charge}\rangle$$

The nominal beam energy was reduced by 3% for calculations involving counters on the edge of the array to compensate for undetected leakage.

This process was iterated by applying the correction to each counter sequentially, and then using the corrected gains on the subsequent iteration. The process was terminated when all gains had stabilized to better than 1%. The total shower energy distributions corresponding to the pulse height distributions shown in Figure A-5 are shown in Figure A-7.

Before the calibration results could be tested (by looking for a peak in the di-gamma invariant mass spectrum at the mass of the neutral pion, for example), one additional correction had to be made. This correction dealt not with the gains per se but with the LED pulser calibrations. As stated in section A.1, a clip line was normally used on the output of the charging line to limit the pulse width. Toward the end of the experiment, as several of the counters were becoming yellow, it was deemed necessary to remove the clip line to effectively increase the LED pulse height. When this was done, several before and after calibrations were done to measure the change for each counter. This factor had to be included if the data to be analyzed was taken with the clip line installed, since the positron calibration data was taken without the clip line. All other changes of any kind were hopefully taken into account by the LED pulser calibrations.

The way in which the gains were modified using the LED calibrations is next descibed. The idea is that the constant light output from the LED corresponds to an electromagnetic shower of a fixed energy. When the LED calibration is performed, the pulse height from each counter corresponds to a known energy. The gain of the counter is then adjusted so as to give this predetermined energy. For example, assume that a counter gave a pulse height of 100 picocoulombs when it was calibrated with positrons. Assume also that the pulse height from 15 Gev positrons was also 100 pc. Thus the

Figure A-7. Total shower energy distribution corresponding to the pulse height distributions in Figure A-5. This includes the energy which leaked out of the counter being calibrated. The gains were adjusted to reproduce the 15.5 Gev beam energy.

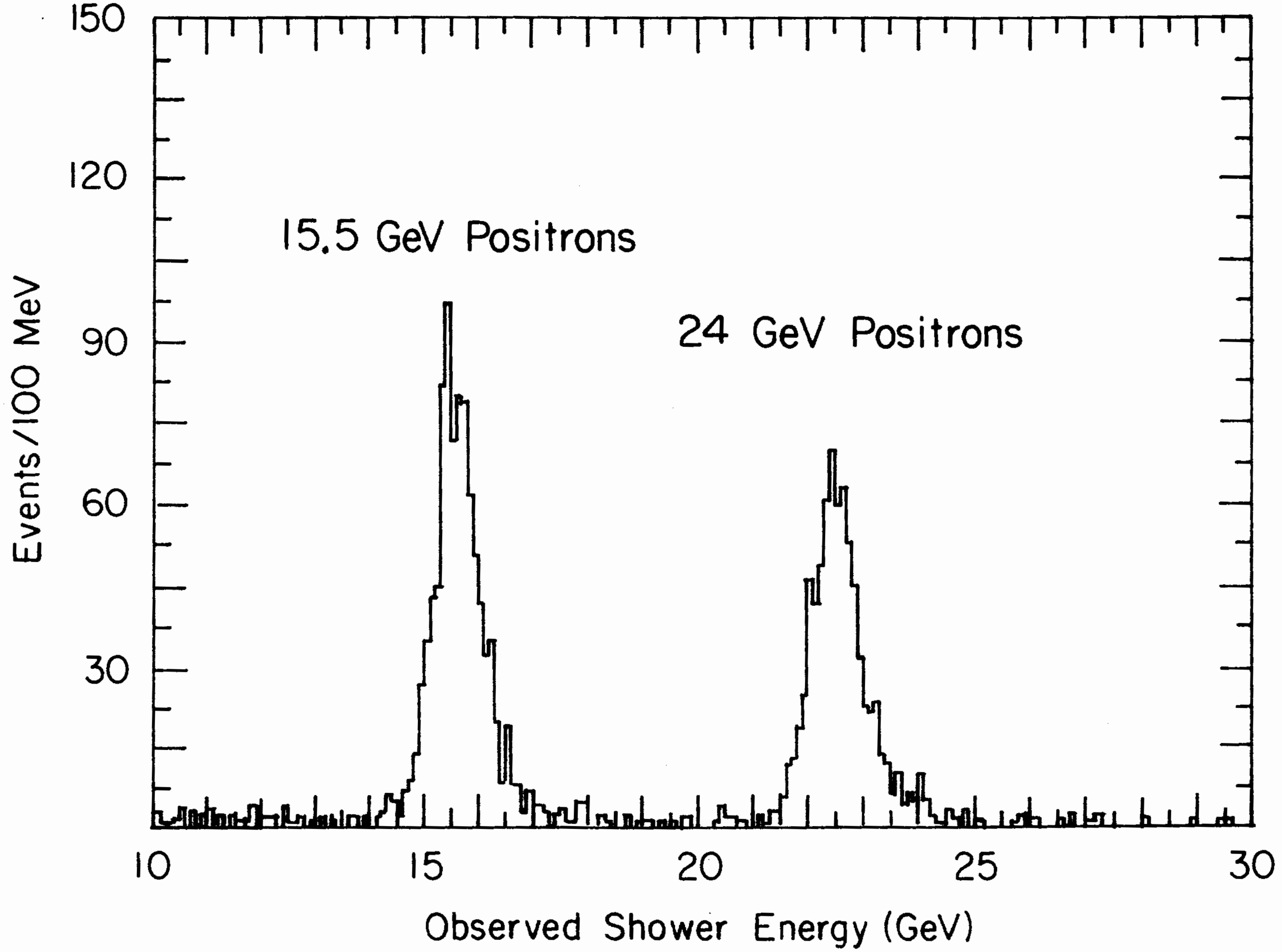
150
120
90
60
30
Events/100 MeV
15.5 GeV Positrons
24 GeV Positrons
10
15
20
25
30
Observed Shower Energy (GeV)

LED flash is the equivalent of a 15 Gev positron. If the gain of this counter was determined to be 150 Mev/pc (15 Gev/100 pc) when it was calibrated, and at some other time the LED flash gave 50 pc, the corrected gain would be 15 Gev/50 pc or 300 Mev/pc. Thus the gain is inversely proportional to the LED pulse height.

A.3 Lead Glass Data Analysis

This section describes the basic algorithms used for the various parts of the lead glass data analysis, and some of the basic results and difficulties which arose. The particular topics covered are:

1. Shower finding
2. Impact position calculation
3. Shower classification and hadron rejection
4. Effects of beam

A.3.1 Shower Finding

It is first necessary to define what is meant by a shower in the lead glass array. In the most general sense, a shower can be defined as a cluster of adjacent counters containing pulse height. As it is defined here however, a shower is restricted to a 3 x 3 counter sub-array. Thus only energy which is deposited in the 9 counters in the sub-array is totaled. Any energy which may have leaked out of the sub-array is disregarded. The reason for this restriction is two-fold: 1) it somewhat simplifies the analysis to fix the definition of the shower, and 2) it loses very little energy in a genuine electromagnetic shower. Only about 10% of the total shower energy is found outside the central counter when the initiating particle strikes the center of the counter. In the worst case, when the photon strikes very near a corner of the counter, much less than 10% of the energy will find it way more than one counter's width in any direction.

Showers are located by the following procedure. The energy in each counter is compared to a value which is set to 20% of the desired low energy cut-off (usually in the 1-5 Gev range). This allows most counters to be skipped, while at the same time, it guarantees that a shower having the minimum desired energy will not be missed. This statement results from the observation that, in the worst case (as discussed above), approximately 25% of the energy should be deposited in each of 4 counters, while in any other case the center counter should contain more than 25% of the total energy.

Once a counter with sufficient energy is found, the central counter of the shower is located. This is done simply by examining the energy in each of the 8 surrounding counters and moving to the center of the one with the largest energy deposition. The central counter is considered to be located when no adjacent counter contains more energy. The total energy is then summed from the 9 counters in the shower, and compared to the low energy cut. If it passes the energy cut, the newly found shower is compared to all previously found showers to make sure it is indeed a new shower.

Two types of showers tend to be improperly treated by this shower finding algorithm: 1) largely overlapping showers, and 2) showers in which the central counter is dead. Showers which overlap enough that there is no counter separating the central counters will not be resolved. The two showers will be identified as a single shower. In the case where a dead counter occupies the central shower region, it is possible for two separate showers to be found - one on either side of the dead counter. This can happen only if the leakage in opposite directions is greater than the low energy cut. Both of these pathological conditions could have been alleviated to some extent by a sophisticated energy fitting algorithm. By fitting the energy distribution in the tails of the shower to the known distributions as a function of energy and impact position, both the energy and position can be determined to some extent even in these cases. For the present analysis however, cases of overlapping showers usually was an indication of photons from the decay of a high energy neutral pion (π^0), and since π^0 energies high enough to cause overlapping showers were also high enough to cause ADC overflows, these events were typically of little interest.

All showers were checked for various conditions:

1. ADC overflow
2. Central counter on edge of array
3. Dead counter(s) in shower
4. Yellow counter(s) in shower
5. Energy sharing with another shower

The overflow of an ADC was considered a fatal condition, which meant the shower was not used in any analysis. All of the other problems were flagged, while, in the case of energy sharing, an attempt was made to separate the energies. Sharing of energy between showers occurred just before the showers became unresolvable. The approach used to separate the energies was to evaluate the amount of energy leakage in each shower in the direction opposite to the shared region. Each shower was categorized in terms of whether more or less than 5% of its energy was found in the counters opposite the shared region. If both showers were in the same category, the energy was divided according to the ratios of the energies in the showers. If the showers were in different categories, the energy was divided 80%-20% or 90%-10% depending on the particular configuration with the shower having the least energy in the opposite direction receiving the bigger share.

This method could be improved upon considerably, but seemed to help somewhat in the usual case where the shared energy was a small fraction of the total. At the least, the shared energy was not added into the total energy for both showers.

A.3.2 Position Calculation

The next calculation done was that of the impact position of the shower-inducing particle. There are several possible approaches to this problem. One method involves fitting the energy distribution observed to a series of tabulated distributions corresponding to small increments in position. The impact position is taken to be that position which gives the best "fit". This algorithm has both advantages and disadvantages (as does any). The advantages include possibly improved resolution, and the ability to estimate the energy deposited in inoperative counters. Increased computation time is the major drawback.

For the present purposes, a simpler scheme was thought to be adequate. The particular paramterization used was developed after studying the energy sharing characteristics of Monte Carlo generated showers. The transverse development of the shower was generated according to the results of a Monte Carlo study of electromagnetic showers in lead glass.(Longo, 1973)

The parameterization which gave the most nearly linear relationship between the position and the functional value was the following:

$$P = \mathrm{LOG}\left[(1 + \mathrm{Ecent}/\mathrm{Eout})/2\right]$$

Ecent is the total energy deposited in the center column (row for Y) of the 3 X 3 sub-array. Eout is the larger of the energies deposited in the two outer columns (or rows, for the Y calculation) of the 3 X 3 sub-array. The center of gravity of the shower is taken to be between the mid-point of the central counter and the edge nearer to the column with energy Eout. The function P has the property of vanishing when Eout equals Ecent, which occurs when the shower is centered on the crack between the counters. Thus P increases as the impact position moves inward from the edge. The relationship (for several different determinations) between the distance of the impact position from the edge of the counter and the value of P is shown in Figure A-8. The value of P is calculated for X and Y independently, and the impact position is interpolated from a piece-wise linear approximation to the curve (between the points).

The curve labeled ´Monte Carlo´ was derived from the study mentioned above. The curve labeled ´Electron´ was obtained from the positron calibration data. Since the impact position was known from the MWPCs, it was easy to determine the relationship shown. However, it was immediately evident that the curve derived from the positron data was incompatible with the experimental data from the fact that the impact positions calculated with the curve were not uniform over the counter as they obviously should be. The reason for this is unclear but may result from the relatively poor statistics (i.e., small number of events per point) in the positron study, or from the energy dependence of the transverse shower development. (Energy leakage decreases as incident energy increases, so that a lower energy shower will seem to be located nearer the edge than a higher energy shower hitting the same spot.) This non-uniformity is shown in Figure A-9 which is a histogram of the x values of the impact positions calculated

Figure A-8. Parametrization used for impact position calculation. The abscissa represents the distance of impact from the edge of the counter and the ordinate is the corresponding value of the function P.

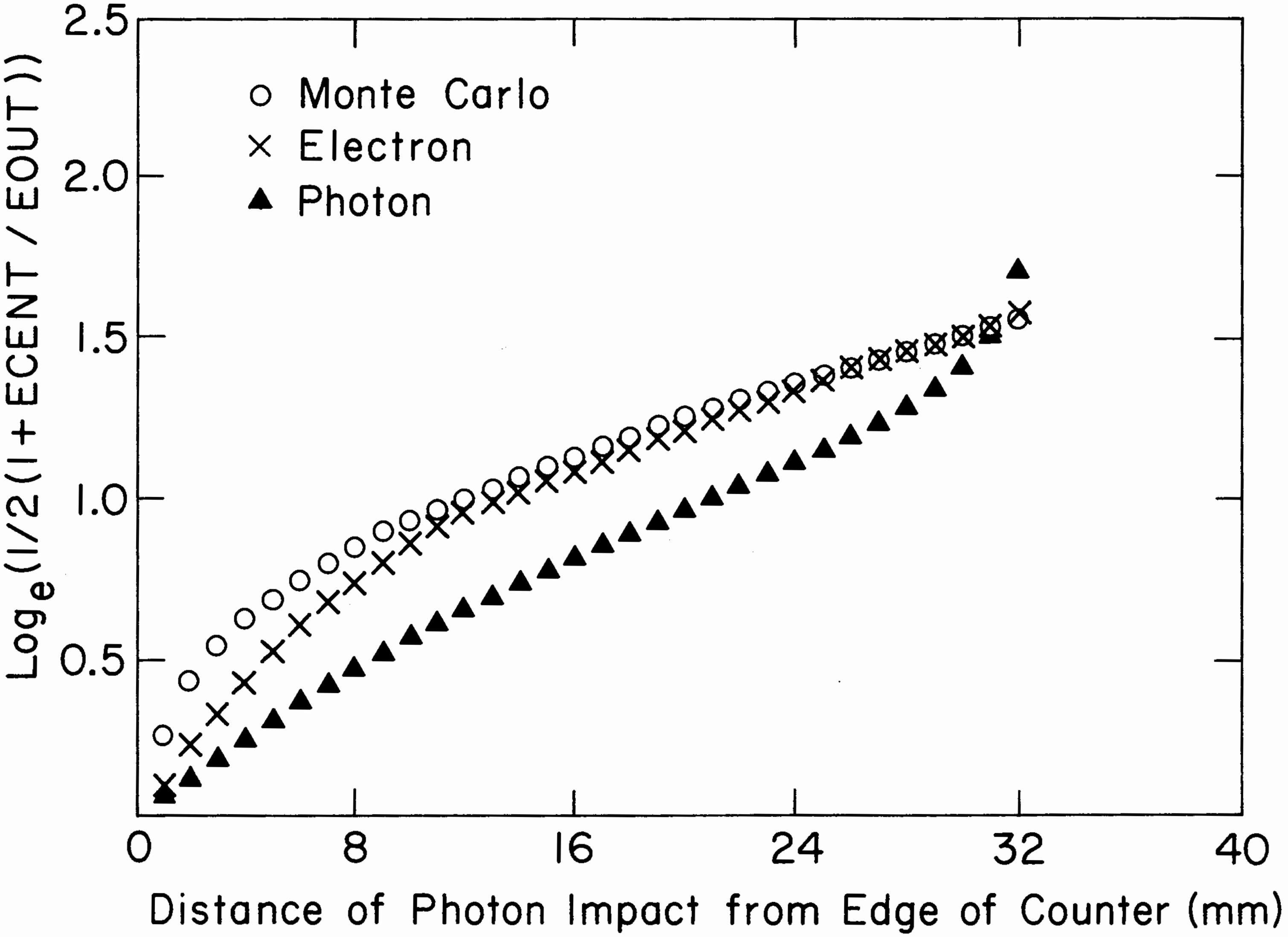

○ Monte Carlo
× Electron
▲ Photon
Log$_e$(1/2(1+ECENT / EOUT))
2.5
2.0
1.5
1.0
0.5
0
8
16
24
32
40
Distance of Photon Impact from Edge of Counter (mm)

Figure A-9. Projection of calculated impact positions onto X axis. The solid histogram was obtained by using the ´Electron Data´ curve from Figure A-8. The dashed histogram results from the ´Photon Data´ curve.

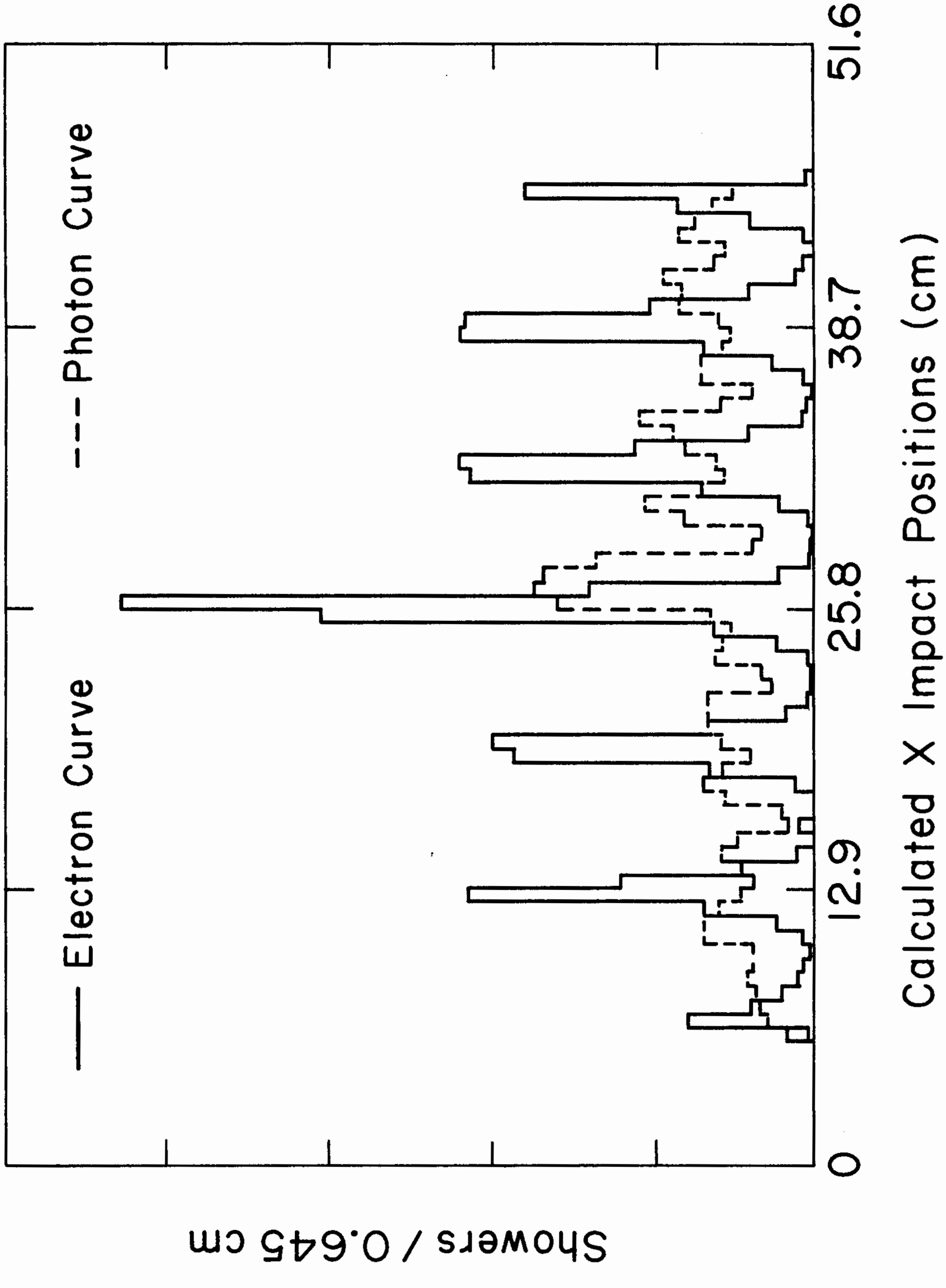
— Electron Curve
--- Photon Curve
0
12.9
25.8
38.7
51.6
Calculated X Impact Positions (cm)
Showers / 0.645 cm

with the ´Electron Data´ curve in Figure A-8. The tedency for the impact position to be found near the edge (tic marks are locations of counter edges) of the counter is clearly seen.

The curve in Figure A-8 labeled ´Photon´ was derived in an attempt to make the distribution of impact positions more uniform. The two assumptions that went into this derivation were that 1) hadronic interactions did not affect the validity of the derivation, and 2) the distribution of impact positions within a given counter should be uniform in x and y. The procedure then was to histogram the values of the function P for all showers (separately in X and Y, although no significant differences were noted). This histogram (X and Y taken together) was divided into 32 bins of equal population (32 is approximately the number of millimeters in a counters half-width). The curve was generated by plotting the bin number (i.e., millimeters from the edge of the counter) versus the value at the upper edge of the bin. This curve was used for the calculation of impact positions for the experimental data. A typical X projection of impact positions calculated with the ´Photon Data´ curve is shown dashed in Figure A-9.

A.3.3 Shower Classification and Hadron Rejection

Several methods were imployed in an attempt to remove hadronic showers. Since the array was centered on the beam line, and the spark chambers had beam deadeners, the tracks of charged particles hitting the array were not always found. In addition, with an average charged particle multiplicity of perhaps 7 - 9, there should be several neutral hadrons per event. Fortunately, most of these are neutral pions, which of course are one of the particles of interest. Most of the other neutral hadrons which could reasonably survive the 17 meters from the target would be KOLs and neutrons. In any case, it was of interest to find ways to reject hadronic showers. In addition to matching tracks in the spark chambers with showers, two independent indicators were developed to aid in the rejection of such showers.

One of these indicators was concerned with the distribution of energy in the shower. In particular, the relative positions of the counters which contained the second and third largest energies was the basis for determining the shower ´type´, as this quantity was called. The counter containing the most energy was always at the center by definition. Type 0 was assigned to the theoretically perfect shower configuration. This type of shower has the counters with the second and third largest energies positioned horizontally and vertically (or vertically and horizontally) with respect to the center counter. A type of 1 was assigned if the second counter was horizontal or vertical from the center, while the third was on the diagonal and adjacent to the second. There was a total of nine possible shower types cataloging every possible unique shower configuration.

Figure A-10 attempts to illustrate the effect of cuts on the type indicator. The di-gamma invariant mass for a sample of events having exactly two showers, and both showers having a type of 0, is shown in FiFigure A-10(a). Figure A-10(b) shows the corresponding mass spectrum for events with exactly two showers which were not both type 0. There seems to be little difference in the two spectra except that the π^0 mass resolution is worse in 10(b). This results from incorrect gains and/or poor energy resolution, which may have caused the shower to be given a non-zero type. The type is more useful in events with several showers, and is typically used by requiring the sum of the types of the two showers to be less than

Figure A-10. Di-gamma invariant mass spectrum for (a) both showers having type 0, and (b) one or both showers not type 0. Most of the real photons had types of either 0 or 1.

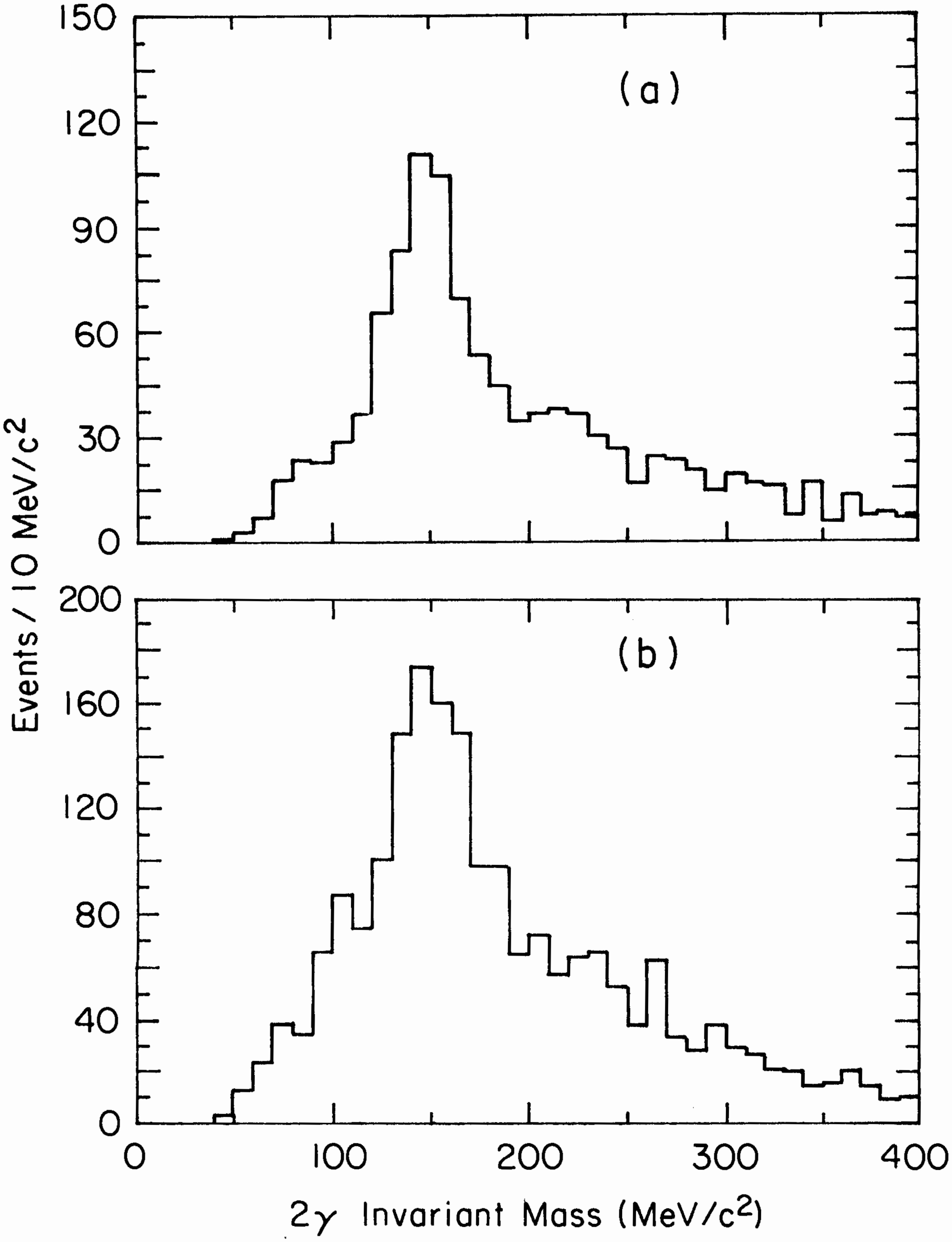
(a)
(b)
Events / 10 MeV/c^2
2γ Invariant Mass (MeV/c^2)
0
30
60
90
120
150
0
40
80
120
160
200
0
100
200
300
400

two.

There were several reasons for the occurence of showers with types other than 0. In addition to hadronic interactions, incorrect gains and dead counters were prominent causes. The relative magnitudes of the energies were not considered unless they were close enough that resolution effects could change the ´type´.

The second indicator dealt with the leakage of energy from the 4 counters containing the largest energies. It was developed by exploiting the known characteristics of the electromagnetic shower, namely:

1. Small fluctuations in the number of shower particles
2. Cylindrical symmetry about the axis
3. Containment of 90% or more of energy in at most 4 counters

The first two properties combined give electromagnetic showers cylindrical symmetry on a single shower basis, while although hadronic showers should be cylindrically symmetric on the average, the relatively small number of shower particles does not provide this symmetry event by event. In addition, the products of hadronic interactions are mainly other hadrons which are highly penetrating relative to positrons and photons. (The counters are 2 interaction lengths, but 20 radiation lengths.) This leads to large variations in the results of hadronic showers with respect to both energy deposition and distribution.

The formula developed for this indicator, called the ´quality´, is:

$$\text{Quality} = (\text{NB}-3)/\text{F4} + 100 \times (1-\text{F4})$$

where NB is the number of counters (out of 9) containing more than 1% of the total shower energy, and F4 is the fraction of the total energy contained in the 4 counters with the largest energies.

One way to compare the quality of photons and hadrons is to obtain a clean (i.e., relatively background free) sample of π^0's and examine the quality of the photons comprising them. The quality of hadrons can be obtained by taking events with exactly one shower. If the tracks of hadrons found in the spark chambers are then extrapolated to the lead glass array, and a strike is found, there is an excellent correlation between the expected and calculated (from energy sharing) impact positions. Those showers with a calculated impact position within a 6 cm radius of the charged track are taken as hadronic showers. Hence, Figure A-11 shows the distribution of the quality for photons consistent with coming from π^0 decay, while shown dashed is the quality for hadronic showers. The distribution for the hadronic showers was scaled (down) to the number of events in the solid histogram.

The di-gamma invariant mass for showers with quality less than 15 is shown in Figure A-12, while the contribution to Figure 14 from events in which the two showers were overlapping is shown in Figure A-13. The energies were separated as described in section A.3.1.

All of the mass spectra shown so far have been calculated using the gains determined during the positron calibration, except for the run dependent corrections dictated by the LED calibrations. Noting the rather poor π^0 mass resolution in Figure A-14 for an uncut sample (except for removal of showers within a 6 cm radius of a hadron track) of the data, an algorithm for minor adjustments of the gains using the photons from π^0 decay was developed. The effects of the beam (see next section) on the counters made the procedure less effective than it could have been.

Figure A-11. Distribution of shower quality. The solid histogram shows the distribution of the quality for showers consistent with photons from π^0 decay. The dashed histogram shows the quality for showers having an impact position within 6 cm of the intercept of a charged hadron track.

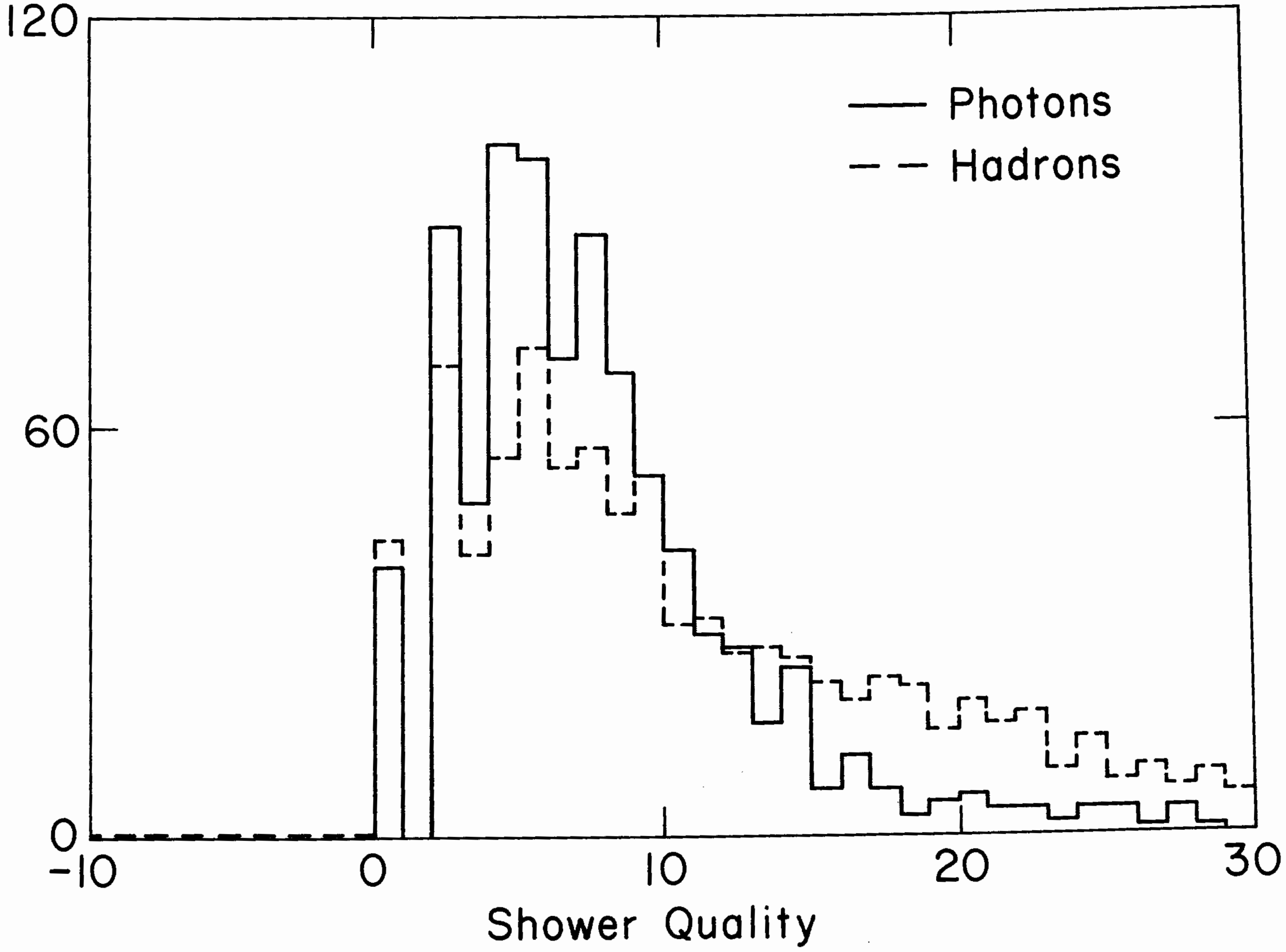
120
60
0
-10
0
10
20
30
Shower Quality
Photons
Hadrons

Figure A-12. Di-gamma invariant mass spectrum for showers with quality less than 15.

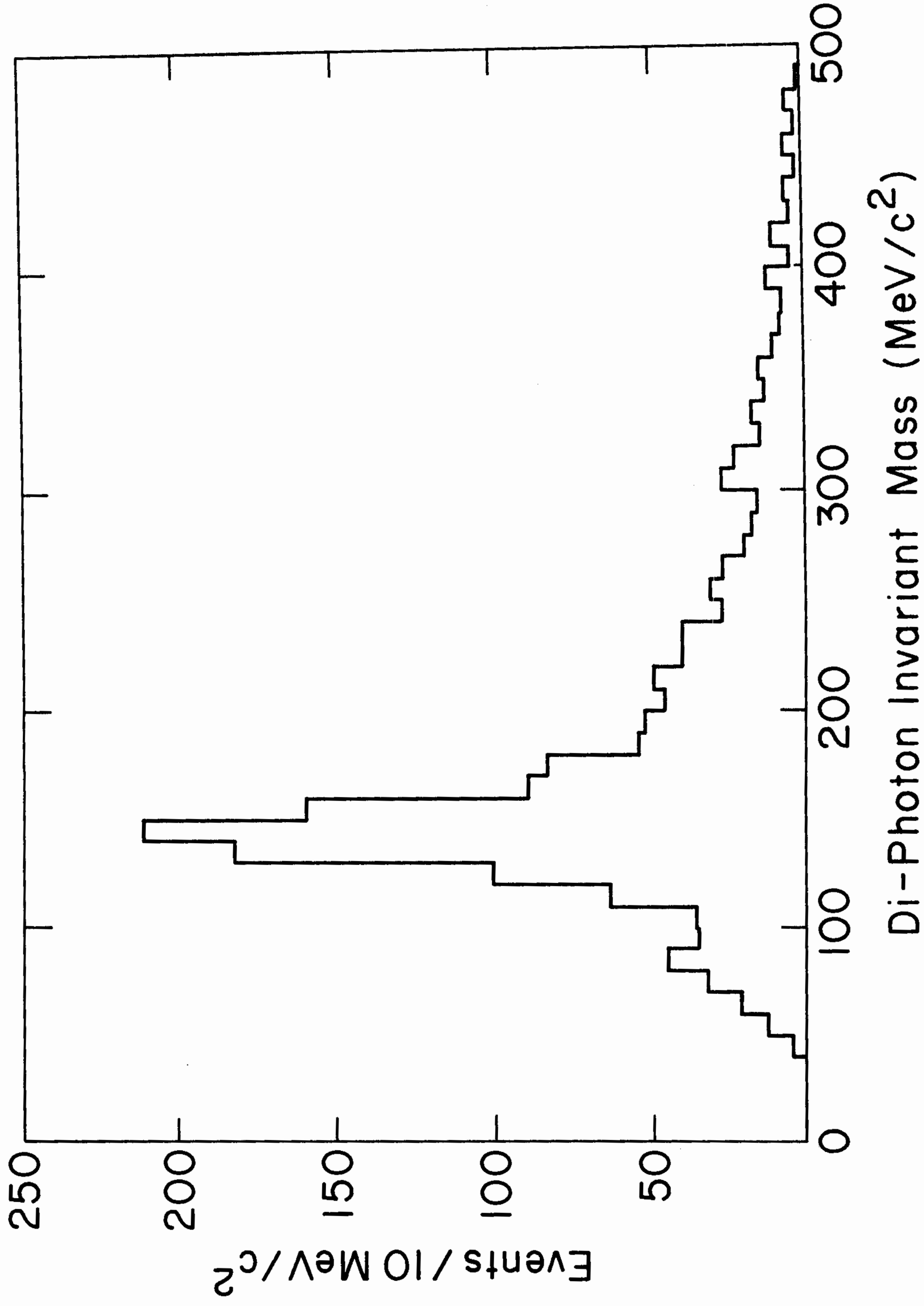
Events / 10 MeV/c^2
250
200
150
100
50
0
100
200
300
400
500
Di-Photon Invariant Mass (MeV/c^2)

Figure A-13. Di-gamma invariant mass for showers with quality less than 15 and sharing energy with one another. The shared energy was separated as described in section A.3.1.

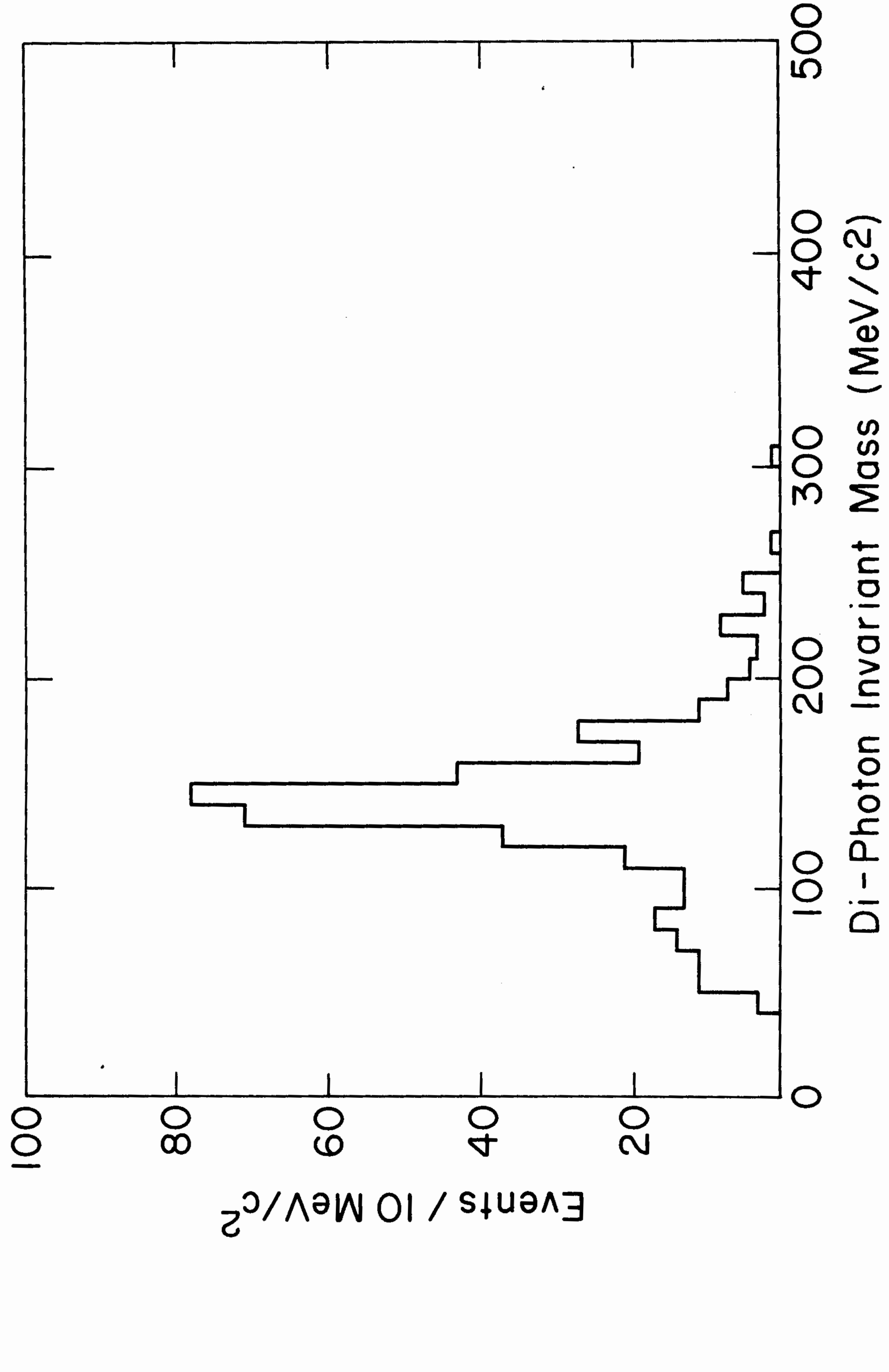
Events / 10 MeV/c^2
100
80
60
40
20
0
100
200
300
400
500
Di-Photon Invariant Mass (MeV/c^2)

Figure A-14. Di-gamma invariant mass spectrum with only showers from known charged hadrons removed.

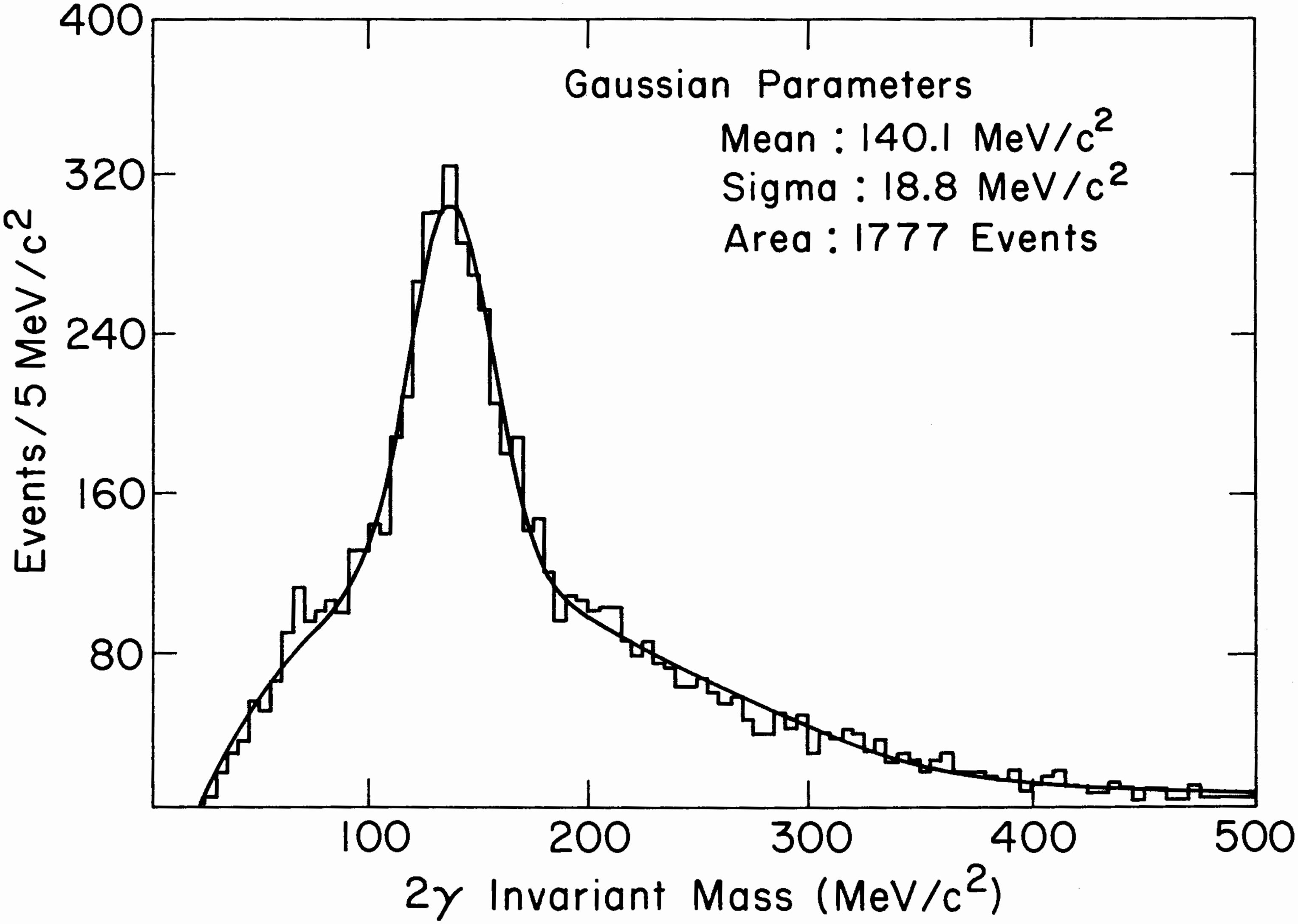
Gaussian Parameters
Mean : 140.1 MeV/c^2
Sigma : 18.8 MeV/c^2
Area : 1777 Events
400
320
240
160
80
Events / 5 MeV/c^2
100
200
300
400
500
2γ Invariant Mass (MeV/c^2)

The basic procedure was to select all events having at least two showers with energies greater than 2 Gev. These events were analyzed using the best gains available (either initial or the adjusted gains of the preceding iteration) and histograms of the di-gamma invariant mass and background were accumulated for each counter individually. The background was calculated by combining showers from separate events. After all events (usually about 50,000) were analyzed, the background subtracted histograms were searched for the π^0 peak (assuming that it dominated the histogram). In particular, the peak was located as that bin (5 Mev/bin) which was at the center of the 3 consecutive bins containing the most events. If the peak was higher than the known π^0 mass (135 Mev/c^2), the gain of the counter was reduced by 3%, whereas if the peak was lower, the gain was increased by 5%. The gains were increased and decreased different amounts to reduce the number of oscillations about the 'best gain' as it was approached. The whole process was iterated by multiplying successive adjustments to get the gains' correction, until at least 70 of the counters were no longer being adjusted. This usually took from 15 to 20 iterations.

The di-gamma invariant mass obtained after 20 iterations is shown in Figure A-15. The π^0 peak has a full width at half-maximum of about 25 Mev/c^2, compared to 45 Mev/c^2 for the spectrum in Figure A-14.

As described in the next section, beam effects were very large and unmanageable in some counters. Thus this gain adjustment process was attempted both as a function of beam intensity and time. That is, events were grouped as to the average beam intensity during the event (since the average intensity had to be calculated from scalars accumulated for about 20 beam spills, possible spill to spill variations were impossible to detect), and the iteration process carried out for each group individually.

Figure A-15. Di-gamma invariant mass spectrum after 20 iterations of the gain adjustment process. The mass resolution is nearly twice as good as in Figure A-14.

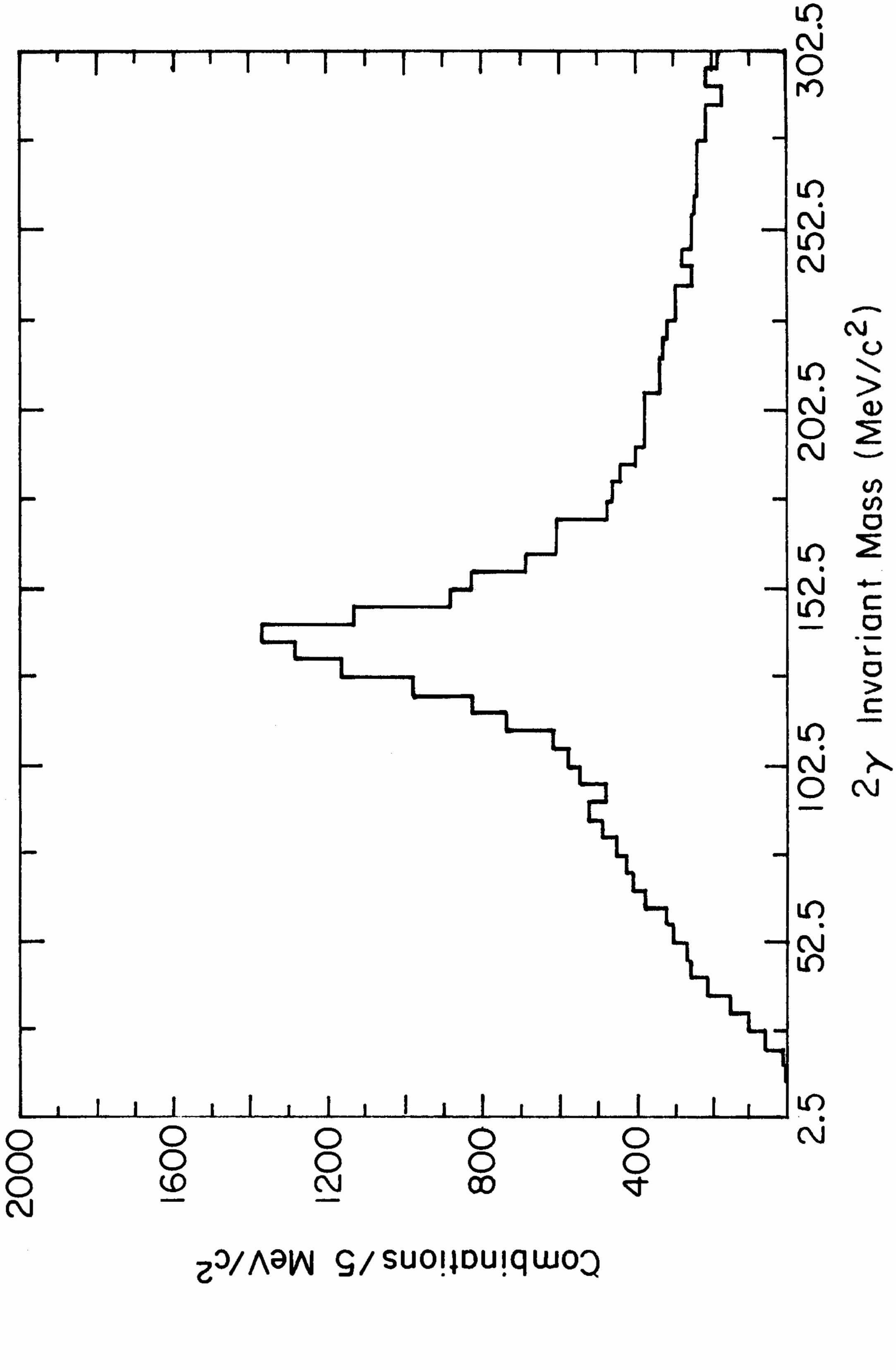
Combinations/5 MeV/c^2
2000
1600
1200
800
400
2.5
52.5
102.5
152.5
202.5
252.5
302.5
2γ Invariant Mass (MeV/c^2)

However, given the facts that the counters showing the largest gain shifts due to beam effects also were the counters becoming yellow most rapidly and that the average intensity was lower for the second half of the experiment, the widely varying results for different intensities came as no surprise.

A.3.4 Effects of Beam

It can be stated without fear of exaggeration that allowing the array to be a beam dump made a mess of the analysis. Two totally independent phenomena were responsible:

1. A beam intensity dependent gain shift in the PMTs
2. Formation of F-centers (yellowing of the glass) by irradiation

Both of these effects may have presented less of a problem had there been time to investigate them in detail during the experiment. For example, a detailed knowledge of the relationship between the beam intensity and the magnitude of the gain shift for each counter would have been of enormous help. As it was however, the entirety of the information available amounted to a few LED calibrations done during the beam spill at a few (rather high) intensities. This information showed how the gain changed from beam off conditions to beam on conditions. However, it was not sufficient to map the change over the range of intensities encountered in the analysis, or to estimate the rise and fall times of the shift. The fall time was apparently on the order of seconds, since only small differences were noted between beam just-off calibrations and calibrations done when the beam was on, for example. A normal LED calibration was started 1.5 seconds after the end of the beam spill. Calibrations started during the beam spill showed an additional change in gain, but it was smaller in magnitude than the change noted between the normal (between spill) calibrations and the beam entirely off calibrations. The longer the fall time of the gain shift the less of a problem it becomes, since the normal calibration becomes a better approximation to the in-spill calibration, and it is the in-spill calibration which reflects the true gain of the PMT. The actual magnitude of the change as estimated from the LED pulse heights varied from a few percent far from the beam to over 100% for counters in the beam.

A word about the origin of the intensity effect is in order. It is not a sagging of output due to excessive dynode current. In fact, the effect appears as an increase in PMT output, which may be eventually counteracted by sagging. One possible explanation for the effect has been given as charge build-up on the dynode-supporting insulators, thus altering the field lines. Why this should cause an increase in output is still not clear.

A.3.5 Radiation Damage

The second effect of the beam and its halo was the darkening of the glass from radiation damage. Fortunately, only a few of the counters were darkened enough to be useless. The relative gain of two counters located near the beam line was shown plotted against time in Figure A-2(b). Note that gain (in Mev/picocoulomb) is inversely proportional to the LED pulse height. Since the LED pulse height is decreasing with time, the gain increases. The main consequence of the yellowing, aside from decrease of shower brightness, is the loss of gain monitoring as provided by the LED calibrations. The reason for this is clear. The attenuation of the Cerenkov radiation relative to the attenuation of the LED radiation may change if the spectral transmission properties of the glass change. Since it is safe to say the latter is true, it is probably also safe to say that the gains are not tracked reliably if the counters are yellowing.

The worsening of energy resolution is another consequence of yellowing. As the PMT output decreases, the ADC least count (fixed at 1/4 picocoulomb) represents an increasing fraction of the energy. Non-uniform yellowing could also contribute to worsening (and energy dependent) resolution.

APPENDIX REFERENCES

Longo, E., and I. Sestilli, Nucl. Insts. Meths. 128, 283, (1975)

Shupe, M., Thesis, Tufts University, 1976

VITA

Daniel Eugene Bender [redacted] [redacted] [redacted] [redacted] [redacted] [redacted] [redacted] [redacted] [redacted] [redacted] [redacted] [redacted]. He earned the Bachelor of Science degree in physics from the University of Illinois in 1974, and the Master of Science degree in physics in 1975. He served both as a teaching assistant and a research assistant, and was co-author of "Production of Photons Associated with the ψ by 217 Gev/c π^- Mesons", T. B. W. Kirk, et al., Phys. Rev. Lett. 42, 619 (1979).